# Dynamics of a cold trapped ion in a Bose-Einstein condensate

Dissertation

zur Erlangung des akademischen Grades
Dokotor der Naturwissenschaften (Dr. rer. nat.)

eingereicht an der
Fakultät für Naturwissenschaften
der
Universität Ulm

von
Stefan Schmid
aus
Schwaz in Tirol

Betreuer der Dissertation: Johannes Hecker Denschlag

November 2011

Amtierender Dekan: Prof. Dr. Axel Groß
Erstgutachter: Prof. Dr. Johannes Hecker Denschlag
Zweitgutachter: Prof. Dr. Tommaso Calarco
Tag der mündlichen Prüfung:

The work described in this thesis was carried out at the

Universität Innsbruck
Institut für Experimentalphysik
Technikerstrasse 25
A-6020 Innsbruck

and at the

Universität Ulm
Institut für Quantenmaterie
Albert-Einstein-Allee 11
D-89069 Ulm

# Zusammenfassung

In dieser Arbeit habe ich mich mit Kollisionen zwischen lasergekühlten, gefangenen Ionen ($Ba^+$ oder $Rb^+$) und ultrakalten neutralen Atomen (Rb) beschäftigt. Dafür war es notwendig einen neuartigen experimentellen Aufbau zu entwickeln, welcher ein Bose-Einstein Kondensations (BEC) Experiment mit einer Paulfalle für einzelne Ionen kombiniert. Die ultrakalten Atome werden dabei in einer magnetischen Falle innerhalb des BEC Experiments hergestellt und mit Hilfe eines bewegten optischen Gitters vertikal über eine Strecke von 30 cm zur Ionenfalle transportiert.

Die Wechselwirkung zwischen Atomen und Ionen kann durch ein $1/r^4$ Polarisationspotential beschrieben werden. Sie ist im Allgemeinen langreichweitiger und stärker als die Wechselwirkung zwischen zwei neutralen Atomen. In unseren ersten Experimenten konnten wir sowohl elastische als auch inelastische Atom-Ionen Kollisionen beobachten. Die elastischen Stöße wurden über die Messung von Atomverlusten nachgewiesen. Mit Hilfe dieser Atomverlust-Messung konnten wir eine typische Kollisionsenergie von ca. 10 mK und einen elastischen Wechselwirkungsquerschnitt von ungefähr $10^{-14}\,\mathrm{m}^2$ abschätzen. In unserem Experiment ist die inelastische Streuung ist im Vergleich zu elastischen Kollisionen um einen Faktor $10^4$ bis $10^5$ unterdrückt. Dennoch konnten wir nachweisen, dass der dominante inelastische Prozess die Ladungstransferreaktion $\mathrm{Rb} + \mathrm{Ba}^+ \rightarrow \mathrm{Rb}^+ + \mathrm{Ba}$ ist. Zudem haben wir gezeigt, dass ein einzelnes Ion verwendet werden kann, um die Dichteverteilung einer ultrakalten Atomwolke zu bestimmen, was eine mögliche Anwendung unseres Aufbaus darstellt.

# Abstract

In this thesis I have investigated the collisions between laser-cooled trapped ions ($Ba^+$ or $Rb^+$) and ultracold neutral atoms (Rb). For this purpose it was necessary to develop a novel hybrid apparatus, where a Bose-Einstein condensation (BEC) apparatus is combined with a Paul trap for single ions. The ultracold atom cloud is produced in a magnetic trap within the BEC apparatus and then transported vertically over a distance of 30 cm using a 1d moving optical lattice.

The interaction between the atoms and the ions can be described by a $1/\mathrm{r}^4$ polarization potential. Generally, the atom-ion interaction is stronger and long-range compared to the interaction between two neutral atoms. In our experiments we were able to observe elastic as well as inelastic atom-ion collisions. Elastic scattering was detected by measuring the loss of atoms in the presence of an ion. From this atom loss measurement we could estimate a typical collision energy of about 10 mK and an elastic scattering cross section on the order of $10^{-14}\mathrm{m}^2$. Inelastic processes are suppressed by a factor $10^4$ to $10^5$ in our experiment. Nevertheless, we were able to show that the dominant inelastic collision channel is the charge transfer reaction $\mathrm{Rb} + \mathrm{Ba}^+ \rightarrow \mathrm{Rb}^+ + \mathrm{Ba}$. As a possible application of our apparatus, we have demonstrated that a single ion can be used to probe the density profile of an ultracold atom cloud.

*Für meinen Vater*

# Contents

**1 Introduction** **13**

**2 Theory of atom-ion collisions** **17**

2.1 The 1/r$^4$ interaction potential . . . 18

2.2 Classical atom-ion collision theory . . . 19

2.2.1 Scattering at the $1/r^4$ potential - appearance of the critical impact parameter $b_c$ . . . 20

2.2.2 Collisions with $b < b_c$ - Langevin collisions . . . 21

2.2.3 Collisions with $b > b_c$ - Glancing collisions . . . 22

2.2.4 Elastic scattering cross section . . . 23

2.3 Quantum mechanical atom-ion collision theory . . . 28

2.3.1 Semiclassical approximation . . . 28

2.3.2 Full quantum mechanical treatment . . . 29

**3 Experimental setup** **32**

3.1 The vacuum system . . . 32

3.1.1 Lower level: Cold atom section . . . 34

3.1.2 Upper level: Ion trapping and science section . . . 39

3.2 Generation of magnetic fields . . . 40

3.3 Laser systems . . . 41

3.3.1 Rb lasers . . . 41

3.3.2 Ba$^+$ lasers . . . 44

3.3.3 High power laser system for atom trapping . . . 48

3.4 Experimental control . . . 48

**4 Trapping of Barium ions** **51**

4.1 The Linear Paul trap . . . 51

4.2 Operating the trap . . . 54

4.2.1 Loading of ions . . . . . . . . . . . . . . . . . . . . . . . . 54
4.2.2 Cooling of ions . . . . . . . . . . . . . . . . . . . . . . . . 56
4.2.3 Detection of ions . . . . . . . . . . . . . . . . . . . . . . . 57
4.3 Oscillation frequencies . . . . . . . . . . . . . . . . . . . . . . . . 58
4.3.1 Single ion - trap frequencies . . . . . . . . . . . . . . . . . 59
4.3.2 Normal mode frequencies of a two-ion crystal . . . . . . . 61
4.4 Trap depth . . . . . . . . . . . . . . . . . . . . . . . . . . . . . . 63
4.5 Micromotion . . . . . . . . . . . . . . . . . . . . . . . . . . . . . . 64
4.5.1 Ion kinematics in the presence of an electric field . . . . . 65
4.5.2 Compensation electrodes . . . . . . . . . . . . . . . . . . . 66
4.5.3 Minimization of excess micromotion . . . . . . . . . . . . . 67
4.5.4 Further sources of excess micromotion . . . . . . . . . . . 68

**5 Bose-Einstein condensates of Rubidium 71**
5.1 Generation of the ultracold atom cloud . . . . . . . . . . . . . . . 71
5.1.1 Magneto-optical trap . . . . . . . . . . . . . . . . . . . . . . 71
5.1.2 Molasses cooling, spinpolarizing and magnetic trapping . . 72
5.1.3 Magnetic transport . . . . . . . . . . . . . . . . . . . . . . . 73
5.1.4 QUIC trap and evaporative cooling . . . . . . . . . . . . . 75
5.2 Optical trapping of the atoms . . . . . . . . . . . . . . . . . . . . 77
5.2.1 The Dipole force . . . . . . . . . . . . . . . . . . . . . . . . 77
5.2.2 Transport of ultracold atoms using a moving optical lattice 78
5.2.3 Crossed dipole trap . . . . . . . . . . . . . . . . . . . . . . . 88

**6 Collisions of cold ions with ultracold neutral atoms 91**
6.1 Elastic collisions between a cold ion and ultracold neutral atoms . 93
6.1.1 Elastic collision cross section - simple model . . . . . . . . 94
6.1.2 Elastic collision cross section - “sphere of depletion” model 97
6.1.3 Energy dependence of the collision rate . . . . . . . . . . . 103
6.1.4 A single ion as a local density probe . . . . . . . . . . . . 104
6.2 Inelastic processes . . . . . . . . . . . . . . . . . . . . . . . . . . . 107
6.2.1 Observation of charge transfer reactions . . . . . . . . . . 109

**7 Conclusion and Outlook 113**

**8 Danksagung 115**

**9 Erklärung 117**

# Chapter 1

# Introduction

In recent years, both the fields of cold trapped ions and of neutral, ultracold atomic gases have experienced an astonishing development. Full control has been gained over the respective systems down to the quantum level. Single ions can be selectively addressed and their quantum states can be coherently manipulated and read out [1]. The collective behavior of neutral atomic quantum gases can be mastered by controlling the particle-particle interactions, temperature, and physical environment. The observation of Bose-Einstein condensation (BEC), solitons, vortices, and the Mott-insulator quantum phase transition are prominent examples for this achievement [2].

It was at the end of 2006, when we started our efforts of combining cold trapped ions with ultracold neutral atoms in Innsbruck. Our vision was to merge a Bose-Einstein condensation (BEC) apparatus with a linear Paul trap, where single ions or a string of a few ions can be stored and cooled to the Doppler limit. At that time a few theoretical proposals on cold and ultracold atom-ion collisions had recently been made. And example is the work done by Robin Côté and co-workers [3–5]. Parallel to our group, also Winthrop Smith and the groups of Vladan Vuletic and Michael Köhl started their experimental efforts. Their work is closely related to ours, since they all work with a combination of trapped atoms and ions [6–10]. Besides these measurements in the mK regime, various experiments with collision energies on the order of $k_B \times 1\,\mathrm{K}$ or beyond have been performed in the past. Already back in 1991, reactions of $NO^+$ with He, Ar and $N_2$ down to energies of $k_B \times 0.3\,\mathrm{K}$ have been studied by Hawley et. al. [11]. Later on, Dieter Gerlich an co-workers have reported about experiments with ions trapped in multi-pole traps and cold He buffer gases [12, 13]. Recently, Stefan Willitsch, Timothy Softley and co-workers have investigated reactive collisions between laser-cooled trapped $Ca^+$ ions and velocity-selected polar $CH_3F$ molecules [14]. Also, experiments with cold charged molecules have been performed in the groups of Michael Drewsen and Stephan Schiller. In their setups optical techniques were used to reduce the energy of the molecular ions [15, 16].

The ultimate goal of our experiment is to study the interaction between ions and atoms in the limit of small collision energies. For this purpose we have built up a novel hybrid apparatus, where ultracold Rb atoms can be brought into the center of a linear Paul trap, which is typically loaded with a small and well defined number of $Ba^+$ or $Rb^+$ ions. The central idea of our hybrid experiment is the spatial separation of the BEC apparatus, where the ultracold atoms (or a BEC) are produced, from the ion-trapping region, where the atom-ion collision experiments are performed. Thereby, we avoid mutual disturbance between the radiofrequency (RF) Paul trap and the RF used for forced evaporative cooling of the atomic sample. Moreover, by keeping all the elements (coils, optical components) needed for atom cooling away from the ion trapping region, we gain valuable optical access to the “science section”, that can be used to trap, manipulate, and detect the atoms and ions. However, due to the large distance of 30 cm between the BEC apparatus and the ion trap, a powerful and reliable transport technique is required to transfer the ultracold atoms from their place of production to the science section. For this purpose, we employ a moving 1-dimensional (1-d) optical lattice. The details of our experimental setup will be published in [17].

With our apparatus we were able to observe the interaction between a single trapped $Ba^+$ ion and an ultracold optically-trapped cloud of Rb atoms (T=100nK or Bose-Einstein-condensed) [18]. By measuring the loss of atoms in the presence of the ion we find the cross section for elastic scattering to be large, as expected from theory [3], with values on the order of $10^{-14}\,\mathrm{m}^2$. In contrast, charge transfer reactions, which are the dominant inelastic collision channel, are strongly suppressed with cross sections on the order of $10^{-19}\,\mathrm{m}^2$ or below. In our type of setup the collision energy is determined by the excess micromotion of the ion. The first attempts of compensating excess micromotion, which I will present in this thesis, have lead to minimal collision energies on the order of 10 mK.

For comparison in the Vuletic experiment a magneto-optical trap (MOT) for Yb is combined with a surface-electrode Paul trap for $Yb^+$ [6, 7]. In their setup the collision energy was too large to enter the regime of ultracold atom-ion collisions, for which a quantum mechanical description is required. However, the observations of the Vuletić group have shown that atoms and ions can principally be trapped at the same location. On the other hand, the idea of the Köhl experiment is very similar to ours. A single trapped $Yb^+$ ion is immersed into an ultracold cloud of Rb atoms [8–10]. The measured cross sections and the collision energy are on the same order of magnitude as in our system. This is not surprising since the inner structure of the ion is only relevant in the ultracold but not in the mK regime.

In the future we plan to study the formation of molecular ions (such as $Rb_2^+$ or $(BaRb)^+$) [19], polaron-type physics [20–23], charge hopping in the ultracold domain [4] and the formation of a mesoscopic molecular ion [5]. For the latter type of experiment it will be necessary to enter the regime of ultracold elastic atom-ion collisions [3], which we might be able to reach by improving the compensation of excess micromotion.

In the following chapter I will present the theoretical groundwork to understand the atom-ion collision dynamics in the various collision energy regimes. Subsequently in chapter 3 the focus is put onto the experimental setup. In chapter 4 and 5 the preparation of the single $Ba^+$ ion and the creation of the Rb BEC are described. The main scientific results of this theses are presented in chapter 6, showing all the measurements on the atom-ion interaction. Finally, an outlook on possible future experiments is given in chapter 7.

# Chapter 2

# Theory of atom-ion collisions

In this chapter I will outline the theoretical groundwork for understanding the dynamics of atom-ion collisions. I will start with a derivation of the atom-ion interaction potential. Using this potential I will then derive the classical atom-ion collision theory (Langevin theory) and calculate classical estimates for the collision cross sections. In a further step I will present a semiclassical description of the atom-ion scattering and compare it with the classical results. The main focus in this theory chapter is put on these two approaches (the classical and the semiclassical), since they are sufficient to explain the experimental data presented in this thesis. However, the aim for the future is to enter the ultracold regime, where the collision energies are low enough that a full quantum mechanical treatment becomes necessary. Therefore I will also touch the theory of ultracold atom-ion collisions at the end of this chapter.

It is important to realize that the theories described in the following can only be used to treat two-body collisions, such as

$$\mathrm{Rb} + \mathrm{Ba}^+ \rightarrow \begin{cases} \mathrm{Rb} + \mathrm{Ba}^+ & \text{elastic} \\ \mathrm{Rb}^+ + \mathrm{Ba} + \gamma & \text{radiative charge transfer} \\ \mathrm{Rb}^+ + \mathrm{Ba} & \text{nonradiative charge transfer} \\ (\mathrm{RbBa})^+ + \gamma & \text{molecule formation} \\ \widetilde{\mathrm{Rb}} + \widetilde{\mathrm{Ba}}^+ & \text{spin-exchange} \end{cases} \tag{2.1}$$

where the tilde denotes a different spin-state of the ion or the atoms, respectively. In the homo-nuclear case we can have

$$\mathrm{Rb} + \mathrm{Rb}^+ \rightarrow \begin{cases} \mathrm{Rb} + \mathrm{Rb}^+ & \text{elastic} \\ \widetilde{\mathrm{Rb}} + \widetilde{\mathrm{Rb}}^+ & \text{spin-exchange.} \end{cases} \tag{2.2}$$

The assumption of binary collisions is justified by our experiments, where we have only observed elastic and charge transfer collisions, but no other type of collisions. Nevertheless, at high atomic densities we obviously also expect three-body processes, such as

$$\mathrm{Rb} + \mathrm{Rb} + \mathrm{Ba}^+ \quad \rightarrow \quad \begin{cases} \mathrm{Rb} + (\mathrm{RbBa})^+ & \text{molecule formation} \\ \mathrm{Ba} + \mathrm{Rb}_2^+ & \text{molecule formation} \end{cases} \tag{2.3}$$

$$\mathrm{Rb} + \mathrm{Rb} + \mathrm{Rb}^+ \quad \rightarrow \quad \mathrm{Rb} + \mathrm{Rb}_2^+ \qquad \text{molecule formation} \tag{2.4}$$

to take place. However, the proper description of the dynamics of many-body processes is beyond the scope of this thesis.

## 2.1 The $1/\mathrm{r}^4$ interaction potential

In the inhomogeneous field of an ion, a neutral atom is polarized and attracted towards the ion. To derive the corresponding interaction potential we consider an atom with an electric dipole moment $p$. The potential energy of the atom in the presence of the electric field of the ion $\mathcal{E}$ is then given by

$$V = -\frac{1}{2} p \mathcal{E}. \tag{2.5}$$

Since the dipole moment of the atom is induced by the electric field of the ion we can write

$$p = \alpha \mathcal{E} \tag{2.6}$$

where $\alpha = 4\pi\epsilon_0\widetilde{\alpha}$ is the dc polarizability of the atom. By plugging (2.6) into (2.5) and using the well-known expression for the electric field of an ion, we get

$$V(r) = \frac{C_4}{2r^4} \tag{2.7}$$

with

$$C_4 = -\frac{\widetilde{\alpha} q^2}{4\pi\epsilon_0} \tag{2.8}$$

where $r$ is the distance between the atom and the ion and $q$ the charge of the ion. For essentially any neutral atom the value for $\widetilde{\alpha}$ can be found in [24]. In our case of Rb $\widetilde{\alpha} = 4.7 \times 10^{-29}\,\mathrm{m}^3$ or in atomic units $\widetilde{\alpha} = 318 a_0^3$, where $a_0 = 5.29 \times 10^{-11}\,\mathrm{m}$ is the Bohr radius. By equating the centrifugal energy with the potential (2.7)

$$\left(\frac{\hbar^2}{2\mu r^2}\right)_{r=r^*} = \left(\frac{C_4}{2r^4}\right)_{r=r^*}, \tag{2.9}$$

we find the characteristic radius $r^*$ to be

$$r^* = \sqrt{\frac{\mu C_4}{\hbar^2}}, \tag{2.10}$$

Here $\mu = m_{\mathrm{ion}} m_{\mathrm{atom}}/(m_{\mathrm{ion}} + m_{\mathrm{atom}})$ is the reduced mass. For the case of ($^{87}$Rb, $^{138}$Ba$^+$) we get $r^* = 295\,\mathrm{nm}$ and for ($^{87}$Rb, $^{87}$Rb$^+$) we find $r^* = 266\,\mathrm{nm}$. The corresponding characteristic energies $\hbar^2/(2\mu r^{*2})$ are $k_B \times 50\,\mathrm{nK}$ ($^{87}$Rb, $^{138}$Ba$^+$) and $k_B \times 80\,\mathrm{nK}$ ($^{87}$Rb, $^{87}$Rb$^+$), respectively. For collision energies much smaller than this characteristic energy, only the partial wave with $l = 0$ (the so-called "s-wave") contributes to the scattering (see below). In this regime the scattering cross section becomes energy-independent with a value on the order of $4\pi r^{*2}$. The characteristic radius $r^*$, which sets the length scale of the $1/r^4$ potential, is much larger than the the van der Waals radius $R_{\mathrm{vdW}}$, which typically determines the range of the atom-atom interaction potential. A typical value is $R_{\mathrm{vdW}} = 5\,\mathrm{nm}$ for $^{87}$Rb [25]. The comparison of $r^*$ with $R_{\mathrm{vdW}}$ clearly shows the long-range characteristics of the atom-ion interaction potential (2.7), compared with the $1/\mathrm{r}^6$ van der Waals potential between two neutral atoms.

## 2.2 Classical atom-ion collision theory

By simply applying the laws of classical mechanics, it is possible to calculate both a classical estimate for the total elastic scattering cross section $\sigma_{\mathrm{elastic}}(E)$ as well as the energy dependence of the inelastic collision cross section $\sigma_{\mathrm{inelastic}} \propto E^{-1/2}$.

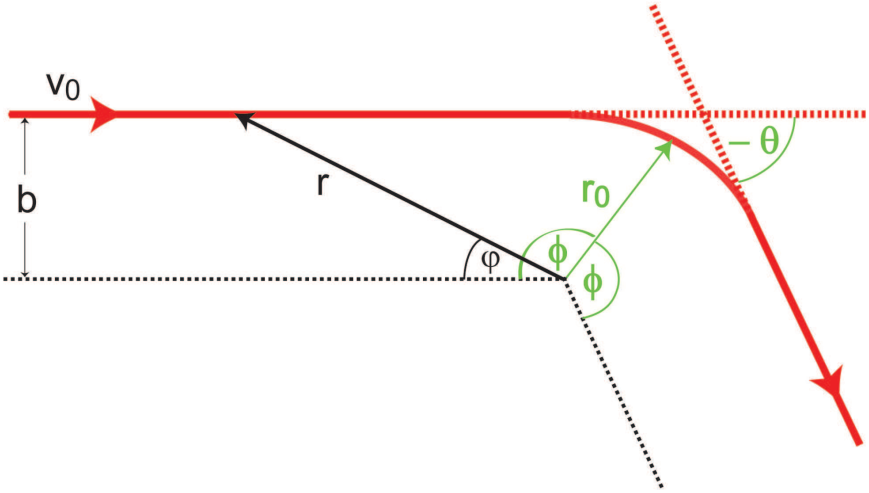

Figure 2.1: Collision between two particles: In the equivalent one-body-problem a particle with mass $\mu$ and starting velocity $v_0$ is deflected by an angle $\theta$, due to the presence of the radially-symmetric potential given by equation (2.7). If we adopt the common definitions, the scattering angle $\theta$ is negative for our case of an attractive potential. At any instant of time the position of the particle is well-defined by the distance from the center $r$ and the polar angle $\varphi$. At the point of minimum distance $r_0$, the polar angle is $\varphi(r_0) = \phi = \pi/2 - \theta/2$.

### 2.2.1 Scattering at the $1/r^4$ potential - appearance of the critical impact parameter $b_c$

We start the calculation of the cross sections by considering the two-body problem in the presence of the atom-ion interaction potential given by equation (2.7). By making a transformation to the center-of-mass (COM) coordinates (COM position $\vec{R}$ and relative coordinate $\vec{r}$), we reduce our two-body problem to the equivalent one-body problem. The relevant parameters are illustrated in Fig. 2.1. In cylindrical coordinates $\vec{r} = r\cos\varphi\vec{e}_x + r\sin\varphi\vec{e}_y + z\vec{e}_z$ the total energy $E$ of our quasi-particle with mass $\mu$ can be written as

$$E = \frac{\mu}{2}\left(\dot{r}^2 + r^2\dot{\varphi}^2\right) - \frac{C_4}{2r^4}. \tag{2.11}$$

Before the collision, the relative velocity between the two particles is $v_0$ and the distance $r \to \infty$. The total energy then reads

$$E = \frac{\mu}{2}v_0^2. \tag{2.12}$$

In a similar fashion we also find an equation for the angular momentum $\vec{L} = L\vec{e}_z$ of our virtual particle.

$$L = \mu r^2 \dot{\varphi} = \mu v_0 b, \tag{2.13}$$

where the left hand side is the general expression and the right hand side the angular momentum again before the collision. The so-called impact parameter $b$ is introduced in Fig. 2.1.

By equating (2.11) with (2.12) and substituting $\dot{\varphi}$ using (2.13) we obtain an expression for $\dot{r}$

$$\dot{r} = \pm v_0 \sqrt{1 - \frac{b^2}{r^2} + \frac{C_4}{\mu v_0^2 r^4}}. \tag{2.14}$$

We can now calculate the minimal distance to the center $r_0$, since we know that $\dot{r}(r = r_0) = 0$. We get

$$r_0^2 = \frac{b^2}{2} \pm \sqrt{\frac{b^4}{4} - \frac{C_4}{\mu v_0^2}}. \tag{2.15}$$

In order for $r_0$ to be a real quantity, the impact parameter $b$ needs to be larger than the critical impact parameter $b_c$ given by

$$b_c = \left(\frac{4C_4}{\mu v_0^2}\right)^{1/4} = \left(\frac{2C_4}{E}\right)^{1/4}. \tag{2.16}$$

Note that the critical impact parameter only depends on the collision energy $E$ and on the polarizability of the atom.

### 2.2.2 Collisions with $b < b_c$ - Langevin collisions

For impact parameters smaller than the critical impact parameter ($b < b_c$) the virtual particle is not simply deflected at the potential, as depicted in Fig. 2.1. In fact, it follows an inward-spiraling orbit, where it finally ends up at the center of the potential. The cross section for this type of collision is called Langevin cross section and is given by

$$\sigma_{\text{Langevin}} = \pi b_c^2 = \pi \sqrt{\frac{2C_4}{E}}. \tag{2.17}$$

The Langevin cross section, initially derived by Langevin in 1905 [26], includes all collisions where the atom-ion separation eventually reaches zero. Assuming that reactive collisions (such as charge exchange or spin-changing collisions) are always Langevin-type collisions, we can relate $\sigma_{\text{Langevin}}$ to the inelastic collision cross sections

$$\sigma_{\text{inelastic}} = p_{\text{inelastic}} \sigma_{\text{Langevin}}, \tag{2.18}$$

where $p_{\text{inelastic}} = 1 - p_{\text{elastic}}$ is the probability for an inelastic collision to take place, once the atom and the ion have come close to each other. It can be written as a sum of the probabilities for all relevant processes

$$p_{\text{inelastic}} = p_{\text{ch.ex.}} + p_{\text{spin-ex.}} + \dots \tag{2.19}$$

In general these probabilities depend on the inner structure of the particles and can obviously not be predicted with the simple Langevin theory. At this point a quantum-mechanical description of the scattering process becomes necessary.

### 2.2.3 Collisions with $b > b_c$ - Glancing collisions

For collisions with impact parameters $b > b_c$ the atom-ion separation stays finite and the two particles are deflected of each other with well defined angles. In the COM frame the scattering angle is given by $\theta = \pi - 2\phi$ where

$$\phi = \int_{\infty}^{r_0} \frac{d\varphi}{dr} dr \tag{2.20}$$

(see Fig. 2.1). The minimal separation $r_0$ is given by equation (2.15), whereas

$$\frac{d\varphi}{dr} = \frac{\dot{\varphi}}{\dot{r}} = \frac{b}{r^2 \sqrt{1 - \frac{b^2}{r^2} + \frac{b_c^4}{4r^4}}} \tag{2.21}$$

By introducing the dimensionless impact parameter $\widetilde{b} = b/b_c$, the solution of the integral (2.20) can be written as

$$\phi = \widetilde{b}\sqrt{2}\sqrt{\widetilde{b}^2 - \sqrt{\widetilde{b}^4 - 1}} \cdot \mathcal{K}\left(2\widetilde{b}^4 - 2\widetilde{b}^2\sqrt{\widetilde{b}^4 - 1} - 1\right) \tag{2.22}$$

where

$$\mathcal{K}(m) = \int_0^{\pi/2} \frac{1}{\sqrt{1 - m \sin^2 x}} dx \tag{2.23}$$

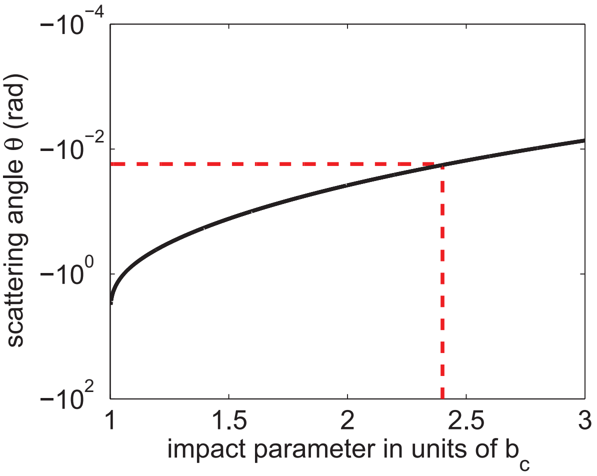

Figure 2.2: The scattering angle versus the dimensionless impact parameter $\widetilde{b} = b/b_c$. For $\widetilde{b} > 2.4$ the scattering angle is smaller than 1° (red dashed lines), which shows that the particles are only deflected significantly when $\widetilde{b} \sim 1$.

is the complete elliptic integral of the first kind.

The expression (2.22) is plotted in Fig. 2.2. One clearly sees that the scattering angle $\theta$ is very small unless $\widetilde{b}$ is close to 1. To show that the main contribution to the (total) cross section comes from scattering events with a small deflection angle, we derive the differential scattering cross section

$$\left(\frac{d\sigma}{d\Omega}\right)_{\text{glancing}} = \left|\frac{b}{\sin\theta}\frac{db}{d\Theta}\right| \tag{2.24}$$

The result is also plotted in Fig. 2.3. For small scattering angles the differential cross section becomes many orders of magnitude larger than $b_c^2$. In fact, for $\theta \to 0$, $(d\sigma/d\Omega)_{\text{glancing}} \to \infty$. Thus, the integral which gives us the total cross section $\sigma = \int \frac{d\sigma}{d\Omega} d\Omega$ has to be truncated for small $\theta$. In the following section we will discuss possible lower bounds for $\theta$ and will discover the total elastic collision cross section.

### 2.2.4 Elastic scattering cross section

As we have learned in the previous sections, a classical treatment of the atom-ion scattering leads to two different types of collisions, the Langevin-type collisions and the glancing collisions. The latter ones are always elastic collisions, since reactive collisions can only take place when the atom-ion separation vanishes. Fur-

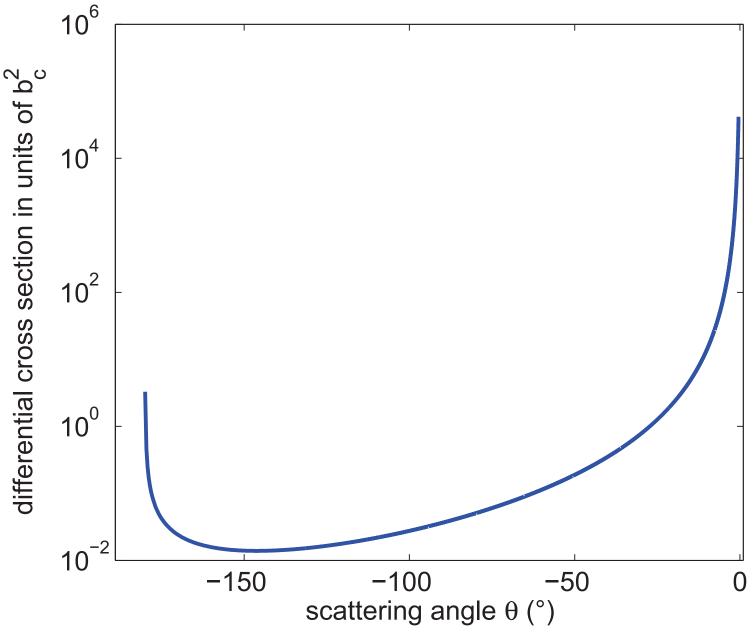

Figure 2.3: The differential cross section $(d\sigma/d\Omega)_{\text{glancing}}$ is minimal for a scattering angle of $\theta = 146°$ and diverges for $\theta \to 0$.

thermore for a hetero-nuclear system such as (Rb, $\text{Ba}^+$) also the Langevin-type collisions are predominantly elastic $p_{\text{inelastic}} \sim p_{\text{ch.ex.}} \ll 1$ (see also the discussion in the previous section). Thus, we can write the elastic cross section as

$$\sigma_{\text{elastic}} \approx \sigma_{\text{Langevin}} + \sigma_{\text{glancing}} \tag{2.25}$$

where $\sigma_{\text{Langevin}}$ is given by equation (2.17) and

$$\sigma_{\text{glancing}} = 2\pi \int_{-\pi}^{\theta_{\text{min}}} \left(\frac{d\sigma}{d\Omega}\right)_{\text{glancing}} \sin\theta d\theta. \tag{2.26}$$

The integral is truncated at a finite $\theta_{\text{min}}$, since the integrand diverges for $\theta \to 0$.

### Heisenberg limit $\theta_{\text{min}}$

If we want to take into account all collisions which can in principle be detected, we have to truncate the integral at the Heisenberg limit

$$\sin\theta_{\text{min}} = \frac{\Delta p_{\text{min}}}{p} \tag{2.27}$$

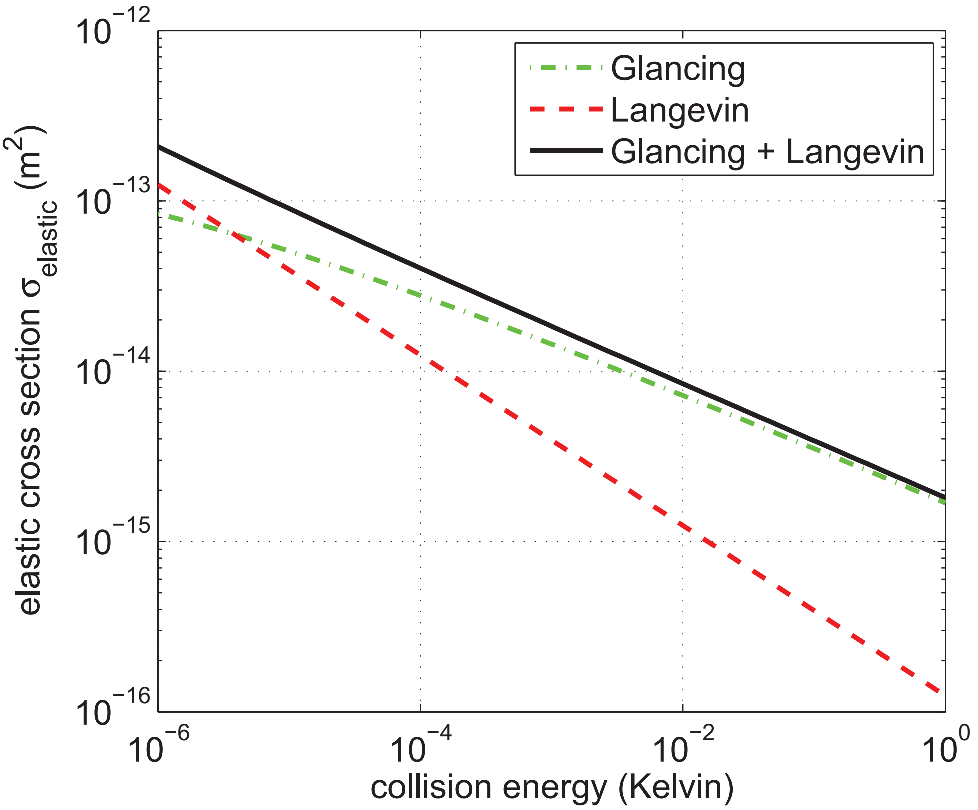

Figure 2.4: For a hetero-nuclear system the cross section for elastic scattering is given by $\sigma_{\text{elastic}} \approx \sigma_{\text{Langevin}} + \sigma_{\text{glancing}}$. For collision energies $E$ down to about $10^{-5}$ K mainly the glancing collisions contribute to $\sigma_{\text{elastic}}$. Moreover, we recognize the dependence $\sigma_{\text{elastic}} \propto E^{-1/3}$ over the entire range, where the classical model is valid.

where $p = \sqrt{2Em}$. For a particle with a position uncertainty of $b(\theta_{\text{min}})$, the minimal uncertainty of the momentum is given by $\Delta p_{\text{min}} \simeq \hbar / b(\theta_{\text{min}})$. By plugging this expression for $\Delta p_{\text{min}}$ into (2.27) we can (numerically) calculate $\theta_{\text{min}}$. The resulting cross section is plotted in Fig. 2.4. For the energy range where the classical theory is assumed to be appropriate ($E \gtrsim k_{\text{B}} \times 30\,\mu\text{K}$) we find the elastic scattering cross section $\sigma_{\text{elastic}}$ to be mainly determined by $\sigma_{\text{glancing}}$. Moreover, we can read off from Fig. 2.4, that the total elastic collision cross section scales as $\sigma_{\text{elastic}} \propto E^{-1/3}$. In the semiclassical theory described later, we will recover this energy-dependence.

### Trap depth limit $\theta_{\text{min, loss}}$

Experimentally, elastic atom-ion collisions are observed via the loss of atoms from their trap. This atom loss can be written as

$$\dot{N} = -n\sigma_{\text{loss}} v_0, \tag{2.28}$$

where $n$ is the atomic density and $v_0 = \sqrt{2E/\mu} = \sqrt{2E_{\text{ion}}/m_{\text{ion}}}$. In our system $\sigma_{\text{loss}} \approx \sigma_{\text{Langevin}} + \sigma_{\text{glancing, loss}}$ is almost identical with $\sigma_{\text{elastic}}$, except that the integral

$$\sigma_{\text{glancing, loss}} = 2\pi \int_{-\pi}^{\theta_{\text{min, loss}}} \left(\frac{d\sigma}{d\Omega}\right)_{\text{glancing}} \sin\theta d\theta. \tag{2.29}$$

is truncated at $\theta_{\text{min, loss}}$. The reason for this new limit $\theta_{\text{min, loss}}$ is that an atom is only lost from the trap, when the energy transferred to the atom $E_{\text{trans}}$ is larger than the trap depth $U_{\text{trap}}$. Here, it is important to note that the mean free path of the atom is much larger than the size of the atom cloud. Therefore, the probability for the atom colliding with another atom after being scattered at the ion and before leaving the trap, is negligible. The transferred energy $E_{\text{trans}}$ can be calculated as a function of the scattering angle $\theta$

$$E_{\text{trans}} = E\frac{2\mu}{m_{\text{atom}}}\left(1 - \cos\theta\right). \tag{2.30}$$

Thus, the integral needs to be truncated at

$$\cos\theta_{\text{min, loss}} = 1 - \frac{m_{\text{atom}}}{2\mu}\frac{U_{\text{trap}}}{E}. \tag{2.31}$$

In Fig. 2.5 the resulting $\sigma_{\text{loss}}$ is plotted for three different trap depths $U_{\text{trap}}$. For large $U_{\text{trap}}$ we find $\sigma_{\text{loss}}$ to be smaller than $\sigma_{\text{elastic}}$, since a significant fraction of the collisions take place under a small scattering angle and thus do not directly lead to an atom loss. However, for small trap depths $U_{\text{trap}} \approx 1...3\,\mu\text{K}$ as used in the experiments described in this work, the majority of the collisions leads to the atom being lost from the trap. In this limit the heating of the atomic sample can be neglected and $\sigma_{\text{loss}} \sim \sigma_{\text{elastic}}$.

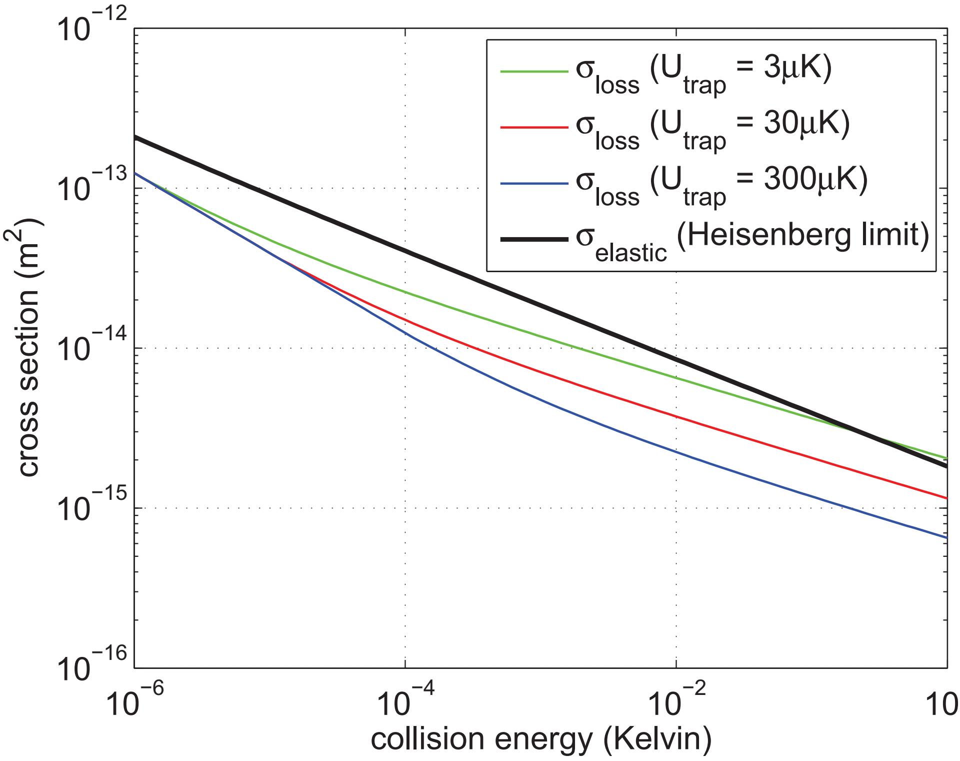

Figure 2.5: The cross section for $\sigma_{\text{loss}} \approx \sigma_{\text{Langevin}} + \sigma_{\text{glancing, loss}}$. The integral for $\sigma_{\text{glancing, loss}}$ is truncated at $\theta_{\text{min, loss}}$, so that only collisions with an energy transfer $E_{\text{trans}} > U_{\text{trap}}$ are contributing. Additionally $\sigma_{\text{elastic}}$ is plotted for comparison.

## 2.3 Quantum mechanical atom-ion collision theory

An important approach to describe the scattering between particles with quantum theory is the method of partial wave expansion. This method is particularly suitable for the case of low collision energies. As can be looked up in any standard quantum mechanics textbook (e.g. [27]), the scattering cross section can be written as

$$\sigma = \sum_{l=0}^{\infty} \sigma_l = \frac{4\pi}{k^2} \sum_{l=0}^{\infty} (2l+1) \sin^2 \delta_l \tag{2.32}$$

where $\sigma_l$ is the contribution of the $l$-th partial wave to the total scattering cross section. The wave vector $k^2 = 2\mu E/\hbar^2$ is set by the collision energy $E$. In general, the scattering phase shifts $\delta_l$ depend on the exact form of the interaction potential and thus also contain all the information about the inner structure of the collision partners.

### 2.3.1 Semiclassical approximation

The following derivation of the semiclassical expression for the elastic scattering cross section is based on the work of Robin Côté and Alex Dalgarno [3]. For large angular-momentum quantum numbers $l \gg 1$, the phase shifts can be approximated by [3]

$$\delta_{l,\mathrm{semi}} = -\frac{\mu}{\hbar^2} \int_{r_0}^{\infty} \frac{V(r)}{\sqrt{k^2 - l^2/r^2}} dr \tag{2.33}$$

where $r_0$ is the classical turning point (see Fig. 2.1). By plugging in the polarization potential $V(r) = C_4/2r^4$, we get

$$\delta_{l,\mathrm{semi}} = \frac{\pi \mu^2 C_4 E}{4\hbar^4 l^3}. \tag{2.34}$$

As can be seen by a comparison with the full quantum mechanical treatment [3], equation (2.34) is valid as long as $\delta_{l,\mathrm{semi}} \approx \sin \delta_{l,\mathrm{semi}} \ll 1$. If we require $\delta_{l,\mathrm{semi}} < \pi/4$, we get a minimum angular momentum $l_{\mathrm{min}}$, for which the semiclassical expression is valid

$$l_{\mathrm{min}} = \left( \frac{\mu^2 C_4 E}{\hbar^4} \right)^{-1/3}. \tag{2.35}$$

For $l < l_{\text{min}}$ the scattering phase shifts $\delta_l$ can only be derived via a full quantum mechanical calculation, taking into account the inner structure of the atom and the ion, respectively. However, in our case, where we take a sum over many partial waves, it is possible to use the mean value $\delta_l = \pi/4$, corresponding to $\sin^2 \delta_l = 1/2$ for all $l \leq l_{\text{min}}$. The resulting cross section contributions are

$$\sum_{l=0}^{l_{\text{min}}} \sigma_l = \frac{2\pi}{k^2} \sum_{l=0}^{l_{\text{min}}} (2l+1) = \frac{2\pi}{k^2} l_{\text{min}}^2 \tag{2.36}$$

and

$$\sum_{l=l_{\text{min}}}^{\infty} \sigma_l = \frac{4\pi}{k^2} \int_{l_{\text{min}}}^{\infty} 2l\delta_{l,\text{semi}}^2 dl = \frac{2\pi}{k^2} l_{\text{min}}^2 \delta_{l_{\text{min}},\text{semi}}^2 = \frac{2\pi}{k^2} l_{\text{min}}^2 \frac{\pi^2}{16}. \tag{2.37}$$

If we take the sum of the equations (2.36) and (2.37) and make use of equation (2.35), we get the semiclassical formula for the elastic scattering cross section

$$\sigma_{\text{elastic}}(E) = \pi \left( \frac{\mu C_4^2}{\hbar^2} \right)^{1/3} \left( 1 + \frac{\pi^2}{16} \right) E^{-1/3}. \tag{2.38}$$

Due to the averaging over many partial waves this expression only depends on the polarizability of the Rb atom and on the collision energy, just as in the classical case. In fact, within the energy range where the semiclassical approximation is assumed to be valid ($E \gtrsim k_B \times 30\mu\text{K}$), the semiclassical values match the classical ones (see Fig. 2.6).

### 2.3.2 Full quantum mechanical treatment

In the ultracold regime, where only a few partial waves contribute to the scattering, quantum mechanical calculations are necessary to determine the relevant phase shifts $\delta_l$. One possible method to describe ultracold atom-ion collisions are numerical coupled-channel calculations [3, 28]. This treatment relies on the singlet and triplet potential curves calculated by *ab initio* methods. Unfortunately, these potential curves are usually not accurate enough to determine the scattering lengths. An alternative approach is to apply the multichannel quantum defect theory (MQDT) to the atom-ion scattering problem [19]. In this case, it is not necessary to know the potential curves precisely. It is sufficient to know the singlet and the triplet scattering lengths $a_s$ and $a_t$ and the long-range behavior of the potential. Since the experiments are not yet able to give estimates for these ultralow-energy scattering parameters, typical values on the order of $r^*$ are

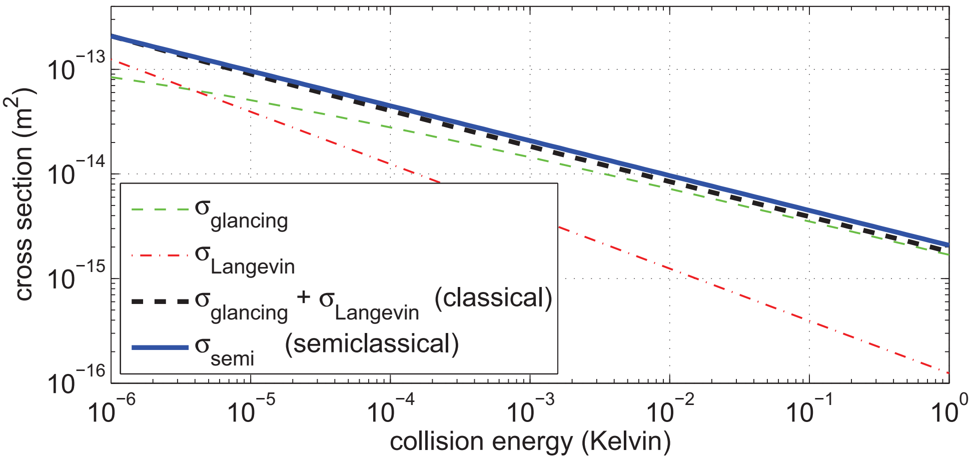

Figure 2.6: Comparison of the semiclassical cross section (equation (2.38)) with the classical one, which is obtained by truncating the integral for $\sigma_{\mathrm{glancing}}$ at the Heisenberg limit (see above). The two results are almost identical, both showing a $E^{-1/3}$ dependence on the collision energy.

assumed for $a_s$ and $a_t$.

Zbigniew Idziaszek and co-workers have performed MQDT calculations for the $^{40}$Ca$^+$ - $^{23}$Na system [19] and also for our $^{138}$Ba$^+$ - $^{87}$Rb setup [29]. The results for our system are depicted in Fig. 2.7. We recognize three different regimes: For energies larger than $10^{-10}$ atomic units (corresponding to $\sim$ 30µK) the MQDT calculation can be well approximated by the semiclassical formula. For smaller energies, however, $\sigma_{\mathrm{elastic}}$ deviates from the simple $E^{-1/3}$-dependence and crucially depends on $a_s$ and $a_t$. Finally, for collision energies in the nK range, $\sigma_{\mathrm{elastic}}$ becomes energy-independent, indicating the start of the s-wave scattering regime. As expected, the right order of magnitude can be estimated with $\sigma_{\mathrm{elastic}} \sim 4\pi r^{*2} \approx 1 \times 10^{-12}\,\mathrm{m}^2$. In addition to $\sigma_{\mathrm{elastic}}$, also the elastic collision rate $\Gamma_{\mathrm{elastic}} = v\sigma_{\mathrm{elastic}}$ is shown in Fig. 2.7. Here $v = \sqrt{2E/\mu}$ is the relative velocity between the ion and the atom.

Similar as the case of the atom-atom interaction [25], the strength of the atom-ion interaction is expected to be tunable with magnetic fields. The MQDT predicts the occurance of magnetic Feshbach resonances at relatively low fields [19, 29]. According to this calculation the scattering resonances should stay observable well above the s-wave regime. In particular, by measuring charge exchange rates, resonant behavior might be visible up to collision energies of tens of µK [29].

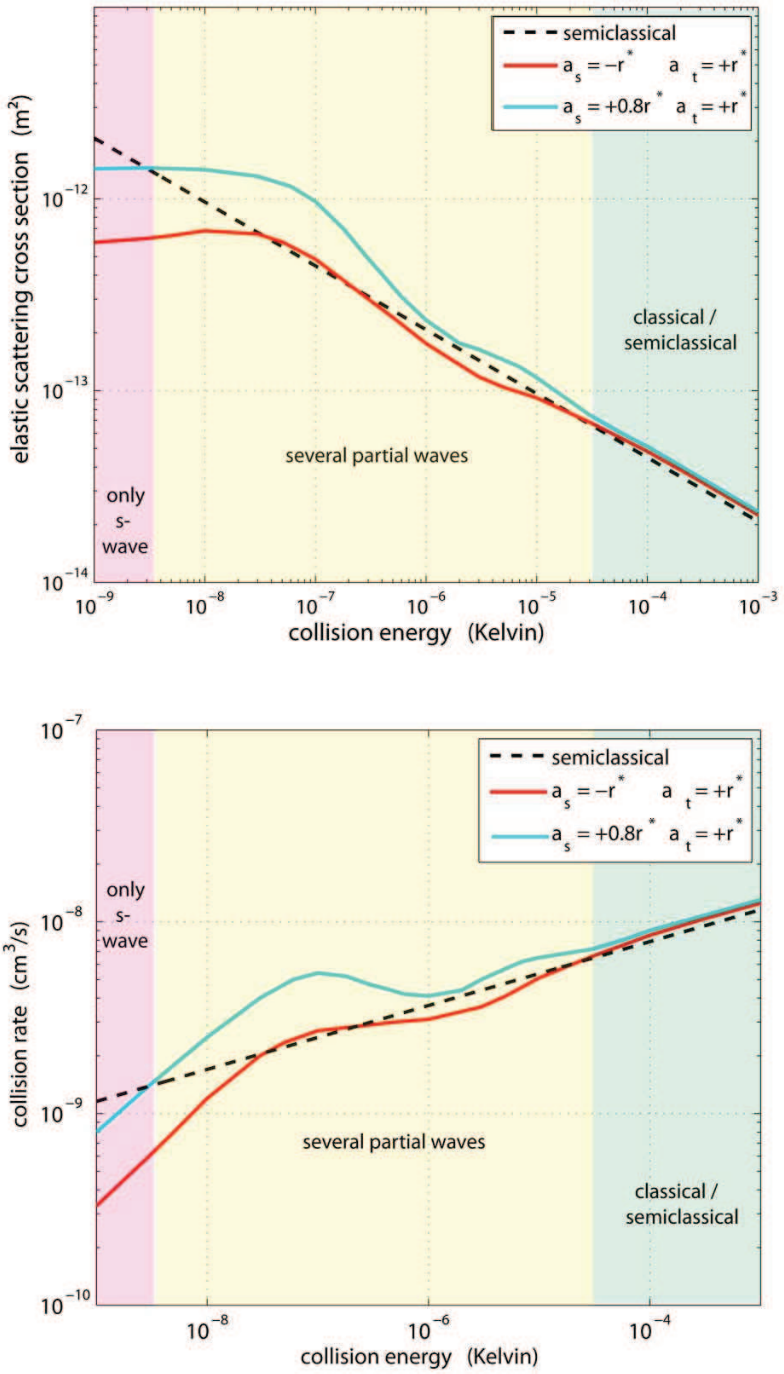

Figure 2.7: Thermal average of the elastic scattering cross section (*upper plot*) and of the elastic collision rate (*lower plot*), both calculated with the multichannel quantum defect theory (MQDT) by Zbigniew Idziaszek and co-workers [19, 29]. Since $a_s$ and $a_t$ are not known, we plot $\sigma_{\text{elastic}}$ and $\Gamma_{\text{elastic}}$ for $a_s$ and $a_t$ having the same sign and for having a different sign, respectively. Here $r^*$ is the characteristic radius given by equation (2.10). Additionally the MQDT result is compared with the semiclassical approximation (dashed line).

# Chapter 3

# Experimental setup

In this chapter I would like to present all the important details about our experimental apparatus. I will start with a description of our vacuum system. Then I will explain how we generate the magnetic fields and the optical laser fields, respectively, required for the manipulation of the cold atoms and ions. Eventually, I will describe how we control the experimental procedures.

## 3.1 The vacuum system

A novel vacuum setup was designed to study the interaction between ultracold atoms and cold trapped ions. The central idea of our hybrid apparatus is the spatial separation of the BEC apparatus, where the ultracold atoms (or a BEC) are produced, from the ion-trapping region, where the atom-ion collision experiments are performed. This way we keep all the elements needed for atom cooling (such as coils or optical components) away from the ion trapping region and gain valuable optical access to the "science section", that is required to trap, manipulate, and detect the atoms and ions. Moreover, with a macroscopic separation of 30 cm we are able to avoid the mutual disturbance between the radiofrequency (RF) Paul trap and the RF used for forced evaporative cooling of the atomic sample. Alternatively, it is also possible to perform the rf evaporation right next to the Paul trap, which allows for a simpler design of the vacuum apparatus. However, one major drawback of such a solution is the resonant heating of the ions due to the rf radiation needed for the evaporative cooling of the atoms [8, 30].

The three main building blocks of our vacuum system are the MOT chamber, the BEC chamber and the science chamber (Fig. 3.1). The latter one is placed about 30 cm above the lower plane of the setup, in which the MOT and the BEC

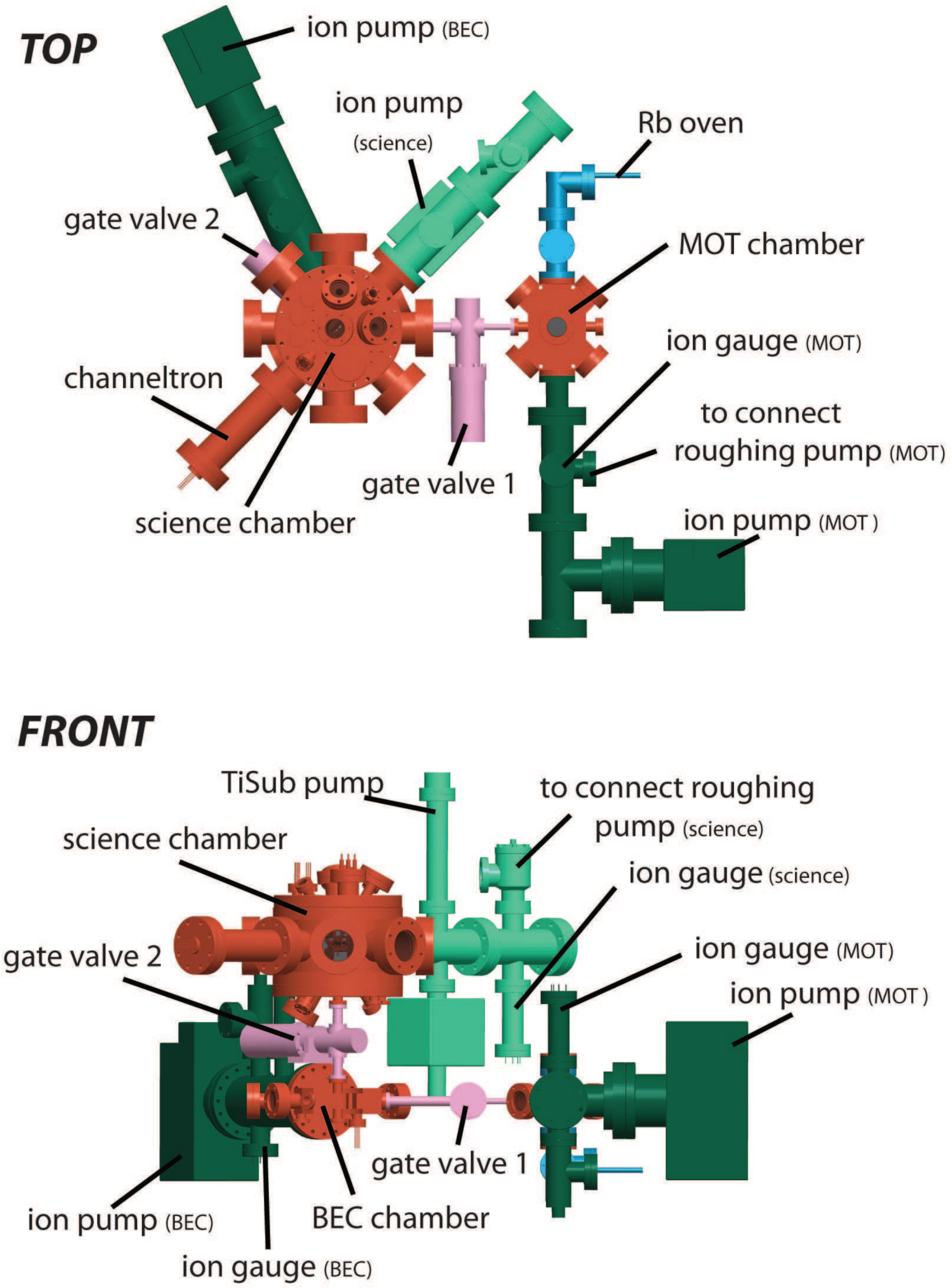
TOP
ion pump (BEC)
ion pump
(science)
Rb oven
gate valve 2
MOT chamber
ion gauge (MOT)
channeltron
to connect
roughing pump (MOT)
gate valve 1
science chamber
ion pump (MOT )
FRONT
TiSub pump
to connect roughing
pump (science)
science chamber
ion gauge (science)
gate valve 2
ion gauge (MOT)
ion pump (MOT )
gate valve 1
ion pump (BEC)
BEC chamber
ion gauge (BEC)

Figure 3.1: Overview of the vacuum system: The MOT chamber, the BEC chamber and the science chamber (red) are connected via two differential pumping stages (purple). Each chamber is evacuated by its own pumping section (green) and can be separated from the rest by closing the gate valves.

chamber are located. To bring the ultracold atoms from their place of production (BEC chamber) to the ion trap (science chamber), a reliable transport scheme is required. We have chosen a 1-d moving optical lattice transport for this task. Further details on this moving standing wave transport and an explanation why the science chamber is not placed near the BEC chamber but above it, are given in section 5.2.2.

The three vacuum vessels (MOT, BEC, science) are connected with each other via two differential pumping stages. Furthermore, a series of vacuum gauges, pumps and valves is used to evacuate the system and to determine the pressure. In fact, UHV conditions with pressures around or below $10^{-11}$ mbar have initially been established in all three chambers. In order to achieve such low pressures it was necessary to bake out the setup at temperatures between 180°C and 250°C. Moreover, a He leak test was performed using an electron-multiplied residual-gas-analyzer (RGA100 from Stanford Research Systems).

### 3.1.1 Lower level: Cold atom section

The lower level of the apparatus is entirely used for the production of the BEC. In the MOT chamber the atoms are loaded from the surrounding background gas ($p_{\mathrm{MOT}} \approx 10^{-9}$ mbar) into a magneto-optical trap. Subsequently the atoms are moved through a differential pumping tube into the BEC chamber, where the pressure $p_{\mathrm{BEC}} \approx 10^{-11}$ mbar is low enough to keep the atoms trapped for more than $10^2$ seconds.

#### MOT chamber

The MOT chamber is a home-made stainless steel (AISI 316L) vacuum vessel, which features ten optical viewports. Most of the ports (six) are required for the MOT beams, whereas the rest of them are needed to connect the Rb oven, to pump out the chamber and to move the atoms out of the MOT chamber towards the BEC chamber. In order to keep the chamber under ultrahigh vacuum (UHV) conditions an ion getter pump (Varian StarCell 75 l/s) is used and the pressure is determined with an Bayard Alpert type UHV pressure gauge (UHV-24p from Varian).

The Rb oven consists of a stainless steel tube, which is welded to a small hole of a blank flange. Since Rb is very reactive when exposed to air, a special procedure for putting it into our system is followed. An ampule filled with bulk

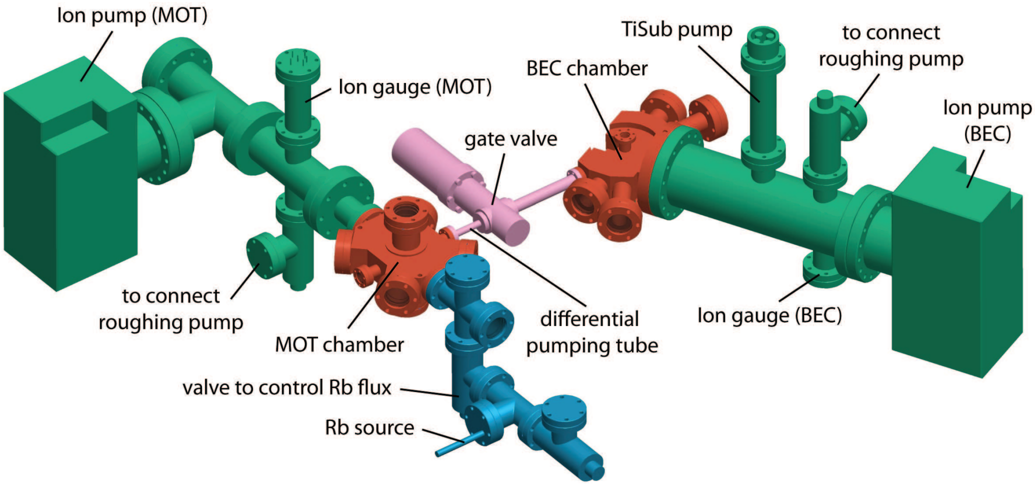
Ion pump (MOT)
Ion gauge (MOT)
TiSub pump
BEC chamber
to connect roughing pump
Ion pump (BEC)
gate valve
to connect roughing pump
MOT chamber
differential pumping tube
Ion gauge (BEC)
valve to control Rb flux
Rb source

Figure 3.2: Vacuum system to produce a ultracold cloud of Rb atoms. The MOT section (left) and the BEC section (right) are separated by a differential pumping stage (middle/pink). The pressure in the MOT section is fully determined by the Rb vapor entering from the Rb oven (blue) and is more than a factor of 100 larger than the pressure in the BEC section.

Rb and He as an inert gas (Sigma-Aldrich Part-No 276332-1G) is put into the tube. Then after evacuating the system the ampule is cracked by pinching the thin-walled stainless steel tube. The helium is pumped out and the pressure in the oven is determined by the vapor pressure of Rb, which is $4\times10^{-7}$ mbar at room temperature. The pressure close to the ion pump is measured with the UHV gauge to be about $1\times10^{-9}$ mbar. Since the MOT chamber is in between the oven and the pumping section we estimate the pressure $p_{\text{MOT}}$ to be a few times $10^{-9}$ mbar. Such a high Rb vapor pressure is necessary in order to be able to load the MOT from the background gas. If necessary, the value for $p_{\text{MOT}}$ can be adjusted by heating the oven or by changing the setting of the valve, which connects the oven with the MOT chamber.

### Differential pumping stage

In order to keep the pressure in the BEC chamber $p_{\text{BEC}}$ two orders of magnitude lower than $p_{\text{MOT}}$ we separate the two chambers with a differential pumping tube. We determine the required length $L$ and diameter $D$ of the tube by making the following estimate. The rate at which the BEC chamber is evacuated can be written as $S_{\text{BEC}}\,p_{\text{BEC}}$, where $S_{\text{BEC}} = 75\,\text{l/s}$ is the pumping speed of the ion pump.

In equilibrium, the pump rate has to be equal to the flux of molecules entering through the differential pumping tube

$$S_{\mathrm{BEC}} p_{\mathrm{BEC}} = C(p_{\mathrm{MOT}} - p_{\mathrm{BEC}}), \tag{3.1}$$

where the conductance of the tube is given by

$$C \approx a \frac{D^3}{L}, \qquad a = 12\,\mathrm{l/s\,cm^2}. \tag{3.2}$$

Here we have neglected any leak rates as well as desorption from the chamber walls, which is a valid assumption for a baked-out and leak-free UHV system. From equation (3.1) we conclude, that for sustaining a large pressure gradient we have to minimize the conductance and thus the diameter of the tube. The lower limit of how small we can make the diameter of the tube is given by the size of the atom cloud, which we want to transport through the tube. Since the extension of the cloud is on the order of a few millimeters, we choose $D = 8\,\mathrm{mm}$. With equations (3.1) and (3.2) we then find a tube length of $L = 115\,\mathrm{mm}$ to be sufficient to maintain the required vacua.

### BEC chamber

Our BEC chamber features a non-standard geometry, which fulfills the following list of demands.

- We require space for mounting a QUadrupole-Ioffe-Configuration (QUIC) trap outside the chamber. For this purpose two quadrupole coils with an inner diameter of 39 mm and an outer diameter of 88 mm need to be placed as close as 15 mm from the center of the chamber. In addition we have to place the Ioffe coil at a distance of 11.2 mm from the center.
- We want to have full optical access along the vertical direction (quadrupole axis), in order to be able to implement the optical transport of the ultracold atoms. In this context "full optical access" means, that we have optical access to the center of the chamber as well as to the atoms, when they are loaded into the minimum of the QUIC trapping potential. The latter position is located on the Ioffe axis, typically about 5 mm away from the center of the chamber towards the Ioffe coil.
- We require full optical access along the direction perpendicular to the vertical and the Ioffe axis, needed for imaging of the ultracold atoms.

- Optical access along the magnetic transport axis is desired, since we want to have the possibility to image the atom cloud at any intermediate position of the magnetic transport. This feature is not mandatory for a running experiment, though, it can be crucial when the magnetic transport is not working properly. Moreover, we require this optical access to send spinpolarizing light through the BEC chamber and the differential pumping tube to the MOT chamber. With this laser beam we spinpolarize the atoms after molasses cooling and before loading them into the magnetic quadrupole trap.
- We also want to have optical access to the center of the chamber along an additional third axis in the horizontal plane. This axis was designed to have the possibility to implement a "blue-detuned plug beam" [31]. With such a plug beam Majorana spin flip losses can be suppressed, which enables evaporative cooling and the creation of Bose-Einstein condensates in a magnetic quadrupole trap. We actually never added a plug beam to our setup, since the operation of our QUIC trap turned out to be successful and reliable.
- One large port to efficiently evacuate the BEC chamber.

To meet all the requirements listed above, we have designed the BEC chamber as shown in Fig. 3.3. The chamber features DN40CF flanges on both ends of the imaging axis, which are large enough not to distort the absorption beam and to allow for a good imaging quality. Along the vertical axis DN16CF flanges are used, so that the QUIC quadrupole coils can be mounted as desired. In order to utilize the large pumping speeds of the ion pump and the TiSub pump, respectively, we use a DN100CF flange to connect the pumping section to the BEC chamber.

Having the BEC chamber connected along three different directions in space (to the MOT chamber, the science chamber and the pumping section), leads to shear forces on the chamber. When using a glass cell these shear forces can lead to a leak or even a crack of the recipient. Thus we have decided to use a stainless steel chamber, even though a glass cell would have provided much better optical access.

The pressure in the BEC chamber is kept below $10^{-11}$ mbar, which is sufficient to achieve lifetimes of the atom cloud of more than 2 min. To reach these X-UHV conditions in the BEC chamber a combination of a titanium sublimation (TiSub)

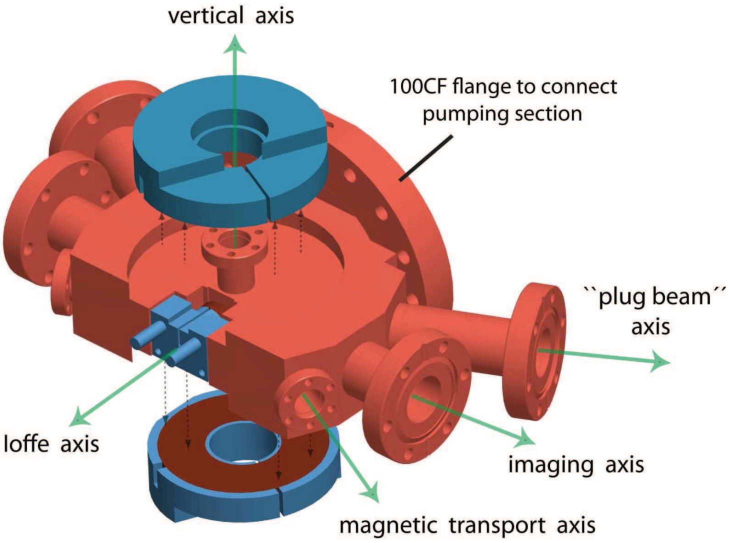
vertical axis
100CF flange to connect pumping section
``plug beam´´ axis
Ioffe axis
imaging axis
magnetic transport axis

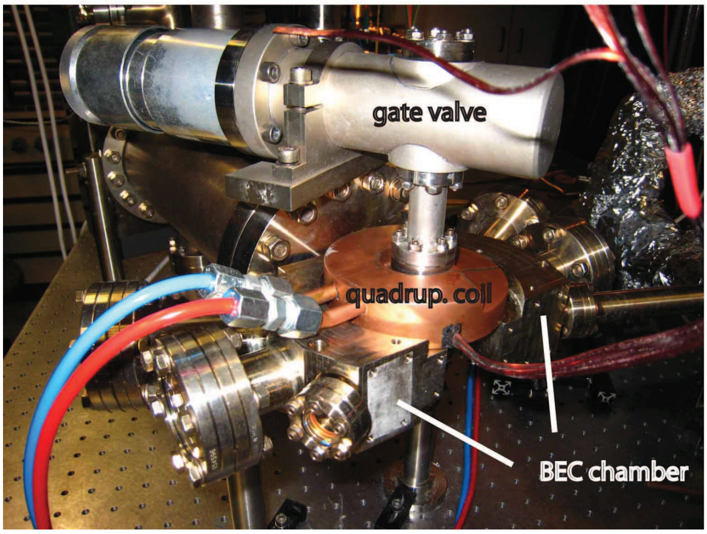
gate valve
quadrup. coil
BEC chamber

Figure 3.3: *Top:* BEC chamber together with the coils for the QUIC trap (blue housing). The coils are mounted outside the vacuum system and as close as possible to the center of the BEC chamber. The atoms enter the chamber along the magnetic transport axis and leave it again along the vertical axis. *Bottom:* Photo of the BEC chamber together with the (water-cooled) upper quadrupole coil (copper housing) and the gate valve, with which the BEC chamber and the science chamber are separated from each other.

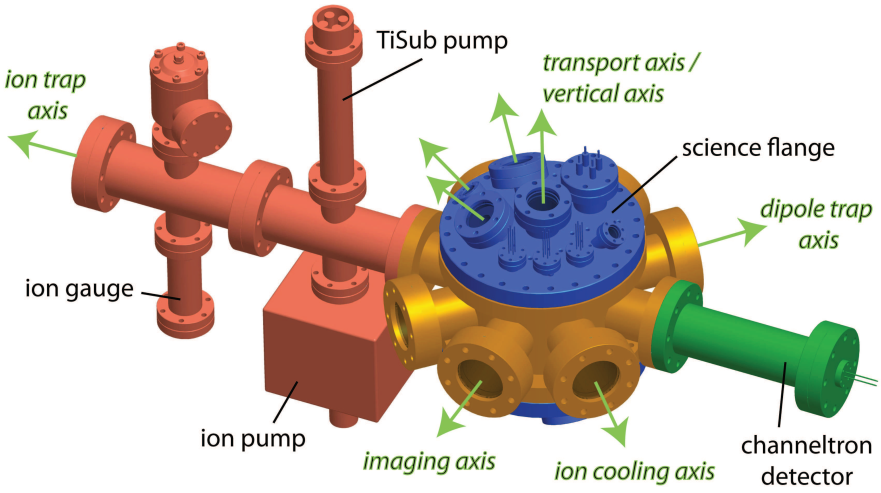
ion trap axis
TiSub pump
transport axis / vertical axis
science flange
dipole trap axis
ion gauge
ion pump
imaging axis
ion cooling axis
channeltron detector

Figure 3.4: The two DN200CF flanges (blue) are mounted on top and on the bottom of the science chamber (golden). The pumping section (red) and the channeltron detector (green) are connected via DN63CF ports. Our eight optical axes are indicated with green arrows.

pump (TSP filament type from Varian) and an ion getter pump (Varian StarCell 75 l/s) is used to efficiently pump out a variety of different gases. The TiSub pump works particularly well for adsorbable gases such as $N_2$ and water, whereas the ion pump is optimized for pumping non-adsorbable gases such as He. Since we baked out our system thoroughly, most of the adsorbable gases are removed from our system. To sustain X-UHV conditions in our chamber it is thus sufficient to only operate the ion pump.

### 3.1.2 Upper level: Ion trapping and science section

The science chamber (Fig. 3.4) is the heart of our vacuum setup and is designed for maximum optical access with 8 optical axes. The optical access is needed for cooling and imaging of the ions as well as for trapping, manipulating and imaging of the atoms. The octagon-shaped science chamber is made out of stainless steel (AISI 316L) and evacuated with a combination of an ion getter pump and a Titanium sublimation pump. During experiments, when the Ba oven is turned off, the pressure in the science chamber drops to typically $1{\times}10^{-11}$mbar. The pumping section is connected to one end of the ion trap axis and a channeltron

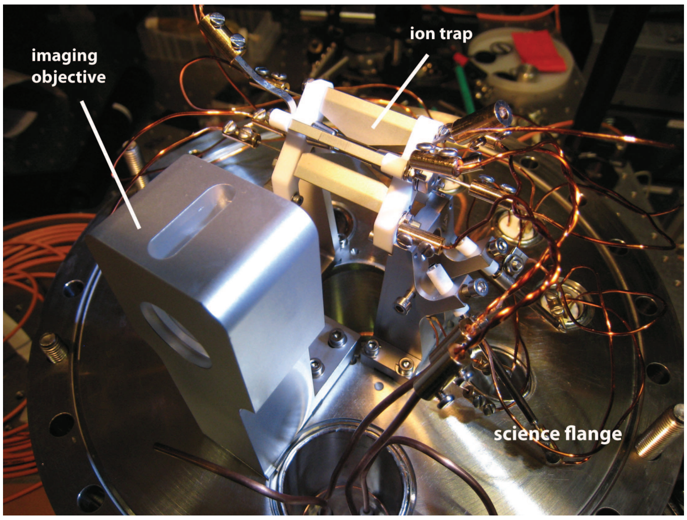

Figure 3.5: The imaging objective and the entire ion trap are directly mounted onto the "science flange". The flange is then put on top of our science chamber.

ion detector (CEM-4823G from Burle) to the other end. The channeltron can be used to identify ions via time-of-flight (TOF) mass spectrometry.

All parts of the ion trap as well as the objective required to image the ions and the atoms are mounted onto the so-called "science flange" (see Fig. 3.5). This CF200 flange also features various electrical feedthroughs, which are needed to apply the required voltages to the Paul trap electrodes and to run currents of up to 12 A through our Ba oven. The flange is put on top of the science chamber.

## 3.2 Generation of magnetic fields

Magnetic fields are an essential tool in our experiments. They are needed to trap and to transport the neutral atoms. Moreover, it has been shown theoretically that in the ultracold regime (i.e. for sufficiently low kinetic energies) the strength of the atom-ion interaction can be tuned via magnetic fields [19] (see also chapter 2).

Self-made coils and four 3 kW power supplies (Delta Elektronika SM15-200D and SM30-100D) are used to generate the magnetic fields. All the coils (except for the compensation cages, where we have simply used ribbon cable) are wound with an enameled copper wire (from the company Synflex), which has a cross section of $1.2 \times 2.5\,\mathrm{mm}^2$. Subsequently the coils are potted with an epoxy casting resin (Raku-Pur 21-2176 from the company Rampf Giessharze). This epoxy was

Table 3.1: Properties of our home-made magnetic field coils

| coil | MOT | Push | Transport | Quadrupole | Ioffe | Feshbach |
|---|---|---|---|---|---|---|
| inner ∅ (mm) | 70 | 38 | 47 | 39 | 6.7 | 130 |
| outer ∅ (mm) | 107 | 48 - 67 | 130 | 88 | 16.5 - 21.4 | 147 |
| windings | 2 × 15 | 40 | 2 × 17 | 4 × 20 | 16 | 2 × 15 |
| distance (mm) | 25 | 57 | 50 and 57 | 16.5 | 11 | 63 |
| current (A) | 5 or 80 | 90 | 45 - 80 | 37 | 37 | - |
| housing | Al | Al | Al | Cu | Cu | Al |

chosen due to its exceptionally high thermal conductivity of 0.8 W/(m K). We have done the potting under vacuum using a bell jar. This way we have avoided blowholes, which would worsen the heat conductivity. The coil forms are water cooled and typically made of aluminum (Al), which has a thermal conductivity of $\lambda_{\mathrm{Al}} = 235\,\mathrm{W/m\,K}$. An exception are the housings of our QUIC coils (two quadrupole coils and the Ioffe coil), which are made of copper (Cu). Cu is more expensive than Al, however, it also features a much higher thermal conductivity of $\lambda_{\mathrm{Cu}} = 400\,\mathrm{W/m\,K}$, as compared with Al. The copper housing allows to dissipate about 530 W (steady state), corresponding to a maximal operating current of our QUIC of 37 A. A complete list of our magnetic field coils and their properties is given in table 3.1.

## 3.3 Laser systems

In our experiment we predominantly use diode lasers to prepare our cold ions and atoms. The big advantages of diode lasers are the low cost and the easy handling, as compared with other types of lasers. Therefore they are well suited for laser cooling of atoms and ions, where high frequency stability but usually only a rather small amount of power is needed. In contrast, a fiber-amplified solid state laser is employed for high power applications, such as the optical transport or the crossed dipole trap.

### 3.3.1 Rb lasers

We have set up two home-built external cavity diode lasers ("Master" and "Repumper") tuned to the $5^2\mathrm{S}_{1/2} \rightarrow 5^2\mathrm{P}_{3/2}$ transition of Rb (Fig. 3.6). By splitting their outputs we derive ten different beams from these two lasers (Fig. 3.7). Each beam is frequency-shifted using acousto-optical modulators (AOMs) and subse-

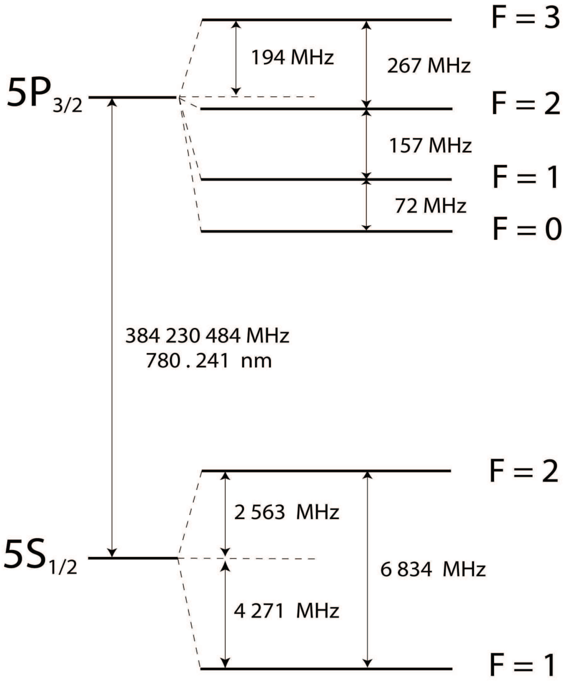

Figure 3.6: The $D_2$ line of $^{87}$Rb: The values for the main transition frequency and for the hyperfine splittings given here are taken from [32].

quently coupled into a polarization-maintaining single-mode glass fiber. This way we are able to transfer the beams from the laser table to the experiment table, where they are used for the cooling, manipulation and detection of the Rb atoms.

### Master laser

The Master laser features an anti-reflection (AR) coated laser diode (eagleyard EYP-RWE-0780-02000) and a holographic grating with 1200 lines/mm and a diffraction efficiency of roughly 10 % (EdmundOptics NT43-772). Using an AR coated laser diode leads to a wide mode-hop-free frequency tuning range and ensures stable lasing so that the laser can be kept locked for several days. Together, the laser diode and the grating determine the frequency stability of our home-made diode lasers. The resulting spectral linewidth is typically on the order of 100 kHz.

The frequency of the Master is locked to the $|\,F = 2\rangle \rightarrow |\,F' = 3\rangle$ transition of $^{87}$Rb via modulation transfer spectroscopy. For this purpose we have set up a doppler-free spectroscopy, where we additionally modulate the pump beam at a frequency on the order of the natural linewidth of the transition (6 MHz). The

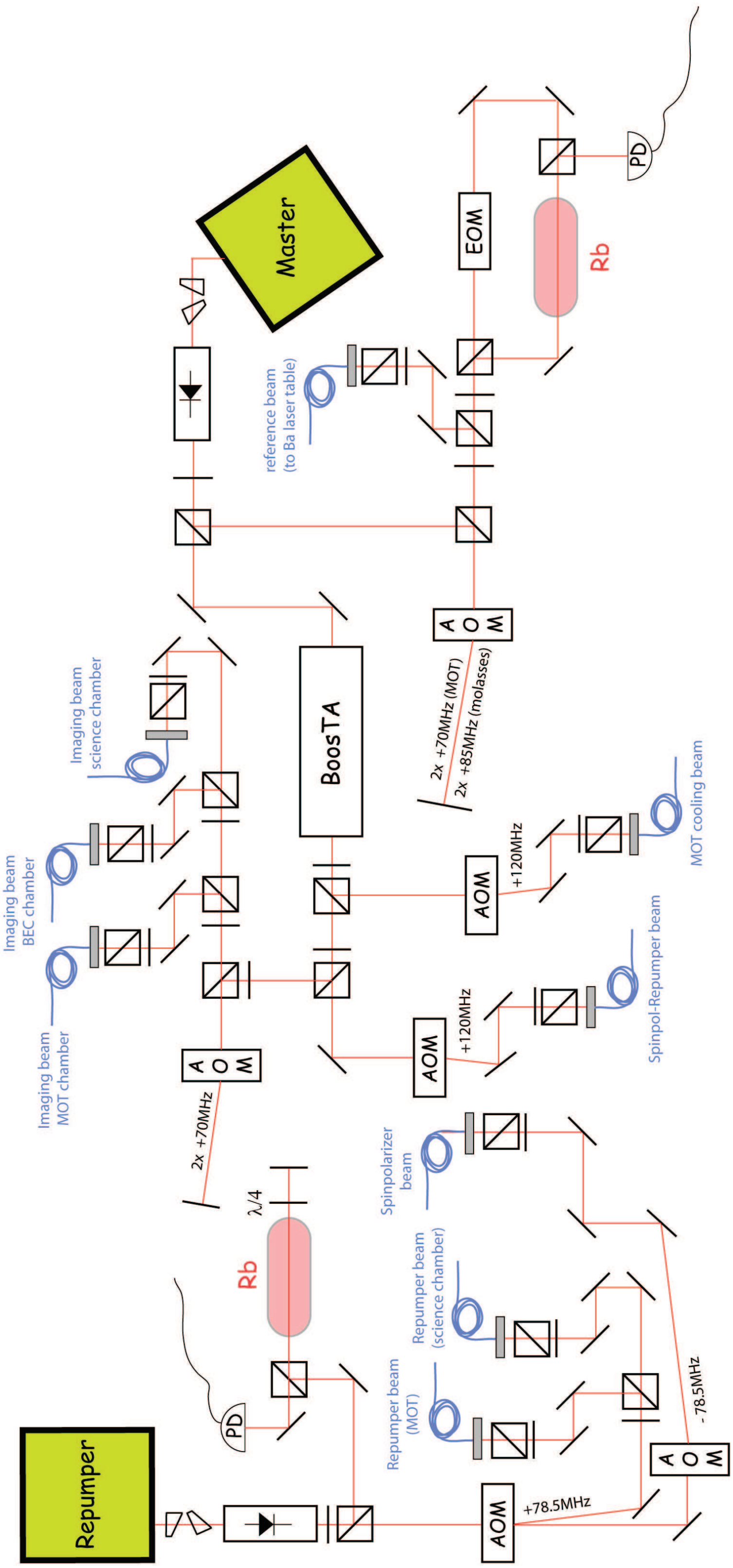
Master
reference beam
(to Ba laser table)
EOM
Rb
PD
BoosTA
A O M
2x +70MHz (MOT)
2x +85MHz (molasses)
AOM
+120MHz
MOT cooling beam
AOM
+120MHz
Spinpol-Repumper beam
Imaging beam
science chamber
Imaging beam
BEC chamber
Imaging beam
MOT chamber
A O M
2x +70MHz
λ/4
Rb
PD
Repumper
Spinpolarizer
beam
Repumper beam
(science chamber)
Repumper beam
(MOT)
-78.5MHz
A O M
AOM
+78.5MHz

Figure 3.7: Rb laser table: Altogether ten laser beams, derived from two different diode lasers are required for the laser cooling and the detection of Rb.

spectroscopy signal is detected with a fast photodiode (bandwidth = 100 MHz) and then mixed with the modulation signal (see Fig. 3.7). The output of the mixer is low-pass filtered and can then be used as an error signal for the stabilization of the laser frequency. For more details on the modulation transfer technique see for example [33].

For the spectroscopy setup we need about 5 mW of laser power. Another 3 mW of the light from the master laser are transferred to the $Ba^+$ laser table, where the light is used as an absolute frequency reference to which the $Ba^+$ lasers are locked. The rest of the master light (about 20 mW) is amplified with a tapered amplifier (BoosTA from the company Toptica). The majority of the 800 mW of laser power available at the output of the BoosTA is used for the MOT cooling beams, whereas small fraction (a few mW) is employed for absorption imaging of the atoms.

#### Repumper laser

Via the frequency modulation (FM) technique [34] the repumper is locked to the $|\,F=1\rangle \rightarrow |\,F'=1\rangle/|\,F'=2\rangle$ cross over line. The frequency of the repumping light is then shifted to the $|\,F=1\rangle \rightarrow |\,F'=2\rangle$ resonance using an AOM. A total repump power of $6{\times}1.5$ mW is employed to operate the MOT. The rest of the light (about 1 mW) is needed for spin-polarizing and during imaging of the atoms, respectively.

Here I would like to point out that we were initially having troubles with bad interferences between the stabilization electronics of our home-built lasers and the rf used to drive the Paul trap. However, we were able to solve these problems by avoiding ground-loops when powering our electronics and by getting rid of circuit elements that directly pick up the 5 MHz radiofrequency (such as for instance the instrumental amplifier INA114 used in our temperature controllers).

### 3.3.2 $Ba^+$ lasers

#### Cooling laser

For the Doppler cooling of the $^{138}Ba^+$ ion a few mW of laser light at 493 nm are required (see Fig. 3.9). Since there are no laser diodes available at this wavelength the cooling light is generated via frequency-doubling of a 986 nm diode

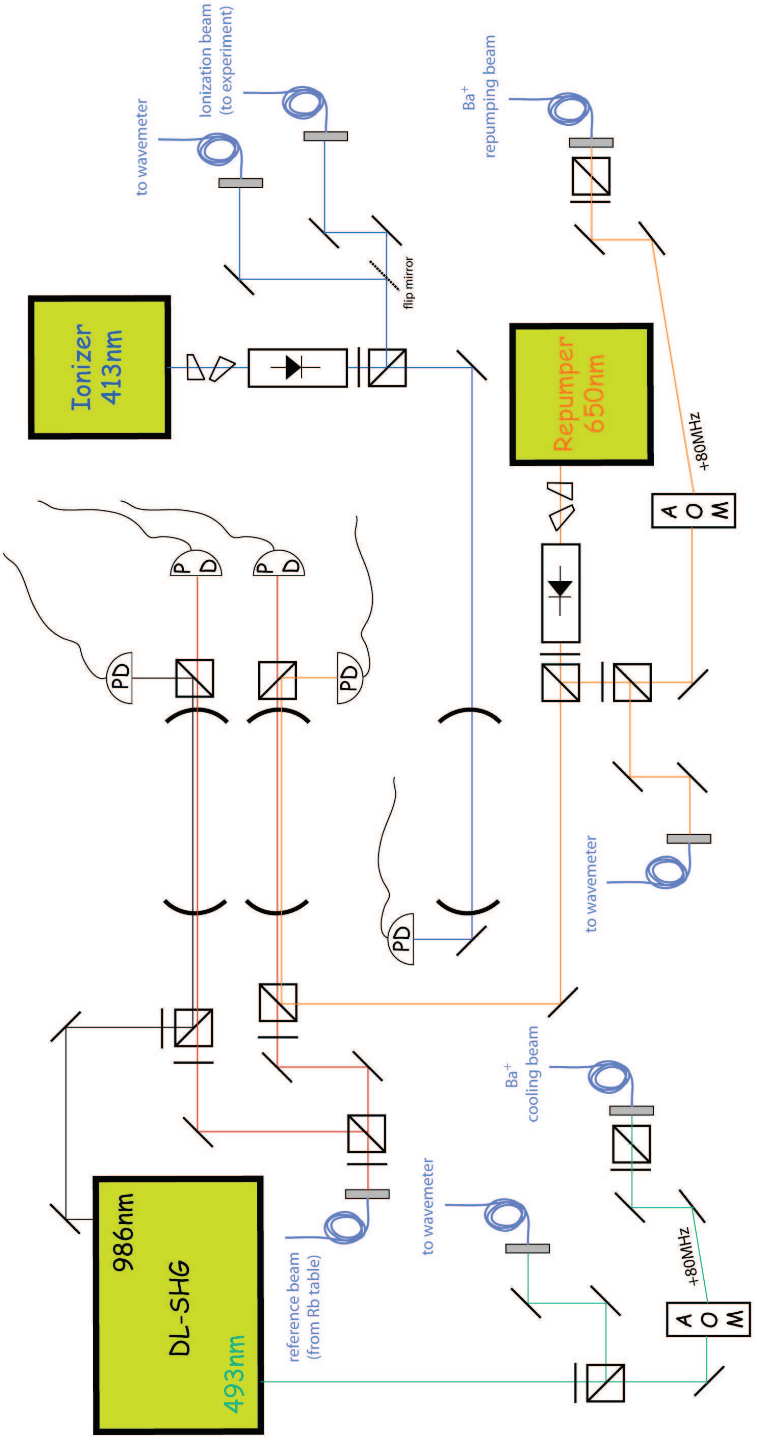
to wavemeter
Ionization beam
(to experiment)
Ba+
repumping beam
flip mirror
Ionizer
413nm
Repumper
650nm
+80MHz
AOM
PD
PD
PD
PD
PD
to wavemeter
Ba+
cooling beam
to wavemeter
+80MHz
AOM
986nm
DL-SHG
493nm
reference beam
(from Rb table)

Figure 3.8: $Ba^+$ laser table: An ionization laser (413 nm) as well as two cooling lasers (493 nm and 650 nm) are used to prepare the $Ba^+$ ion. The cooling lasers are locked relative to the Master laser (780 nm) using optical resonators.

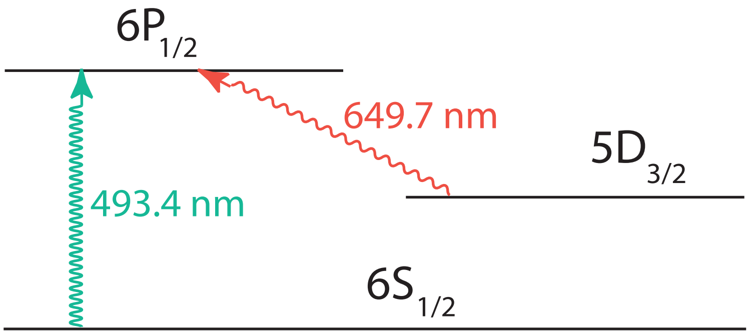

Figure 3.9: Relevant energy levels for Doppler cooling of $^{138}\mathrm{Ba}^+$: Two laser frequencies (493.4 nm and 649.7 nm in air) are required to cool $\mathrm{Ba}^+$ to mK temperatures. The linewidths are $\Gamma_{\mathrm{cool}}/(2\pi) = 15.1\,\mathrm{MHz}$ for the 493 nm transition and $\Gamma_{\mathrm{repump}}/(2\pi) = 5.3\,\mathrm{MHz}$ for the 650 nm transition. Therefore the ion decays into the ground state about 75% of the time and into the metastable $5\mathrm{D}_{3/2}$ state about 25% of the time.

laser. Both the diode laser and the frequency-doubling stage are part of the commercially available system “DL SHG” from the company Toptica. To stabilize the frequency of the 493 nm light, 986 nm laser light is coupled into a stabilization cavity, together with the 780 nm master laser. Since the master laser is already stabilized to an atomic transition ($|\,F = 2\rangle \rightarrow |\,F' = 3\rangle$ in Rb), it serves as a frequency reference. The cavity is scanned continuously and transmission peaks for both the 986 nm and the 780 nm laser are recorded. The frequency of the 986 nm and thus also of the 493 nm light is then stabilized by keeping the position of a 986 nm cavity transmission peak fixed with respect to two consecutive 780 nm peaks. We calculate the relevant time differences between the peaks and subsequently the error signal using home-built digital electronics. The feedback loop is closed by adding the error signal to the offset voltage on the piezo-electrical transducer (PZT) of the diode laser. The bandwidth of this locking scheme is limited by the frequency with which the cavity is scanned and is thus only on the order of 10 to 100 Hz. For this reason we can only correct slow thermal drifts of the laser frequency. For ordinary Doppler cooling our stabilization scheme is sufficient, since the spectral linewidth of the 493 nm light is a few hundred kHz and thus well below the linewidth of the cooling transition of 15.1 MHz (see section 4.2.2.

### Repumping and ionization laser

For the cooling of the $\mathrm{Ba}^+$ ion we additionally need a second cooling laser at 650 nm. Since the branching ratio between the 650 nm transition and the 493 nm transition is 1:3, this laser is usually called repumping laser (Fig. 3.9). We derive the 650 nm light from a home-built external cavity diode laser, which features an anti-reflection coated laser diode to guarantee stable lasing at the desired wavelength. The locking scheme to stabilize the frequency of the repumper is the same as for the 986nm laser.

The ionization laser is a commercially available external cavity diode laser (DL100 from Toptica). It features a blue laser diode to generate up to 12 mW of coherent light at 413 nm. The neutral Ba is ionized by the 413 nm radiation, which drives a resonant two-photon transition from the ground state to the continuum via the $^3\mathrm{D}_1$ state. For more details on the ionization procedure and on the ion loading I would like to refer to section 4.2.1.

### Stabilization cavities

The stabilization cavities are required to keep the frequency of the $\mathrm{Ba}^+$ lasers fixed. For each of our four cavities we have drilled a hole through a ultralow expansion glass (ULE) block. Due to its extraordinarily low expansion coefficient (on the order of $10^{-10}$/K) this material is well-suited for keeping the cavity mirrors in place. The length of the block and thus the length of the cavity is $L = 10\,\mathrm{cm}$, leading to a free spectral range of $\mathrm{FSR} = c/2L = 1.5\,\mathrm{GHz}$. In order to be able to vary the length of the cavity (on the micrometer scale) ring-shaped piezo-electrical transducers (PZTs) are mounted in between the ULE block and the cavity mirrors.

Our ULE block is put into a vacuum tube (size 63CF), which gets sealed with AR-coated viewports at both ends. This way we avoid changes of the cavity length due to variations of the surrounding atmospheric pressure. Moreover the temperature of the vacuum tube is stabilized with mK precision using a heating wire, which we have wound around the tube. In order to keep influences of air flows or fast changes of the surrounding air temperature small we have put the vacuum tube into a polystyrene housing.

The cavity mirrors have a radius of curvature of 250 mm and are specified to have a reflectivity of $R \approx 99\%$. From this value we expect the finesse to be $F = \pi R/(1 - R) \approx 310$ and therefore the cavity linewidth to be FSR/F =

4.8 MHz. The measured value of the cavity linewidth is slightly lower (5.8 MHz), which corresponds to a finesse of $F \approx 260$.

### 3.3.3 High power laser system for atom trapping

For the optical trapping and the transport of the ultracold atom cloud we employ a far-red detuned (from the atomic resonance) high power laser. The main idea of our high power laser system is to optically amplify the output of a commercially available narrow-band laser source. As a source we use a 2 W solid state laser (Mephisto) from the company Innolight. This single-frequency laser has an emission wavelength of 1064 nm and a spectral linewidth below 1 kHz. By changing the temperature of the crystal the laser frequency can be tuned over a range of 30 GHz (tuning coefficient = -3 GHz/K).

The light from the Mephisto is seeded into an amplifying fiber, which is optically pumped from the opposite end of the fiber using high-power laser diodes. Pumping the fiber in the absence of the seed beam leads to an irreparable damage of the amplifying fiber. For this reason a safety circuit was implemented, which shuts the pumping laser down when either the power of the seeding beam is to low or when the power at the fiber output is fluctuating too much. All components of the fiber amplifier, including the safety circuit, the entire control electronics for the pumping laser as well as the housing for the fiber and the pump laser are home-built.

The output beam of the amplifier has a total power of up to 10 W and is split into three beams, with which we generate the 1d optical lattice as well as the crossed optical dipole trap.

## 3.4 Experimental control

In our experiment we use an inexpensive and powerful control system mainly developed by our research colleagues Florian Schreck and Gerhard Hendl [35].

The hardware includes circuit boards for digital and analog outputs (16-bit DACs). The outputs are required to trigger our cameras and to control the laser shutters, the currents through our magnetic field coils and the frequency of our lasers. Furthermore we have also implemented direct digital synthesizer (DDS) boards from Analog Devices (AD9854). This way we have full control over amplitude, frequency and phase of the radiofrequency signal used to drive our AOMs.

For the communication between the hardware and the control computer we use a high speed 32-bit parallel digital I/O interface from National Instruments (NI-6533). The data is sent from the interface to the individual boards via a general purpose parallel bus. The clock frequency of 2 MHz enables to update the values at the outputs every 500 ns. We phase-lock our clock to the 50 Hz of the AC power line, in order to keep the electronic noise at a minimum.

The control software is a self-written LabView program (version 8.5), which runs on our so-called “control computer”. It features a user interface to enter the values for our experimental sequences and passes these values on to the NI-6533 board.

In addition a second computer is required to display and to store the pictures taken by our CCD-cameras. This so-called data “acquisition computer” not only files the camera picture, but also the corresponding values of the control outputs. These values are sent from the control computer to the data acquisition computer via TCP/IP.

# Chapter 4

# Trapping of Barium ions

Over the last view decades the Paul trap and the Penning trap have been used for a lot of beautiful experiments. Particularly, both traps have routinely been employed to store ions on a single particle level. In a Penning trap, however, the state of minimal ion energy is not stable. Therefore this kind of trap is not suited for the investigation of ultra-cold atom-ion collisions, for which the ion energy is desired to be as low as possible. Thus we confine the ions in a Paul trap with a combination of a static and an oscillating electric field. The two most common variations of the Paul trap are the ring trap and the linear trap. In our experiment we employ the latter one, since it gives us the opportunity to work with a linear string of several ions. For deeper insight and a general overview about ion trapping I would like to refer to a review article of Dave Wineland et. al. [36] and to the book of P. K. Gosh [37].

## 4.1 The Linear Paul trap

In a linear Paul trap the radial confinement (xy-plane) is achieved by applying a high-voltage radiofrequency to two of the four blade electrodes, just like in the case of a quadrupole mass filter. Trapping along the axial ($z$) direction is ensured by applying positive DC voltages to the endcap electrodes. The total trapping potential can be written as

$$\Phi = \Phi_{\mathsf{blade}} + \Phi_{\mathsf{end}}, \tag{4.1}$$

where $\Phi_{\mathsf{blade}}$ and $\Phi_{\mathsf{end}}$ are the potentials formed by the blade electrodes and the end-cap electrodes, respectively. When a voltage $U_{\mathsf{RF}} \cos(\Omega t)$ is applied to

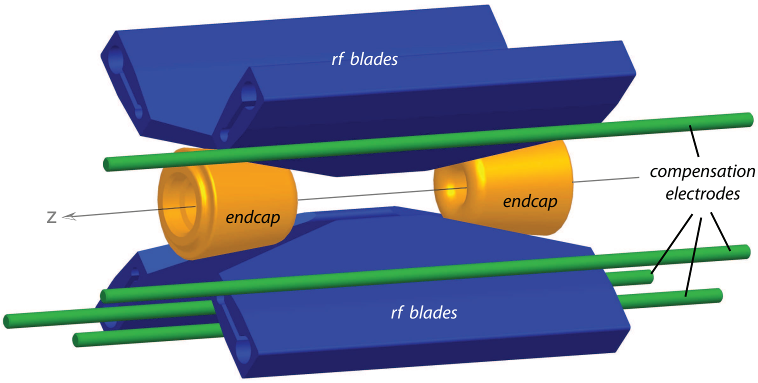

Figure 4.1: *Linear Paul trap:* Four rf blades (blue) are used to confine the ions along the radial direction (xy-plane). Two endcap electrodes (golden) are needed for trapping along the third ($z$) direction. The ions are moved within the xy-plane by applying appropriate voltages to the compensation electrodes (green).

two opposite blade electrodes, a potential of the form

$$\Phi_{\mathsf{blade}}(x,y) = \frac{U_{\mathrm{RF}}}{2}\left(1+\frac{x^2-y^2}{\tilde{r}_0^2}\right)\cos(\Omega t) \tag{4.2}$$

is generated close to the center (i.e. $x, y \ll \tilde{r}_0$). In the case of hyperbolically shaped electrodes the parameter $\tilde{r}_0$ is equal to the minimum distance of the electrodes to the trap center $r_0$. In general for non-hyperbolically shaped electrodes $\tilde{r}_0 = \nu r_0$, where $\nu$ is a dimensionless parameter which depends on the geometry of the electrodes. A DC voltage $U_{\mathsf{end}}$ applied to the end-caps leads to the potential

$$\Phi_{\mathsf{end}}(x,y,z) = \frac{\kappa U_{\mathsf{end}}}{z_0^2}\left(z^2-\frac{x^2}{2}-\frac{y^2}{2}\right), \tag{4.3}$$

where $L = 2z_0$ is the distance between the endcaps and $\kappa$ is again a dimensionless number which depends on the details of the trap geometry. The total potential then reads

$$\begin{aligned}\Phi(x,y,z) = \frac{U_{\mathsf{RF}}}{2}\cos(\Omega t) &+ \left(\frac{U_{\mathsf{RF}}}{2\tilde{r}_0^2}\cos(\Omega t) - \frac{\kappa U_{\mathsf{end}}}{2z_0^2}\right)x^2 \\ &- \left(\frac{U_{\mathsf{RF}}}{2\tilde{r}_0^2}\cos(\Omega t) + \frac{\kappa U_{\mathsf{end}}}{2z_0^2}\right)y^2 \\ &+ \frac{\kappa U_{\mathsf{end}}}{z_0^2}z^2. \end{aligned} \tag{4.4}$$

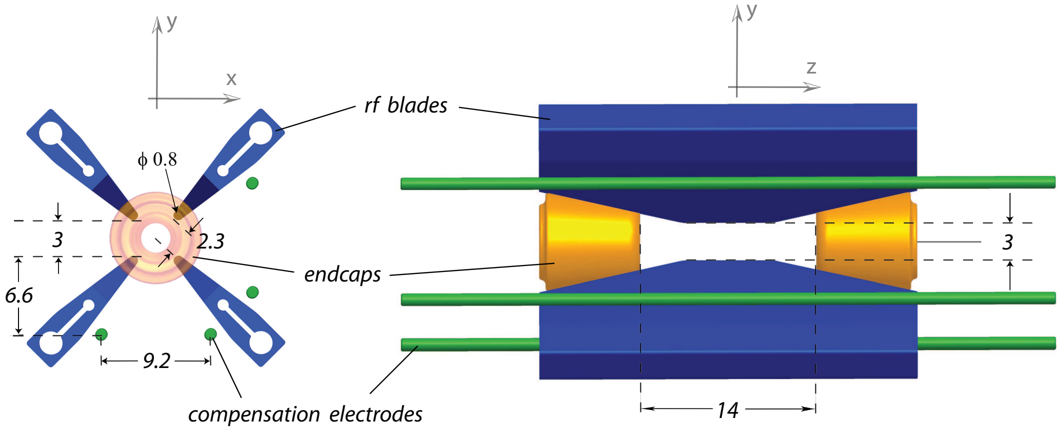

Figure 4.2: *Front and side view of the trap:* All dimensions are given in mm. The edge of the blade electrodes has a radius of curvature of 0.4 mm and the electrode is mounted such that the clear view diameter is *cvd* = 3 mm. The endcaps have a bore with a diameter of 2.5 mm and are separated by a distance of $L = 2z_0 = 14\,\mathrm{mm}$. The compensation electrodes are placed 9.3 mm away from the trap center.

From this we can derive the electric field

$$\begin{aligned}\mathbf{E}(x,y,z) = &\left(\frac{U_{\mathsf{RF}}}{\tilde{r}_0^2}\cos(\Omega t) - \frac{\kappa U_{\mathsf{end}}}{z_0^2}\right) x\,\hat{\mathbf{e}}_\mathbf{x} \\ &- \left(\frac{U_{\mathsf{RF}}}{\tilde{r}_0^2}\cos(\Omega t) + \frac{\kappa U_{\mathsf{end}}}{z_0^2}\right) y\,\hat{\mathbf{e}}_\mathbf{y} \\ &+ \frac{2\kappa U_{\mathsf{end}}}{z_0^2} z\,\hat{\mathbf{e}}_\mathbf{z}.\end{aligned} \tag{4.5}$$

In this field the equation of motion $m\ddot{\mathbf{x}} = -e\mathbf{E}$ for a singly charged ion with mass $m$ and charge $e$ is given by

$$\begin{aligned}\ddot{x} + [2q\cos(\Omega t) - b]\,\frac{\Omega^2}{4}x &= 0 \\ \ddot{y} - [2q\cos(\Omega t) + b]\,\frac{\Omega^2}{4}y &= 0 \\ \ddot{z} + \frac{\Omega^2}{2}b\,z &= 0\end{aligned} \tag{4.6}$$

with

$$
q = \frac{2eU_{\mathsf{RF}}}{m\tilde{r}_0^2\Omega^2} \tag{4.7}
$$

$$
b = \frac{4e\kappa U_{\mathsf{end}}}{mz_0^2\Omega^2}. \tag{4.8}
$$

These equations of motion (4.6) are known as the Mathieu equations. To solve them we separate the motion of the ion into a fast ***micromotion*** at frequency $\Omega$ and into a slow ***secular motion*** [37–39].

For $b \ll 1$ and $q \ll 1$ the solutions of (4.6) can be written as [39, 40]

$$
\begin{aligned}
x(t) &\approx A_x \cos(\omega_x t + \phi_x)\left(1 + \frac{q}{2}\cos(\Omega t)\right) \\
y(t) &\approx A_y \cos(\omega_y t + \phi_y)\left(1 + \frac{q}{2}\cos(\Omega t)\right) \\
z(t) &\approx A_z \cos(\omega_z t + \phi_y)
\end{aligned} \tag{4.9}
$$

where the secular frequencies are given by

$$
\omega_{\mathsf{rad}} \equiv \omega_x = \omega_y = \frac{\Omega}{2}\sqrt{\frac{q^2}{2} - b} \tag{4.10}
$$

$$
\omega_z = \frac{\Omega}{2}\sqrt{2b}. \tag{4.11}
$$

On time scales much larger than $1/\Omega$ the trapping potential of the rf Paul trap is quasi-static. Close to the center of the trap this quasi-static potential has a harmonic shape, with trap frequencies given by (4.10) and (4.11).

## 4.2 Operating the trap

### 4.2.1 Loading of ions

A commercially available oven (Alvasource from the company Alvatec) is used as a source of neutral Barium. The oven is a stainless steel tube with a diameter of 2 mm and a length of about 30 mm. The tube, which is welded up at both ends, is filled with He as an inert gas and with a stable intermetallic compound of barium and another non-toxic metal such as indium, gallium, tin or bismuth. Once the chamber is evacuated, the oven can be put into operation. In a first step a current of about 9 A is sent through the oven in order to melt the very

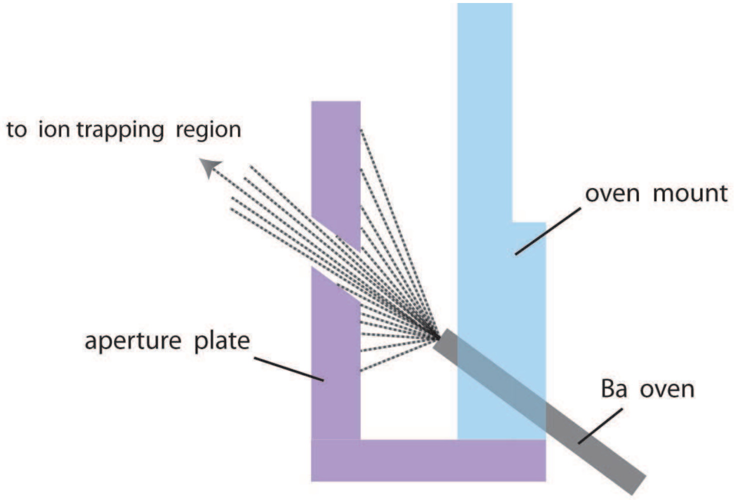

Figure 4.3: *Collimation of the atomic beam:* By heating up the oven, Ba atoms start to exit at the front end of the oven. The majority of these atoms are moving along the direction of the oven. However, some particles (in particular those, which are evaporated off close to the front end) will have a random direction. These atoms would not be able to reach the center of the Paul trap, but rather they would hit one of the rf blades of our trap. Therefore, in order to avoid that our blades get gradually coated with Ba, we put an aperture plate into our atomic beam. This way, we are able to sort out the particles, that are indeed moving towards the trap center.

thin Indium weld at the front side of the tube. As soon as the oven is "open", the He is pumped away and pure atomic Ba is released from the intermetallic compound. By following this procedure the Ba does not get into contact with air and thus the formation of BaN or BaO on the surface of the Ba is avoided.

The oven tube is mounted such that it points directly to the center of the ion trap (see Fig.4.5) and the position is fixed using a ceramics (Macor) part. In order to evaporate off neutral Barium, we typically run a current of about 7.5 A (corresponding to about 6 W) through the oven. An additional aperture plate (also made of Macor) is used to collimate the atomic beam and thus to avoid that the electrodes get coated with Barium (see Fig. 4.3). Once the Ba atoms reach the center of the trap, they are photoionized by driving a resonant two-photon transition from the ground state to the continuum via the $^3D_1$ state [41]. For this purpose a few mW of laser power at a wavelength of 413 nm are used (see Fig. 4.4). With this ionization procedure typical loading times (single ion) are on the order of one minute.

Once the ions have been trapped, they are laser-cooled for tens of seconds

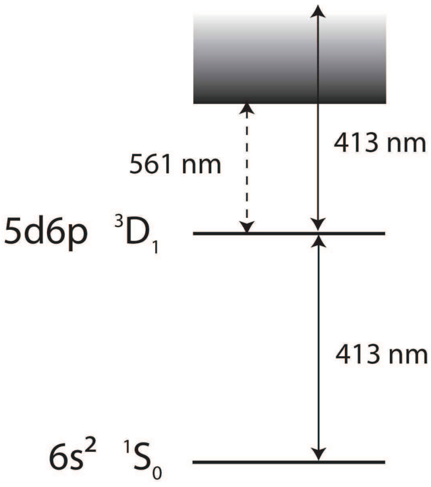

Figure 4.4: Relevant transitions for the photo-ionization of neutral Ba: At first, the 413 nm laser excites the atom into the 5d6p $^3D_1$ state and then drives the transition far into the continuum.

to reach mK temperatures. For this purpose we overlap the cooling(493 nm), the repumping(650 nm) and the ionization (413 nm) laser beam with very high precision using a laser beam profiler. Eventually the ions can be detected via fluorescence imaging.

### 4.2.2 Cooling of ions

In order to properly describe the laser cooling of trapped atoms and ions it is necessary to determine the value for the so-called Lamb-Dicke parameter $\eta$. This parameter compares the mean extension of the particle's wavepackage $\sqrt{\langle \Delta \hat{X}^2 \rangle}$ with the wavelength of the cooling light. For a particle trapped in a harmonic potential and being in number state $|n\rangle$, $\eta$ is defined as

$$\eta = k\sqrt{\langle \Delta \hat{X}^2 \rangle} = k\sqrt{2n+1}\sqrt{\frac{\hbar}{2m\omega}} \tag{4.12}$$

where $k = 2\pi/\lambda$ is the wavevector of the cooling laser, $m$ the mass of the particle, and $\omega$ the trap frequency. In our experiment $\eta$ is about 1, when the ion reaches the Doppler temperature. Above Doppler temperature $\eta$ is larger than one, meaning that we do not enter the Lamb-Dicke regime during Doppler cooling. Therefore, we can describe the laser cooling in our case as if the ion was a free particle [42].

The Doppler-cooling is performed on the $6S_{1/2} \rightarrow 6P_{1/2}$ cycling transition

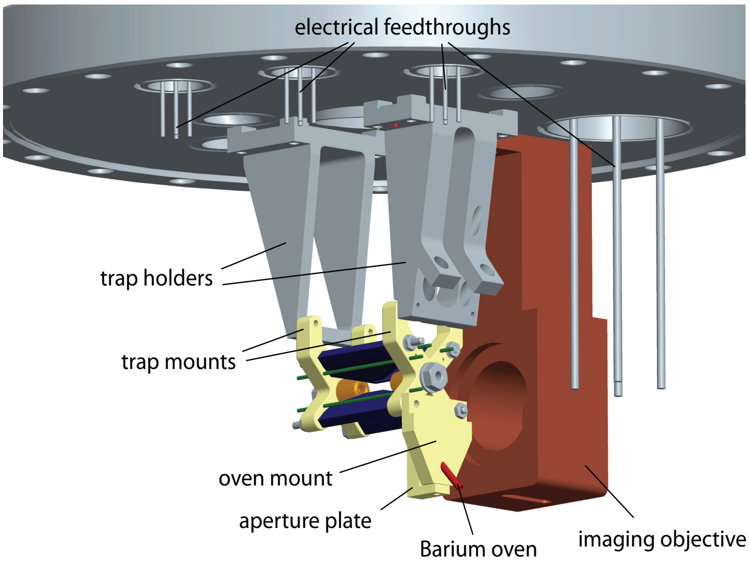

Figure 4.5: *Overview of the ion trapping region:* The Paul trap electrodes are mounted onto the center of the 200CF science flange using trap holders (stainless steel) and trap mounts (macor). Additional macor parts are required to mount the Ba oven and to aperture the Ba atom beam. The imaging objective for collecting the fluorescence of the $\mathrm{Ba}^+$ ions is also put onto the science flange at a distance of 6 cm from the center of the trap.

(see Fig. 3.9), which has a transition wavelength of 493 nm and a linewidth of $\Gamma_{\mathrm{cool}}/(2\pi) = 15.1\,\mathrm{MHz}$. The minimum temperature we can reach is $k_B T_D = \hbar\Gamma_{\mathrm{cool}}/2 \approx k_B \times 360\,\mu\mathrm{K}$. With a probability of about 25% the ion does not decay into the $6S_{1/2}$ groundstate, but into the metastable $5D_{3/2}$ state. For this reason a second cooling laser at a wavelength of 650 nm is needed. Since the contribution of the 650 nm light to the cooling is only about 25%, this second laser is often called repumping laser.

### 4.2.3 Detection of ions

We detect the ion by collecting its fluorescence using a “high-aperture laser objective (HALO)” from the company Linos. The HALO has a numerical aperture of $\mathrm{NA} = 0.2$ and a focal length of $f = 60\,\mathrm{mm}$, which enables to collect about $\mathrm{NA}^2/4 \approx 1\%$ of the spontaneously emitted photons. In order to be able to place the HALO at a distance of $f = 60\,\mathrm{mm}$ from the trap center, it has to be put into the vacuum chamber. The original mount, which holds all four lenses of the objective at a fixed position, is anodized and generally not designed to be put into a UHV environment. For this reason an exact copy of the original mount was made by our mechanical workshop (Fig. 4.5). Our home-built mount is made out of UHV-capable aluminum and features an air vent in order to avoid slow outgassing of air that is enclosed in between the different lenses of the objective (virtual leaks).

The collimated fluorescence light exits the chamber through a CF63 AR-coated viewport and a $f$ =300 mm achromat is then used to focus the light onto the CCD chip of an Andor Luca(S) camera. Together the HALO and the achromat form a telescope with a magnification of 5. Diffraction at the aperture of the HALO ultimately limits the resolution of the imaging system to about 1.5 µm, which is an order of magnitude smaller than the typical distance between two neighboring ions of an ion string. The Andor Luca(S) is a cost effective EM-CCD (electron-multiplying charge coupled device) camera designed for low light imaging. At 493 nm the quantum efficiency is about 50%. During operation the CCD chip of the camera is held at -20°C. Cooling the CCD-chip together with operating the camera in the electron-mulitplying (EM) mode reduces the noise level to less than 100 photons per second. Being able to measure such low light levels is particularly important when one wants to trap ions for the first time. In the beginning the fluorescence signal from the ions is typically very small, since the exact values for the experimental parameters (such as the oven current, laser powers, focus position) are not known. However, once an ion signal is detected, the parameters can be adjusted properly. For the optimal settings we expect the number of detectable photons to be

$$\Gamma_{\mathrm{detect}} = \frac{\Gamma_{\mathrm{cool}}}{2} \frac{d^2}{16 f^2} \eta_{\mathrm{CCD}} \tag{4.13}$$

where the diameter of the lens is $d = 25.4\,\mathrm{mm}$, the distance between the lens and the ion $f = 60\,\mathrm{mm}$, the transition linewidth $\Gamma_{\mathrm{cool}}/(2\pi) = 15.1\,\mathrm{MHz}$ and the quantum efficiency of the camera $\eta_{\mathrm{CCD}} \approx 80\%$. With these numbers we theoretically expect almost $10^5$ photons per second. In the experiment we are able to collect several $10^4$ photons per second per ion with our imaging system.

## 4.3 Oscillation frequencies

In this section I will discuss the normal mode frequencies of a single ion as well as of a two-ion crystal stored in our Paul trap. These eigenfrequencies are important parameters for characterizing the trapping of the ions.

### 4.3.1 Single ion - trap frequencies

The oscillation frequencies of a single ion (= trap frequencies) have already been calculated in the first section of this chapter (equations (4.10) and (4.11)). Using the expressions for $q$ (equation (4.7)) and for $b$ (equation (4.8)) we obtain the eigen-frequencies

$$\omega_{\mathsf{rad}} = \sqrt{\frac{e^2 U_{\mathsf{rf}}^2}{2m^2 \tilde{r}_0^4 \Omega^2} - \frac{e\kappa U_{\mathsf{end}}}{m z_0^2}} \tag{4.14}$$

$$\omega_z = \sqrt{\frac{2e\kappa}{m z_0^2} U_{\mathsf{end}}} \tag{4.15}$$

as a function of the rf amplitude $U_{\mathrm{rf}}$ and the end-cap voltage $U_{\mathsf{end}}$.

Experimentally the radial trap frequency is determined via amplitude modulation of the rf voltage. The modulation frequency is varied and when it is equal to the trap frequency the ion is resonantly heated. For a sufficiently large modulation amplitude the heating is strong enough to put the ion into an orbit of several $\mu$m, that can be detected via fluorescence imaging. For a single ion we actually find two radial trap frequencies on the order of 200 kHz, which differ by about 5%. We explain the existence of two radial eigenfrequencies by the fact, that due to geometrical imperfections the potential generated by the rf blades is not perfectly cylindrically symmetric. A simple estimation shows that an uncertainty of $\Delta\omega/\omega \approx 5\%$ corresponds to $\Delta\tilde{r}_0/\tilde{r}_0 = -2\Delta\omega/\omega \approx 2.5\%$ and thus to $\Delta\tilde{r}_0 \approx 60\,\mu\mathrm{m}$. In Fig. 4.6a the two radial eigenfrequencies are plotted versus the end-cap voltage. The frequencies decrease for increasing end-cap voltages, because the end-caps generate a (small) anti-trapping potential along the radial directions. By fitting the relation (4.14) to the data, we obtain values for the two geometric parameters $\kappa = 0.295$ and $\tilde{r}_0 = 2.6\,\mathrm{mm}$, which depend on the exact geometry of all ion trap electrodes. The "effective distance" $\tilde{r}_0$ is the distance to the center, that ideal quadrupole-shaped electrodes would have to have in order to generate the same trap frequencies as our blade electrodes. As expected, $\tilde{r}_0$ is slightly larger than the "real distance" to the trap center $r_0 = 2.3\,\mathrm{mm}$. By plugging the values for $\kappa$ and $\tilde{r}_0$ together with the typical voltages used in our experiment $U_{\mathsf{RF}} = 700\,\mathrm{V}$ and $U_{\mathsf{end}} = 40\,\mathrm{V}$ into the equations (4.7) and (4.8), we obtain $q \approx 0.13$ and $b \approx 6 \times 10^{-4}$.

To determine the axial trap frequency we modulate the end cap voltage and

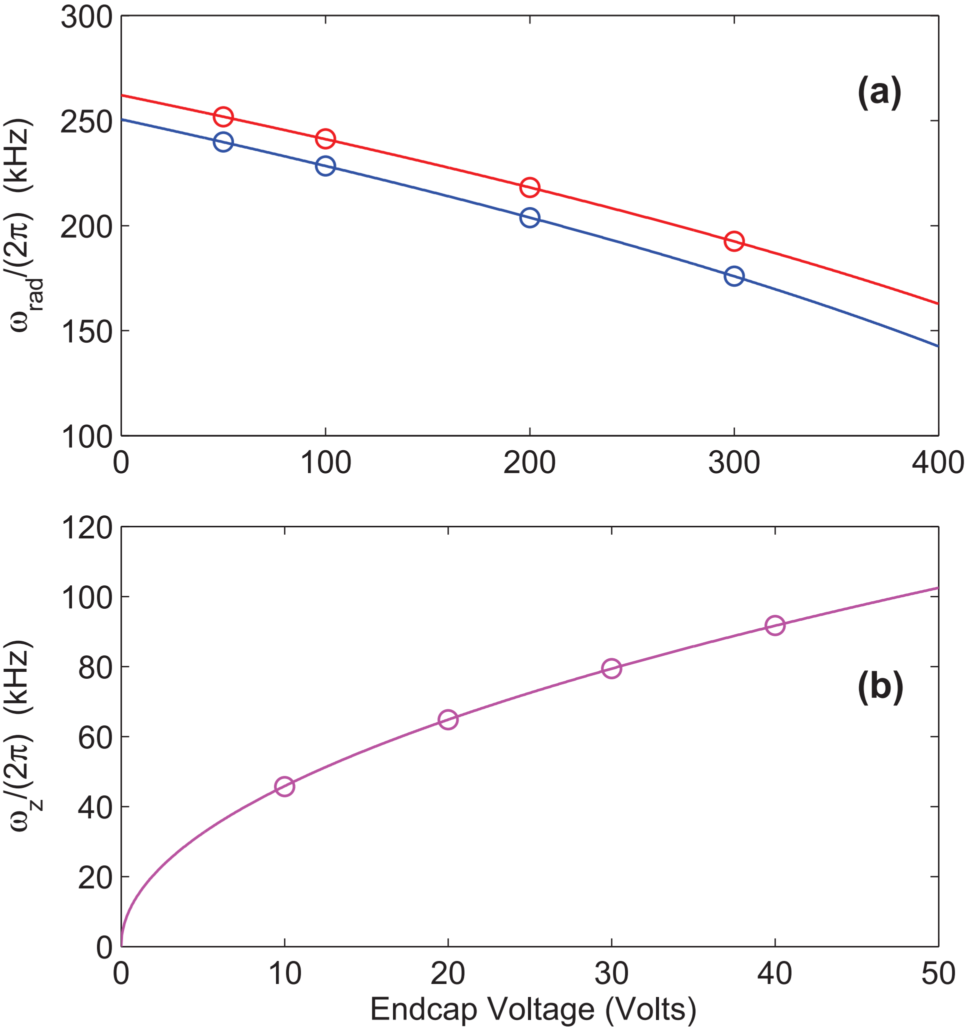

Figure 4.6: Measurement of the trap frequencies for a given rf amplitude $U_{\mathrm{rf}} = 700\,\mathrm{V}$, rf-drive frequency $\Omega = 2\pi \times 5.24\,\mathrm{MHz}$ and end-cap separation $2z_0 = 14\,\mathrm{mm}$. **(a)** By fitting the relation for the **radial trap frequencies** (4.14) to our data we find $\kappa = 0.295$ and $\tilde{r}_0 = 2.6\,\mathrm{mm}$. **(b)** Fitting the expression for the **axial trap frequency** (4.15) to the data leads to $\kappa = 0.293$.

again look for resonant heating of the ion. Typical axial trap frequencies in our experiment are between 50 kHz and 100 kHz. We also measure $\omega_\mathsf{z}$ for various DC voltages on the end-cap electrodes (see Fig. 4.6b) and fit the expression (4.15) to our data. By again using $\kappa$ as a free fit parameter we extract $\kappa = 0.293$. This value is in very good agreement with the one obtained from the measurement of the radial trap frequencies.

By measuring the trap frequencies $\omega_\mathsf{rad}$ and $\omega_\mathsf{z}$ for various endcap voltages $U_\mathsf{end}$, we have been able to determine the geometry parameters $\kappa$ and $\tilde{r}_0$. With these two quantities we can simulate our trapping potential, in order to find values for our trap depth.

### 4.3.2 Normal mode frequencies of a two-ion crystal

The potential energy $U$ of two singly-charged ions with masses $m_1$ and $m_2$, confined in a harmonic trap with radial trap frequencies $\omega_{r,1}$ and $\omega_{r,2}$ and axial trap frequencies $\omega_{z,1}$ and $\omega_{z,2}$ is given by

$$\begin{aligned} U = \frac{1}{2}m_1\left(\omega_{z,1}^2 z_1^2 + \omega_{r,1}^2 r_1^2\right) &+ \frac{1}{2}m_2\left(\omega_{z,2}^2 z_2^2 + \omega_{r,2}^2 r_2^2\right) \\ &+ \frac{e^2}{4\pi\epsilon_0}\frac{1}{\sqrt{(z_1 - z_2)^2 + (r_1 - r_2)^2}} \end{aligned} \tag{4.16}$$

where the last term arises from the Coulomb repulsion of the two ions. A linear Paul trap is usually operated such that $\omega_r \gg \omega_z$. In this case the radial equilibrium positions are $r_1^{(0)} = r_2^{(0)} \approx 0$. To find the axial equilibrium positions $z_1^{(0)}$ and $z_2^{(0)}$ we calculate $(\partial U/\partial z_1)_{(0)} = 0$ and $(\partial U/\partial z_2)_{(0)} = 0$, where the subscript "(0)" denotes that we have to plug in the radial equilibrium positions. At this point it is very helpful to note, that $m_1\omega_{z,1}^2 = m_2\omega_{z,2}^2$, since $\omega_z \propto 1/\sqrt{m}$. As a consequence the ions are displaced symmetrically from the trap center, even in the case of $m_1 \neq m_2$. We get

$$\begin{aligned} z_1^{(0)} &= \left(\frac{e^2}{4\pi\epsilon_0}\frac{1}{m_1\omega_{z,1}^2}\right)^{1/3} = \left(\frac{e^2}{4\pi\epsilon_0}\frac{1}{m_2\omega_{z,2}^2}\right)^{1/3} \\ z_2^{(0)} &= -\left(\frac{e^2}{4\pi\epsilon_0}\frac{1}{m_1\omega_{z,1}^2}\right)^{1/3} = -\left(\frac{e^2}{4\pi\epsilon_0}\frac{1}{m_2\omega_{z,2}^2}\right)^{1/3}. \end{aligned} \tag{4.17}$$

The motion of the two ions is coupled via the Coulomb interaction. Thus, the eigenfrequencies of the two-ion-system are not simply given by the trap frequencies. However, the eigenfrequencies can be calculated by solving the classical equations of motion for the potential given by (4.16) [43]. Assuming small oscillations the equations of motion have the form

$$T\ddot{r} + V_{\mathrm{rad}} r = 0 \tag{4.18}$$

$$T\ddot{z} + V_{\mathrm{ax}} z = 0 \tag{4.19}$$

with

$$r = \begin{pmatrix} r_1 \\ r_2 \end{pmatrix} \qquad z = \begin{pmatrix} z_1 \\ z_2 \end{pmatrix} \tag{4.20}$$

$$T_{ii} = m_i \qquad T_{ij} = 0 \quad \text{for} \quad i \neq j \tag{4.21}$$

$$V_{ij}^{\mathrm{rad}} = \frac{\partial^2 U}{\partial r_i \partial r_j} \tag{4.22}$$

$$V_{ij}^{\mathrm{ax}} = \frac{\partial^2 U}{\partial z_i \partial z_j}. \tag{4.23}$$

It is well known, that the solutions to the equations (4.18) and (4.19) are harmonic functions. The corresponding eigenfrequencies $\Omega_{\mathrm{rad}}$ and $\Omega_{\mathrm{ax}}$ are found by solving

$$\begin{aligned} \det(V_{\mathrm{rad}} - \Omega_{\mathrm{rad}}^2 T) &= 0 \\ \det(V_{\mathrm{ax}} - \Omega_{\mathrm{ax}}^2 T) &= 0 \end{aligned} \tag{4.24}$$

Using the potential given by equation (4.16), the equations (4.24) can easily be solved analytically. We obtain for the axial direction (see also [44])

$$\begin{aligned} \Omega_{\pm}^{\mathrm{ax}} &= \sqrt{\omega_{z,1}^2 + \omega_{z,2}^2 \pm \sqrt{\omega_{z,1}^4 + \omega_{z,2}^4 - \omega_{z,1}^2 \omega_{z,2}^2}} \\ &= \omega_{z,1} \sqrt{1 + \frac{m_1}{m_2} \pm \sqrt{1 - \frac{m_1}{m_2} + \frac{m_1^2}{m_2^2}}} \end{aligned} \tag{4.25}$$

where $m_1 \leq m_2$. For the special case of equal masses $m_1 = m_2$ (and thus also

Table 4.1: Axial eigenfrequencies of a two-ion crystal, when one of the two ions is $^{138}\mathrm{Ba}^+$ with a trap frequency of $\omega_{\mathrm{z},1}$.

| second ion | $\Omega_+^{\mathrm{axial}}/\omega_{\mathrm{z},1}$ | $\Omega_-^{\mathrm{axial}}/\omega_{\mathrm{z},1}$ |
|---|---|---|
| $^{138}\mathrm{Ba}^+$ | $\sqrt{3}$ | 1 |
| $^{87}\mathrm{Rb}^+$ | 1.99 | 1.09 |
| $(^{138}\mathrm{Ba}^{87}\mathrm{Rb})^+$ | 1.58 | 0.86 |
| $^{87}\mathrm{Rb}_2^+$ | 1.65 | 0.94 |

$\omega_{z,1} = \omega_{z,2} = \omega_z$) we get the well-known eigenfrequencies $\Omega_-^{\mathrm{ax}} = \omega_z$ (center-of-mass (COM) mode) and $\Omega_+^{\mathrm{ax}} = \sqrt{3}\omega_z$ (breathing mode).

For the transverse motion (radial direction) the eigenfrequencies are found to be

$$\Omega_\pm^{\mathrm{rad}} = \sqrt{\frac{\omega_{r,1}^2 + \omega_{r,2}^2}{2} - \frac{\omega_{z,1}^2 + \omega_{z,2}^2}{4} \pm \frac{1}{2}\sqrt{\left(\omega_{z,1}^2 - \omega_{z,2}^2 - \omega_{r,1}^2 + \omega_{r,2}^2\right)^2 + \omega_{z,1}^2\omega_{z,2}^2}} \tag{4.26}$$

Again looking at the special case of $m_1 = m_2$, meaning that $\omega_{z,1} = \omega_{z,2} = \omega_z$ and $\omega_{r,1} = \omega_{r,2} = \omega_r$, the eigenfrequencies take the simple form $\Omega_+^{\mathrm{rad}} = \omega_r$ (COM mode) and $\Omega_-^{\mathrm{rad}} = \sqrt{\omega_r^2 - \omega_z^2}$ (rocking mode).

Analogous to the case of a single ion, the eigenfrequencies $\Omega_\pm^{\mathrm{rad}}$ and $\Omega_\pm^{\mathrm{ax}}$ are experimentally found via modulation of the rf amplitude and the endcap voltage, respectively. For our purposes the most important situation is when one of the ions is a (bright) $\mathrm{Ba}^+$ ion and the second one a dark unknown ion. We then watch the fluorescence of the $\mathrm{Ba}^+$ ion to find the eigenfrequencies and use the values for $\Omega_\pm^{\mathrm{radial}}$ and $\Omega_\pm^{\mathrm{axial}}$ together with the expressions (4.25) and (4.26) to figure out the mass of the unknown ion (see also table 4.1). We use this technique to identify the dark ions formed in an inelastic atom-ion collision.

## 4.4 Trap depth

The trap depth is the energy required to remove the ion from the trap. For given trap frequencies the trap depth increases with the size of the trap. With the rf blade electrodes placed at a distance of $r_0 = 2.3\,\mathrm{mm}$ from the trap center, the size of our Paul trap and thus also its trap depth is large, as compared with most of the other Paul traps for cold ions which are in use worldwide. Due to the large

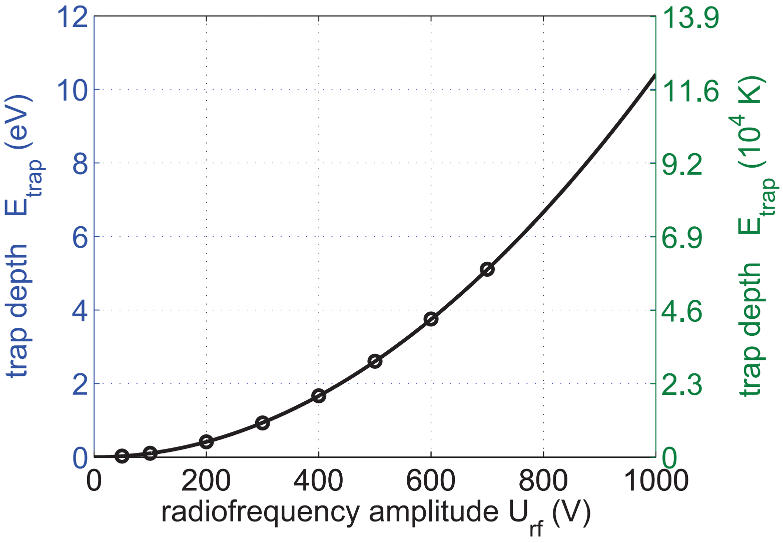

Figure 4.7: Trap depth (on left axis in eV and on right axis in K) as a function of the rf amplitude $U_{\mathsf{rf}}$. The circles are the results from the numerical simulation. The solid line is a harmonic fit $E_{\text{trap}} = \epsilon U_{\mathsf{rf}}^2$, from which we obtain $\epsilon = 1.041 \times 10^{-5}\,\text{eV}/\text{V}^2$.

trap depth we are able to store ions even without laser cooling for basically any amount of time.

The trap depth can be derived numerically by solving the Laplace equation using finite element methods. Such a calculation also provides values for the trap frequencies, which we have cross-checked with the measured values. This way we were able to verify the simulation. In Fig. 4.7 the calculated trap depth is plotted versus rf amplitude $U_{\mathsf{rf}}$. Typical values are on the order of a few eV, corresponding to several $k_{\mathsf{B}} \times 10^4\,\text{K}$.

## 4.5 Micromotion

As derived previously the motion of an ion in a rf Paul trap is a combination of a slow secular motion and a fast micromotion (see equation (4.9)). The amount of micromotion is determined by the amplitude of secular motion and thus by the temperature of the ion. The only way to reduce the micromotion for a given set of parameters is to cool the ion.

Besides the “ordinary micromotion” discussed so far, the ion also exhibits so-called “excess micromotion”. For the collision energies in the experiments described here, the main cause for "excess micromotion" are unwanted dc electric fields along the radial direction, which push the ion out of the rf node into a region of enhanced rf. Excess micromotion can also arise from a phase difference between the ac voltages applied to the rf electrodes. I will discuss this effect at the end of this section.

### 4.5.1 Ion kinematics in the presence of an electric field

Ideally the electric field in the center of a linear Paul trap is equal to zero. In the experiment, however, dc electric fields are present at the position of the ion. We classify these fields using their origin and thus distinguish between "charge fields" and "geometrical" fields. The latter ones are typically caused by imperfections in the fabrication and the alignment of the trap electrodes. The source for so-called charge fields are surface charges on the trap mountings and on the trap electrodes themselves. These charges are particularly a problem in experiments where an electron emitter is used for ionization.

In the following we derive the effect of a dc electric field $\mathbf{E}_{\mathrm{dc}}$ on the motion of the trapped ion. The equations of motion take the form

$$\begin{aligned} \ddot{x} + [2q\cos(\Omega t) - b]\,\frac{\Omega^2}{4}x &= \frac{eE_{\mathrm{dc,x}}}{m} \\ \ddot{y} - [2q\cos(\Omega t) + b]\,\frac{\Omega^2}{4}y &= \frac{eE_{\mathrm{dc,y}}}{m} \\ \ddot{z} + \frac{\Omega^2}{2}b\,z &= \frac{eE_{\mathrm{dc,z}}}{m}. \end{aligned} \tag{4.27}$$

They can be solved in the same way as the equations for zero electrical field. The solution has the form

$$\begin{aligned} x(t) &\approx (A_x\cos(\omega_x t + \phi_x) + B_x)\left(1 + \frac{q}{2}\cos(\Omega t)\right) \\ y(t) &\approx (A_y\cos(\omega_y t + \phi_y) + B_y)\left(1 + \frac{q}{2}\cos(\Omega t)\right) \\ z(t) &\approx (A_z\cos(\omega_z t + \phi_y) + B_z)\,, \end{aligned} \tag{4.28}$$

where $A_i$ is the amplitude of the secular motion and

$$B_i = \frac{eE_{\mathrm{dc,i}}}{m\omega_i^2} \tag{4.29}$$

the position shift of the ion, when a field is applied. As can be seen from this solution, the motion in the radial plane has two "micromotion terms", both oscillating with frequency $\Omega$. The first part is the "ordinary micromotion" with amplitude $qA_i/2$, $i = \{x, y\}$, which can only be reduced by cooling of the ion. Our new term is the second one, which has an amplitude of $qB_i/2$ and thus is proportional to the dc electric field at the position of the ion $E_{\mathrm{dc,i}}$. Since $E_{\mathrm{dc,i}}$ can in principle be made arbitrarily small by proper compensation of electrical stray fields, the second term is called "excess micromotion".

The kinetic energy of the ion

$$E_{\mathrm{kin}} = \frac{1}{2} m \left( \langle \dot{x}^2 \rangle + \langle \dot{y}^2 \rangle + \langle \dot{z}^2 \rangle \right) \tag{4.30}$$

is calculated by averaging over one period of the secular motion. Plugging in the expressions for the trajectory (equation (4.28)), we get

$$\begin{aligned}
E_{\mathrm{kin}} &= E_{\mathrm{kin}}^{\mathrm{secular}} + E_{\mathrm{kin}}^{\mathrm{micro}} + E_{\mathrm{kin}}^{\mathrm{excess\ micro}} \\
E_{\mathrm{kin}}^{\mathrm{secular}} &= \frac{1}{2} m \left( A_x^2 \omega_x^2 + A_y^2 \omega_y^2 + A_z^2 \omega_z^2 \right) \\
E_{\mathrm{kin}}^{\mathrm{micro}} &= \frac{1}{16} m \Omega^2 q^2 \left( A_x^2 + A_y^2 \right) \\
E_{\mathrm{kin}}^{\mathrm{excess\ micro}} &= \frac{1}{m} \left( \frac{2eq}{(q^2 - 2b)\Omega} \right)^2 \left( E_{\mathrm{dc,x}}^2 + E_{\mathrm{dc,y}}^2 \right)
\end{aligned} \tag{4.31}$$

### 4.5.2 Compensation electrodes

The atom-ion collision energy is fully determined by the kinetic energy of the ion. Therefore it can be controlled via the ion's excess micromotion by applying an additional dc electric field along the radial direction. To generate these external electric fields four "compensation electrodes" are added to the design of our Paul trap (see Fig. 4.1 and 4.2).

Applying a voltage $U_{\mathrm{comp,x}}$ to the two horizontal and $U_{\mathrm{comp,y}}$ to the two vertical compensation electrodes leads to a position shift $\Delta x$ and $\Delta y$, respectively. The shift along the vertical direction $\Delta y$ can be determined using the fluorescence images of the ion. When measuring $\Delta y$ as a function of the compensation voltage, we find $\Delta y \propto U_{\mathrm{comp,y}}$, as expected, with a proportionality constant of 2.1(2) µm/V (Fig. 4.8). Using the expression (4.29) we can then derive the external electric field as a function of the compensation voltage

$$E_{\mathrm{ext,y}} \approx 4.9 \, \frac{\mathrm{V/m}}{\mathrm{V}} \cdot U_{\mathsf{comp,y}}. \tag{4.32}$$

We do not have the ability to measure the x-position of the ion with high resolution. Due to symmetry, however, we can assume the gauging factor to be approximately the same as for the y-direction.

### 4.5.3 Minimization of excess micromotion

For the majority of the experiments we want the ion energy and thus the excess micromotion to be as small as possible. Therefore we compensate for stray fields by adjusting the external field $\mathbf{E}_{\mathrm{ext}}$ such that the total dc electric field $\mathbf{E}_{\mathrm{dc}} = \mathbf{E}_{\mathrm{ext}} + \mathbf{E}_{\mathrm{stray}}$ vanishes. The following two methods are used in our experiment to null the dc electric field.

**Compensation via ion position:**

In the presence of an electric field the ion position changes when the steepness of the ion trap (the trap frequency) is varied. For this reason, we adjust the compensation voltages so that the position shifts of the ion due to changes of the rf amplitude is minimal. This compensation method is simple and reliable. For the experiments described in this thesis the DC electric field at the position of the ion was reduced to below 4 V/m, corresponding to a maximum ion energy of $k_B \times 40\,\mathrm{mK}$. As mentioned above, it is not possible with our current setup to measure the x-position of the ion with high resolution. Thus we can only compensate the stray fields along the y-direction with this "position method".

**Compensation via heating of the ion:**

For the compensation of the stray fields along the $x$-direction we apply the following method. The trapped ion is resonantly heated, when we modulate the amplitude of the rf voltage with the modulation frequency being equal to the trap frequency. This heating leads to a smear-out of the ion's fluorescence, that can be detected by taking fluorescence images (see also section 4.3). The amount of heating is increased, when the ion is not in the rf node, i.e. in the presence of a dc electric field. Therefore, we are able to compensate excess micromotion by minimizing the heating for given modulation parameters. We estimate that for the experiments presented in this work the residual electric field along the $x$-direction was also about 4 V/m.

Over the last couple of months a great effort was made to further reduce the dc

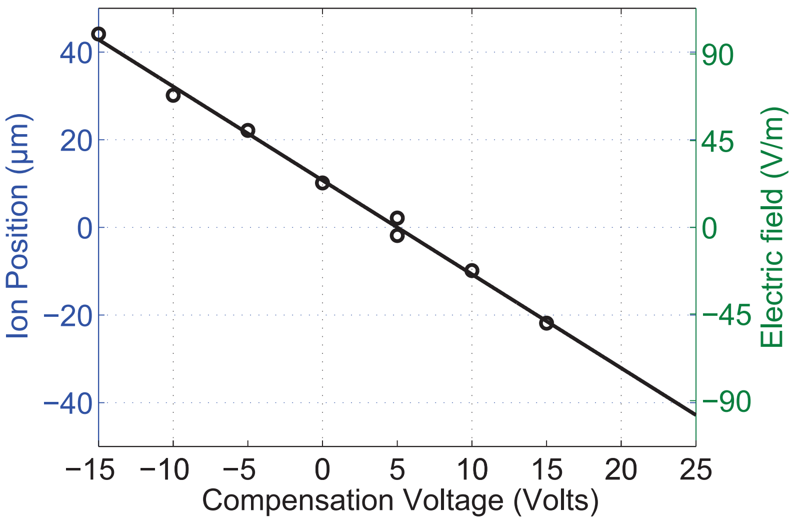

Figure 4.8: The vertical ion position is measured as a function of the voltage on the compensation electrode (*left y-axis*). Plugging the value for the trap frequency $\omega_{\mathrm{rad}} = 200\,\mathrm{kHz}$ into (4.29), we can also plot the electric field along the $y$-direction $E_y$ as a function of the compensation voltage (*right y-axis*).

electric fields, so that the residual fields are now (summer 2011) about $50\,\mathrm{mV/m}$ for the $y$-direction ("position method") and $150\,\mathrm{mV/m}$ for the $x$-direction ("heating method"). These values prove the high accuracy of the both compensation methods.

### 4.5.4 Further sources of excess micromotion

Additional micromotion can not only be caused by a dc electric field but also by a phase difference between the ac voltages applied to the rf electrodes. The existence of such a phase difference $\varphi_{\mathrm{ac}}$ will lead to an electric field pointing towards one of the two rf-driven blade electrodes. Consequently, the kinetic energy of the ion will be increased by an amount of [39]

$$E_{\mathrm{kin}}^{\mathrm{phase}} = \tfrac{1}{64} m \left(q\, r_0\, \alpha\, \varphi_{\mathrm{ac}}\, \Omega\right)^2 , \tag{4.33}$$

where $\alpha$ is a dimensionless parameter on the order of 1. A phase difference $\varphi_{\mathrm{ac}}$ can occur for instance when the rf electrodes are not wired up properly or the supply cables do not have equal length. This effect can be roughly estimated as follows. Assuming a speed of propagation of $c = 3 \times 10^8\,\mathrm{m/s}$, the radiofrequency of $\nu = 5\,\mathrm{MHz}$ has a wavelength of $\lambda = c/\nu = 60\,\mathrm{m}$. For a length difference of

$\delta l = 1\,\mathrm{mm}$ we would get a phase difference of $\varphi_{\mathrm{ac}}/(2\pi) = \delta l/\lambda \sim 10^{-5}$. Using equation (4.33) the excess kinetic energy of the ion due to such a phase difference is then estimated to be on the order of $E_{\mathrm{kin}}^{\mathrm{phase}} \sim k_{\mathrm{B}} \times 100\,\mu\mathrm{K}$. This value is much smaller than the typical excess micromotion energies due to dc electric stray fields. A more precise calculation of the phase difference effect is quite involved, since one would have to know the characteristic impedance and thus the exact geometry of the supply cables.

# Chapter 5

# Bose-Einstein condensates of Rubidium

## 5.1 Generation of the ultracold atom cloud

The techniques used in our experiment to create ultracold quantum gases of Rubidium atoms are very similar to those described in [45]. The atoms are collected in a magneto-optical trap (MOT) and then further cooled by the use of optical molasses. Subsequently the atom cloud is transported magnetically from the MOT chamber into the BEC chamber, where it is loaded into a QUadrupole-Ioffe-Configuration (QUIC) trap. Since the magnetic field is non-zero at the minimum of the QUIC trapping potential, the atom cloud can be cooled down to quantum degeneracy. In table 5.1 I have listed the particle number and the atom temperature after each step of the preparation process. In the following I will summarize in a nutshell our roadway to BEC and describe a few selected experimental characteristics in more detail.

### 5.1.1 Magneto-optical trap

The preparation of the neutral atom cloud starts with loading the Rb atoms from the background vapor into a standard six-beam MOT [46–48]. The MOT is operated at the $|\,F=2\rangle \rightarrow |\,F'=3\rangle$ cycling transition of $^{87}$Rb. To maximize the particle number we have chosen a detuning of -3.5$\Gamma$, where $\Gamma = 2\pi\times 6\,\mathrm{MHz}$ is the natural linewidth of the transition.

The atoms are not slowed down prior to capturing them in the MOT. Instead they are directly loaded from the surrounding Rb vapor, which is in equilibrium

Table 5.1: Roadway to a degenerate Rb quantum gas: Approximate values for the particle number as well as for the temperature of the atom cloud are listed.

| stage | MOT | Molasses cooling | Magnetic trap | after transport | after evaporation |
|---|---|---|---|---|---|
| Particle number | $3 \times 10^9$ | $2 \times 10^9$ | $1 \times 10^9$ | $5 \times 10^8$ | $2 \times 10^6$ |
| Temperature [µK] | 120 | 40 | 150 | 230 | 1 |

with the chamber walls and thus has room temperature. For maximum particle number we therefore require the MOT cooling beams to be as large as possible. Since we employ a tapered amplifier (see section Laser systems) the totally available MOT beam power is about 250 mW, which allows for having MOT beams with a diameter of 30 mm (the saturation intensity of the transition is $\sim 1.6\,\mathrm{mW/cm^2}$).

The MOT light can also excite the atoms into the $|\,F' = 2\rangle$ state with a small but non-vanishing probability, from which they can then decay into the $|\,F = 1\rangle$ groundstate. For this reason we need a "repumper laser", which is tuned resonantly to the $|\,F = 1\rangle \rightarrow |\,F' = 2\rangle$ transition. To pump the atoms back into the cycling transition, we use a total repumper power of about 10 mW.

To ensure the trapping of atoms in our MOT we add a pair of anti-Helmholtz coils to our setup. The MOT coils are placed at a distance of 25 mm above and below the MOT chamber. Both coils have an inner diameter of 70 mm, an outer diameter of 107 mm and consist of two layers with 2 x 15 windings in total. To operate the MOT we typically run a current of 5 A through the coils, leading to a magnetic field gradient of about 8 G/cm.

With the parameters given here we are able to load about $3{\times}10^9$ $^{87}$Rb atoms within a time of typically 8 s into our MOT, as detected via absorption imaging. Using time-of-flight (TOF) images, we find the temperature of the atom cloud to be slightly below the Doppler temperature of 140 µK.

### 5.1.2 Molasses cooling, spinpolarizing and magnetic trapping

Immediately after we have completed the loading of the MOT, we turn off the magnetic field and linearly change the detuning of the MOT cooling beams within 3 ms to about -8.5 $\Gamma$. The power of the beams is kept at the same value as for the MOT. The MOT beams now form a so-called optical molasses [47, 48]. For a total duration of 10 ms the atoms are not trapped. However, the temperature of

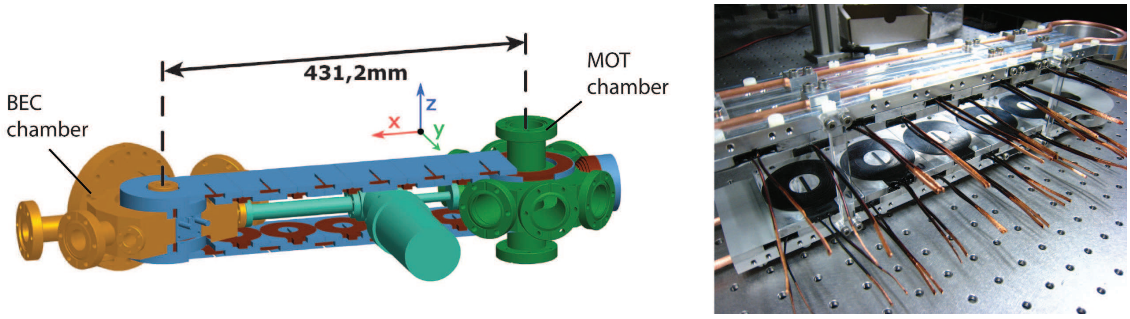

Figure 5.1: *Left:* Magnetic transport line: The neutral atom cloud is transported over a distance of 431.2 mm from the MOT chamber (green) to the BEC chamber (golden). All required magnetic field coils (brown) as well as their respective housings (blue) are shown. *Right:* Photo of the magnetic transport coils and the MOT coils (far right) before they are mounted to the vacuum apparatus.

the cloud is reduced further to about 40 µK.

In a next step the atoms are optically pumped into the lowest lying magnetically trappable state $|\, F = 1,\ m_F = -1\rangle$. For this spin-polarizing procedure we require a magnetic offset field, which we generate with our push coil. We then pump the atoms towards the $m_\mathrm{F} = -1$ substate by shining in $\sigma^-$ light propagating along the magnetic field axis and tuned to the $|\, F = 1\rangle \to |\, F' = 1\rangle$ transition. Since the atoms are originally (during MOT and molasses cooling) in the $|\, F = 2\rangle$ state, we shine in another $\sigma^-$ beam tuned to the $|\, F = 2\rangle \to |\, F' = 2\rangle$ transition. This beam excites the atoms to the $|\, F' = 2\rangle$ state from where they can then decay into the $|\, F = 1\rangle$ ground state.

Subsequently the spin-polarized atoms are loaded into a magnetic quadrupole trap. For this purpose we run a current of 80 A through our MOT coils to generate a magnetic field gradient of $B_z' = 130\,\mathrm{G/cm}$. This field gradient exerts a confining force of $4m_\mathrm{Rb}g$ on the atoms, which is clearly sufficient to hold them against gravity. Loading the atom cloud into the magnetic trap increases its temperature to about 150 µK. The total number of atoms at this stage is about $1 \times 10^9$.

### 5.1.3 Magnetic transport

Following the concept described in [49], we transport the cold atom cloud magnetically from the MOT chamber to the BEC chamber. For this transport we employ all together 13 anti-Helmholtz pairs of coils (11 transport coil pairs, the

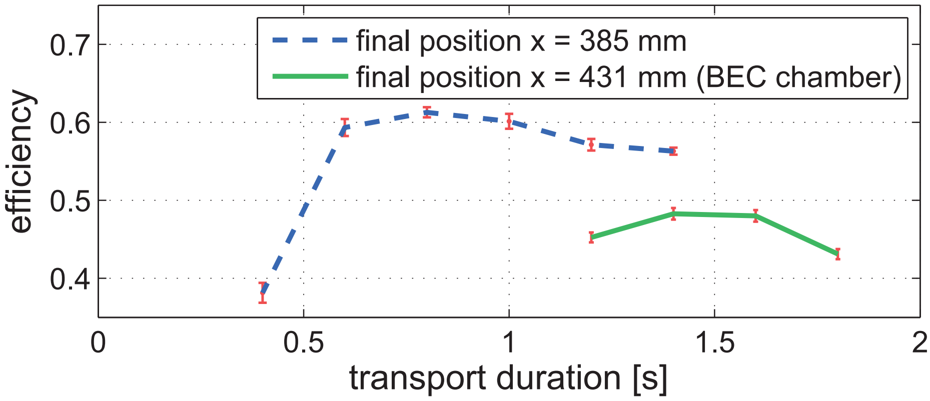

Figure 5.2: Efficiency as a function of the duration for the transport to the intermediate point $x = 385\,\mathrm{mm}$ and for the transport to the final position in the BEC chamber $x = 431.2\,\mathrm{mm}$. The rise of the cloud's aspect ratio, when it enters the BEC chamber, leads to the significant drop of the maximal efficiency ($\eta^{\mathrm{max}}_{385\mathrm{mm}} = 62\%$ and $\eta^{\mathrm{max}}_{431\mathrm{mm}} = 48\%$).

MOT coil pair, the QUIC quadrupole coil pair) and an additional "push coil". Each magnetic transport coil has an inner diameter of 47 mm and an outer diameter of 130 mm, with 2x17 windings in total. The transport coils are arranged in two (semi-overlapping) layers above and below the atoms. In order to keep the required current minimal, the distance between the coils and the atoms is chosen to be as small as possible. The distance, which is mainly limited by the size of the gate valve, is 50 mm for the inner layer and 57 mm for the outer layer, respectively.

The atoms can be moved from the center of one pair of quadrupole coils to the next by reducing the current through the first coil pair while ramping up the current through the second pair. However, since such a simple scheme would lead to a periodic change of the cloud's aspect ratio and thus to a heating of the atoms, we operate three neighboring coil pairs simultaneously. This way we can keep the aspect ratio at a constant value of 1.69.

We encounter a special situation at the beginning of the transport line, where the aspect ratio would blow up, since the size of the MOT coils makes it impossible to mount the first transport coils as close as required. This problem, though, has been fixed by adding a so-called "Push-coil" to the setup. The Push coil generates a force which points along the direction of the transport and it ensures that the aspect ratio is ramped smoothly from 1 (magnetic trap) to 1.69 (transport).

In an analogous way a so-called “Pull coil” would have been necessary at the end of the transport line. However, due to the geometry of the BEC chamber it was not possible to implement such a Pull coil. As a consequence the aspect ratio can only be kept at 1.69 until a transport position of $x = 385\,\mathrm{mm}$. When the cloud enters the BEC chamber the aspect ratio rises temporarily to 4.71, which leads to a larger duration and a smaller efficiency of the transport (see Fig. 5.2).

Together with the aspect ratio we also keep the magnetic field gradient along the vertical direction ($\partial B/\partial z = 130\,\mathrm{G/cm}$) constant throughout the transport. These input parameters uniquely define the curves for the currents through the coils $I$ as a function of the atom cloud position $x$. For the kinematics of the atom cloud $x(t)$ we have chosen a smooth spline interpolation between the starting point $x = 0$ and the intermediate point $x = 385\,\mathrm{mm}$, as well as between the intermediate point and the final position $x = 431.2\,\mathrm{mm}$. The only parameter, that remains variable, is the transport duration, which is chosen such that the transport efficiency is maximal (Fig. 5.2). By combining $I(x)$ and $x(t)$ we can derive the desired current ramps $I(t)$ (see Fig. 5.3). However, since the power supplies show a typical low pass behavior, the current ramps cannot directly be fed into the respective modulation inputs. In fact, it is necessary to accurately record the frequency response of the power supplies and to correct for the low pass behaviour.

With the procedure described here we are able to move the cloud over a distance of 431.2 mm within a time of 1.5 s. The final particle number after transport is typically $5\times10^8$, corresponding to an overall efficiency of about 50%. The temperature of the atom cloud increases from initially 150 µK to about 230 µK.

### 5.1.4 QUIC trap and evaporative cooling

The first step of loading the atoms into the QUIC trapping potential is to increase the current through the QUIC quadrupole coils within a duration of 1.5 s from 16 A to the maximal steady state value of 36 A. The corresponding maximum magnetic field gradient is $\partial B/\partial z = 320\,\mathrm{G/cm}$.

At this point we start rf-induced forced evaporative cooling to reduce the temperature of the atom cloud. To selectively remove hot atoms, a small coil with 3 turns and a diameter of about 20 mm is placed inside the vacuum at the bottom of the chamber at a distance of 13 mm from the atoms. The coil is driven with 30 dBm of rf power. The rf is generated with a direct digital synthesizer (DDS) board from Analog Devices (AD9854). The DDS allows to smoothly change

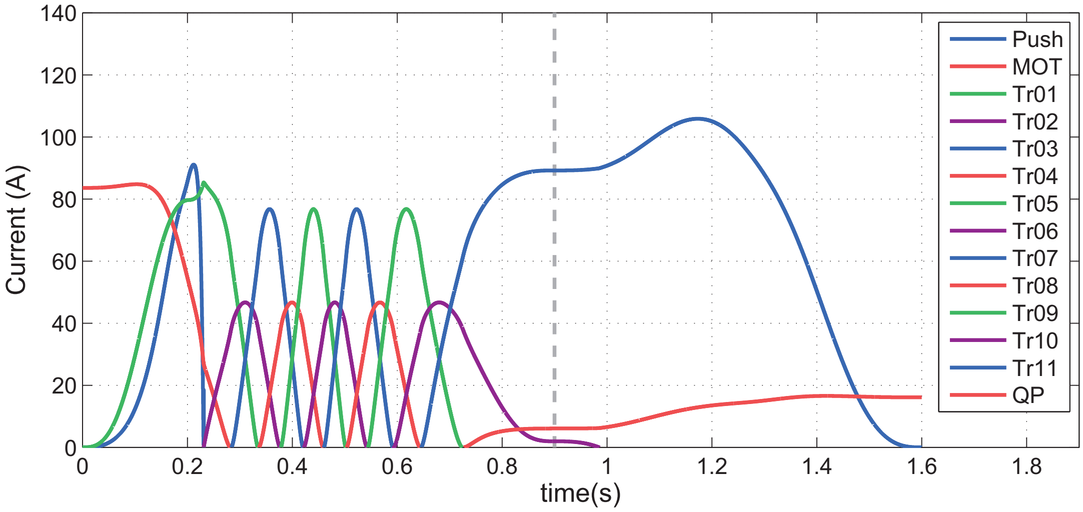

Figure 5.3: Transport currents as a function of time for the optimum duration of 1.6 s. The dashed line at 0.9 $s$ indicates the point of time, when the atom cloud is at the intermediate position of 385 mm.

the frequency while keeping the rf phase coherent. In our case the frequency is ramped linearly from 70 MHz to 40 MHz within 3 s and from 40 MHz to 10 MHz within 5 s. At this point the atom temperature is about 70 micro K and Majorana losses start to play a role. Therefore the current through the Ioffe coils is also ramped up to 36 A within a time of 0.8 s. At the end of the ramp the quadrupole coils and the Ioffe coil are connected in series and driven by a single power supply. Having all the QUIC coils wired up in the same circuit minimizes heating of the atom sample and leads to a 1/e lifetime of the cloud on the order of 2 min. The QUIC coil system generates an offset magnetic field of about 2 G and close to the center a nearly harmonic potential with trapping frequencies of $(\omega_x, \omega_y, \omega_z) = 2\pi\times(105, 105, 20)$ Hz.

In the QUIC trap the evaporative cooling is continued by ramping the rf within a time of 5 s exponentially from 10 MHz down to about 3 MHz. With this procedure we are able to produce Bose-Einstein condensates of up to $3\times10^5$ atoms (BEC transition temperature $T_c \approx 100$ nK). However, we usually stop the evaporation when the temperature of the cloud is on the order of 1 µK and the atom number is about $2\times10^6$. This way we are able to work with larger atomic samples in our science chamber.

Here I would like to point out that we achieve final particle numbers of $2\times10^6$ only when we start the rf evaporation in the quadrupole trap, i.e. before the current through the Ioffe coil is ramped up. With this procedure we avoid that atoms get into contact with the chamber walls, after they have been loaded from the steep quadrupole trap into the shallow QUIC trap. As a result, we find that preventing the atoms from collisions with the chamber walls leads to an increase of the final atom number.

## 5.2 Optical trapping of the atoms

As discussed so far, we have used magnetic fields to trap the atom cloud during its preparation. However, after the 1 µK cold atomic sample has been generated, it is loaded into an optical trapping potential for the following reasons.

A moving 1-d optical lattice is employed for the transport of the atoms from the BEC chamber to the science chamber. Since we only need two counter-propagating laser beams to form such a lattice potential, the optical transport setup is very simple compared with other methods (such as a magnetic transport). Moreover, the optical transport scheme works for arbitrarily cold atom samples, provided that a small magnetic offset field is present along the transport line.

Once the atoms have arrived in the center of the ion trap, they are loaded into a crossed optical dipole trap. Since the depth of the dipole trap is orders of magnitude lower than the one of the Paul trap, the influence of the optical trap on the ion can be neglected. Another advantage of the dipole trap is that its position can be adjusted fast and easily. As we will see later, this feature is essential for the optimization of the overlap between the atoms and the ion.

### 5.2.1 The Dipole force

In the presence of a laser light field the atomic energy levels are shifted due to the AC Stark effect [48, 50]. The shift arises from the electric dipole interaction between the atom and the laser field. Its magnitude can be calculated using time-dependent perturbation theory.

Optical dipole traps are operated far-detuned from the atomic resonance, so that the photon scattering rate is typically much smaller than the linewidth of the transition. Thus the atoms spend basically all the time in the electronic ground state. Under these conditions the optical dipole potential is directly given by the AC Stark shift of the atomic ground state.

In our experiment the Rb atoms are optically trapped using a fiber amplified solid state laser at $\lambda = 2\pi c/\omega = 1064\,\text{nm}$ (see section 3.3.3). A laser intensity distribution of $I(x, y, z)$ then leads to a potential of the form [50]

$$U_{\text{dip}}(x, y, z) = -\frac{3\pi c^2 \Gamma}{2\omega_0^3} \left( \frac{1}{\omega_0 - \omega} + \frac{1}{\omega_0 + \omega} \right) I(x, y, z) \tag{5.1}$$

where $\omega_0$ is the transition frequency of the relevant atomic transition, which in our case is the 5S→5P transition in Rubidium. For the calculation of $U_{\text{dip}}$ the fine structure splitting of 5P level can be neglected, since it is much smaller than the detuning of the trapping laser from the atomic resonance. Rather, we can work with the mean transition frequency

$$\omega_0 = \frac{1}{2}\omega_1 + \frac{2}{3}\omega_2 \tag{5.2}$$

which can then be calculated as a weighted average of the frequencies of the two Rb D-lines $2\pi c/\omega_1 = 795\,\text{nm}$ and $2\pi c/\omega_2 = 780\,\text{nm}$. With these values we find $2\pi c/\omega_0 = 785\,\text{nm}$. The (average) transition linewidth is given by $\Gamma = 2\pi \times 5.9\,\text{MHz}$ [32].

Since our trapping laser is red-detuned from the atomic resonance $\omega < \omega_0$, the atoms are stored in the intensity maxima of the trapping beams. Therefore it is necessary to estimate the heating rate of the atomic sample due to scattering of photons from the trapping beam. The maximal photon scattering rate is given by

$$\hbar\Gamma_{\text{scatt}} \approx U_0 \frac{\Gamma}{\omega_0 - \omega}, \tag{5.3}$$

where $U_0$ is the depth of the dipole potential. For all the dipole potentials used in our setup $U_0$ is chosen such that $1/\Gamma_{\text{scatt}}$ is larger than then typical trapping time.

### 5.2.2 Transport of ultracold atoms using a moving optical lattice

A key feature of our experiment is the long-distance optical transport of the ultracold atoms. This transport scheme allows us to separate the science chamber from the BEC chamber by a macroscopic distance of 30 cm. Thereby we are able to avoid mutual disturbance between the Paul trap and the setup used to generate the Rb quantum gas. In particular we minimize the heating of the ions due to the rf radiation needed for evaporative cooling of the atoms. In the future this feature might make our apparatus superior over other atom-ion experiments, since it makes it easier to reduce the ion energy and thus to enter the regime of ultracold atom-ion collisions.

During transport the ultracold Rb atoms are stored in the nodes of a 1-d optical standing wave. We achieve the confinement with the optical dipole force, as described above. By introducing a detuning between the two counterpropagating lattice beams the standing wave nodes and therefore the atoms are moved. With this transport scheme we are able to control the position of the atoms very precisely. Furthermore, the moving lattice transport is very reliable with an almost perfect reproducibility.

Before I describe our transport technique in more detail, I will summarize the previous efforts of transporting BECs with far-off-resonant laser fields.

### Introduction - earlier transport experiments

For the optical transportation of quantum-degenerate gases two different methods have already been implemented successfully. On the one hand the group of Wolfgang Ketterle has trapped BECs in so-called optical tweezers, generated by the focus of a far-off-resonant laser beam. By moving the focussing lens they have managed to transport the condensate over a distance of about 40 cm [51]. On the other hand ultracold atoms have been moved over macroscopic distances of up to 20 cm using a 1-dimensional optical lattice [52–54]. To set the interference pattern and thus the atoms in motion, a relative detuning between the two counterpropagating lattice beams is introduced. The major issue of this transport scheme is the vertical confinement. In order to avoid that gravity drags the atoms out of the lattice potential, the waist of the lattice beams needs to be sufficiently small. However, due to the wave nature of the light a small waist is directly linked to a small Rayleigh range and thus to a large divergence of the beam. Therefore, ordinary Gaussian laser beams are not well suited to generate the 1-d lattice needed for a horizontal long distance transport of atoms. One possible solution to this problem is to exchange one of the Gaussian-shaped lattice beams with a so-called "Bessel beams". A Bessel beam allows for holding the atoms against gravity along the entire transport line [53]. A drawback of this technique is the fact that special and more expensive optics (e.g. a conical lens or holographic elements) is needed to generate the Bessel beam [54]. Moreover, most of the Bessel beam's power is not carried by the central spot, in which the atoms are trapped, but by the outer rings of the beam. Therefore an increased amount of laser power is needed to create a Bessel beam with which ultracold

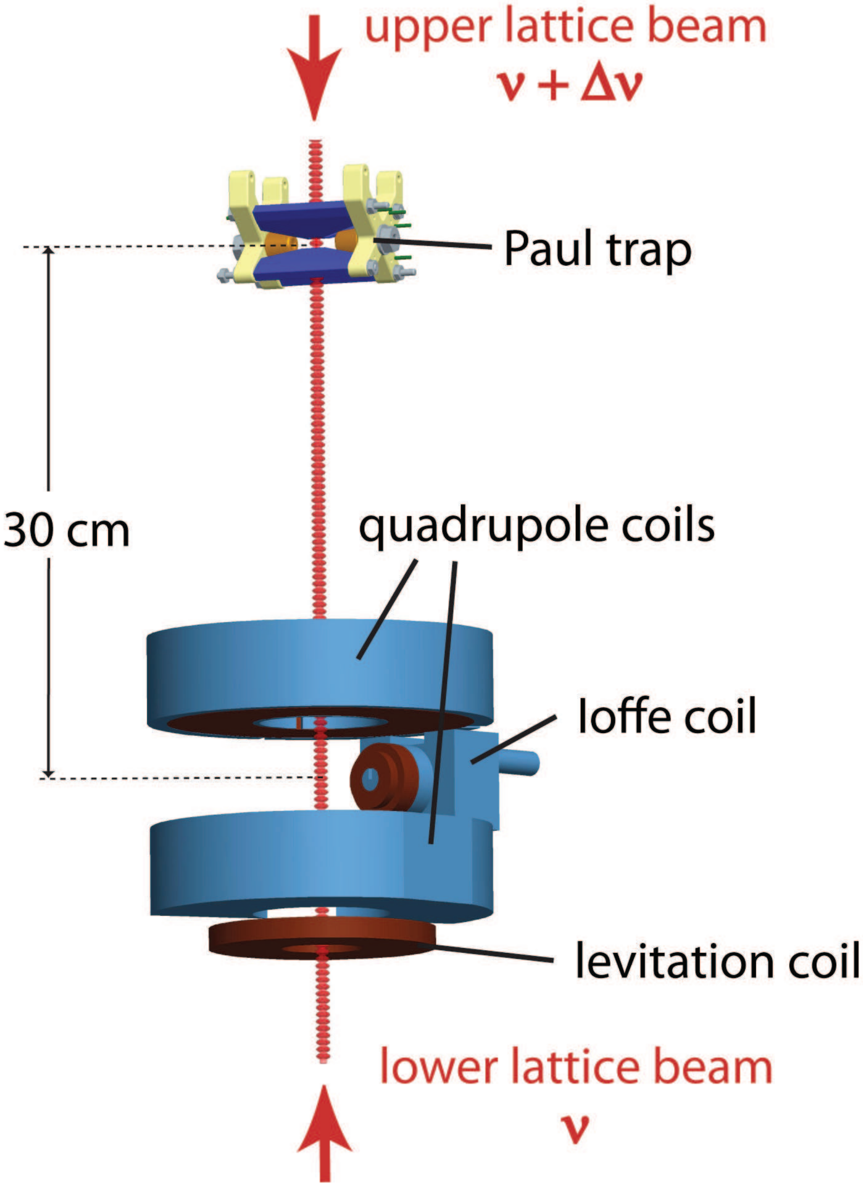
upper lattice beam
$\nu + \Delta\nu$
Paul trap
30 cm
quadrupole coils
Ioffe coil
levitation coil
lower lattice beam
$\nu$

Figure 5.4: An optical standing wave is used to transport the ultracold atoms from the BEC chamber into the science chamber

atoms can be trapped.

In the BaRbI experiment we require a transport technique with which we can move ultracold atoms over a distance of 30 cm. A 1-dimensional moving Bessel-Gauss lattice, as described above, would be well-suited for this purpose. However, in our setup we wanted to avoid the usage of Bessel beams, due to the drawbacks discussed before. Therefore, we have decided to build the experiment such that the atoms get transported vertically. In this case the strong axial confining force $F_{\mathrm{ax}}$ points along the direction of gravity. And since $F_{\mathrm{ax}}$ can easily be made larger than the gravitational force for any realistic beam diameter, it is sufficient for a vertical transport to use two Gaussian beams.

### The 1-d optical lattice potential

Our 1-d optical lattice is formed by two counterpropagating Gaussian laser beams, which are traveling along the vertical z-direction. Both beams have a waist of $w_0 = 500\,\mu\mathrm{m}$ and are slightly focussed onto the same spot located right in between the BEC and the science chamber. The intensity distribution of the resulting standing wave pattern is then given by

$$\begin{aligned} I(r,z) &= |\sqrt{I_1}e^{-r^2/w_0^2}e^{ikz} + \sqrt{I_2}e^{-r^2/w_0^2}e^{-ikz}|^2 \\ &= \left(I_1 + I_2 + 2\sqrt{I_1 I_2}\cos(2kz)\right)e^{-2r^2/w_0^2}, \end{aligned} \tag{5.4}$$

where the distance between two consecutive nodes is $\lambda/2 = \pi/k = 532\,\mathrm{nm}$. The beam intensities $I_1$ and $I_2$ are derived from

$$I_{1,2} = \frac{2P_{1,2}}{\pi w_0^2} \tag{5.5}$$

with the power of the beams being $P_1 = 1.5\,\mathrm{W}$ and $P_2 = 0.5\,\mathrm{W}$.

Here we have neglected the divergence of the trapping beams. This assumption is valid, since the Rayleigh range $z_{\mathrm{R}} = \pi w_0^2/\lambda = 74\,\mathrm{cm}$ is much larger than the transport distance.

By plugging (5.4) into (5.1) we get the expression for the trapping potential

$$U(r,z) = \left(-U_0 + U_{\mathrm{latt}}\sin^2(kz)\right)e^{-2r^2/w_0^2} \tag{5.6}$$

where total trap depth $U_0$ and the modulation depth of the lattice $U_{\mathrm{latt}}$ are given by

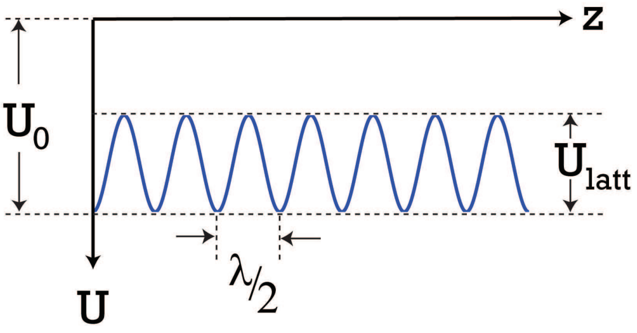

Figure 5.5: The total trap depth $U_0$, the lattice depth $U_{\text{latt}}$ and the periodicity $\lambda/2$ of the potential are illustrated.

$$U_0 = \frac{\pi c^2}{2\omega_0^3}\frac{\Gamma}{\Delta}\left(I_1 + I_2 + 2\sqrt{I_1 I_2}\right) \tag{5.7}$$

$$U_{\text{latt}} = \frac{\pi c^2}{2\omega_0^3}\frac{\Gamma}{\Delta}4\sqrt{I_1 I_2} \tag{5.8}$$

Close to the potential minima we can make a harmonic approximation of (5.6) and calculate the trap frequencies

$$\omega_r = 2\pi f_r = \sqrt{\frac{4U_0}{mw_0^2}} \tag{5.9}$$

$$\omega_z = 2\pi f_z = k\sqrt{\frac{2U_{\text{latt}}}{m}} \tag{5.10}$$

### Loading of the lattice

After evaporative cooling in the magnetic QUIC trap the atom cloud has a temperature of 1 µK and a particle number of about $2 \times 10^6$. The ultracold atoms are loaded into the standing wave trap by smoothly ramping down the currents through the QUIC coils and by simultaneously ramping up the power of the lattice beams. A long loading time of 300 ms is chosen in order to keep the heating of the atoms small and the efficiency of the loading process high. Moreover, for a high loading efficiency it is obviously necessary to maximize the spatial overlap between the magnetic trap and the optical lattice.

At first a coarse overlap between the two traps is established with the following procedure. A resonant 780 nm laser beam is sent along the optical transport axis. It is aligned in such a way that it passes exactly through the center of the ion trap. Furthermore we assure that the beam also hits the center of the magnetically trapped atom cloud by maximizing the atom loss due to the (almost) resonant light. Subsequently, the first 1064 nm lattice beam is aligned precisely along the 780 nm beam. In a third step we exchange the 780 nm beam by the second 1064 nm lattice beam and walk the new beam until the relative alignment between the two lattice beams has reached an optimum.

An even finer overlap between the 1d lattice and the magnetically trapped atoms is subsequently achieved with the diffraction technique described in [55]. For this purpose we load the atoms non-adiabatically into a moving 1-d optical lattice. Due to the abrupt turning-on of the lattice potential the atomic wave function (plain wave) $|\phi_{\mathrm{q}}\rangle$ is projected on the Bloch eigenstates $|n, q\rangle$. Here $n = 1, 2, ...$ is the $n$-th Bloch band and $q$ the initial momentum of the atoms relative to the lattice. The subsequent dynamics crucially depends on the lattice potential experienced by the atoms. When the lattice is turned off again the wave function is projected back onto the plain wave basis, which consists of the eigenvectors $|\phi_{q+2n\hbar k}\rangle$, where $2\pi/k = 1064\,\mathrm{nm}$. In our case we have chosen the relative momentum to be $q = \hbar k$, corresponding to a relative detuning between the two lattice beams of $2\hbar k^2/m$. To reveal the momentum distribution of the atom sample after the lattice pulse, we perform time-of-flight imaging. We find only the $|\phi_0\rangle$ and the $|\phi_{2\hbar k}\rangle$ momentum state to have relevant populations. To optimize the overlap between the lattice and the atoms, we set the length of the lattice pulse such that initially the majority of the atoms is in the $|\phi_0\rangle$ state and only a small fraction occupies the $|\phi_{2\hbar k}\rangle$ state. By adjusting the position of our magnetic trap for this fixed pulse length, we then maximize the population of the $|\phi_{2\hbar k}\rangle$ state and thus the spatial overlap.

Along the Ioffe axis the atom cloud is moved by changing the current through the quadrupole coils, while keeping the Ioffe current constant. On the other hand for slight position changes along the imaging axis (which is orthogonal to the Ioffe axis) we operate the last pair of the magnetic transport coils. For the (third) vertical direction a precise optimization of the atom position is not necessary, since the atoms can be loaded into any node of the optical lattice. However, we need to assure that establishing the overlap along the two horizontal directions, does not change the height of the atoms by more than few hundred microns.

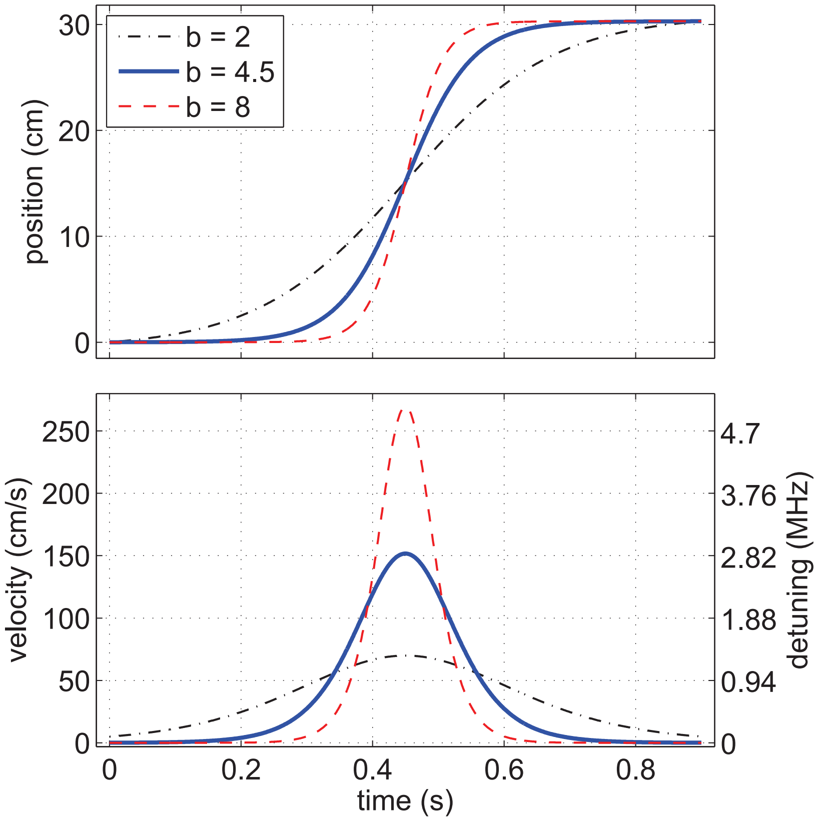

Figure 5.6: The transport ramps are shown for a transport distance of $D = 304\,\mathrm{mm}$, a transport time of $T_{\mathrm{trans}} = 0.9\,\mathrm{s}$ and three different form parameters $b = 2$, $b = 4.5$ and $b = 8$. The transport efficiency is found to maximal for $b = 4.5$ (blue solid line). (a) Position $y(t)$ of the atoms versus time. (b) Velocity $v(t)$ of the atoms and the corresponding relative detuning between the lattice beams $\Delta\nu(t)$ versus time.

Otherwise the atom cloud would leave the field-of-view of our imaging system. For this reason we add a levitation coil (Fig. 5.4) to our system, with which we can also control the vertical position of the atoms.

Eventually, when the overlap between the magnetic trap and the optical trap is optimized, the population of the individual momentum states $|\phi_{2n\hbar k}\rangle$ is measured as a function of the diffraction pulse length. From this time evolution of the momentum states it is possible to determine the lattice depth $U_{\mathrm{latt}}$ [55, 56]. Typical values are $U_{\mathrm{latt}} \approx 5E_r$, where the recoil energy is given by $E_r = (\hbar k)^2/2m$.

### Vertical lattice transport

Like an elevator, the lattice drags along the atoms over a distance of $D = 304\,\mathrm{mm}$ from the BEC chamber into the science chamber. To make the standing wave move with a velocity $v$ we introduce a relative detuning

$$\Delta\nu = \frac{2v}{\lambda} \tag{5.11}$$

between the two lattice beams. We choose the ramp $\Delta\nu(t)$ such that the atom position $y(t) = \int_0^t v(t')dt'$ obeys the relation

$$y(t) = \frac{D}{2\tanh(b)} \left[\tanh\left(b\left(2t - T_{\mathrm{trans}}\right)/T_{\mathrm{trans}}\right) + \tanh(b)\right], \tag{5.12}$$

where $T_{\mathrm{trans}}$ is the duration of the transport and $b$ a variable form parameter [57]. In Fig. 5.6 the atom position and the velocity are plotted for three different values of $b$. In the limit $b \to 0$ the curve $y(t)$ has a linear behavior, whereas for $b \gg 1$ $y(t)$ is a step function. For a given transport distance $D$, the transport time $T_{\mathrm{trans}}$ and the form parameter $b$ are optimized for maximum transport efficiency. In our case with $D = 304\,\mathrm{mm}$ we find a maximum efficiency of 60% for $T_{\mathrm{trans}} = 0.9\,\mathrm{s}$ and $b = 4.5$.

In addition, we have shown that the optical transport may be extended to even larger distances. As a proof of principle we have transported the atom cloud from the BEC chamber over 45 cm to the very top of the science chamber and then back into the BEC chamber again. In this experiment the total roundtrip distance covered is 90 cm and is only limited by the extension of our vacuum apparatus.

### Final position of the lattice transport

The lattice transport distance $D$ has to be chosen such that at the end of the transport the atoms are located right in the center of the ion trap. In a first step, to find an approximate value for $D$, we determine the position of the atom cloud relative to the RF electrodes via standard absorption imaging. We set $D$ such that the atoms roughly end up midway in between the lower and the upper electrodes.

For a more precise adjustment, we load a cloud of $\mathrm{Rb}^+$ ions into the Paul trap. We then transport the atom cloud into the trap, hold it for 1 s at the final position, and take an absorption image. In the region where the ion cloud

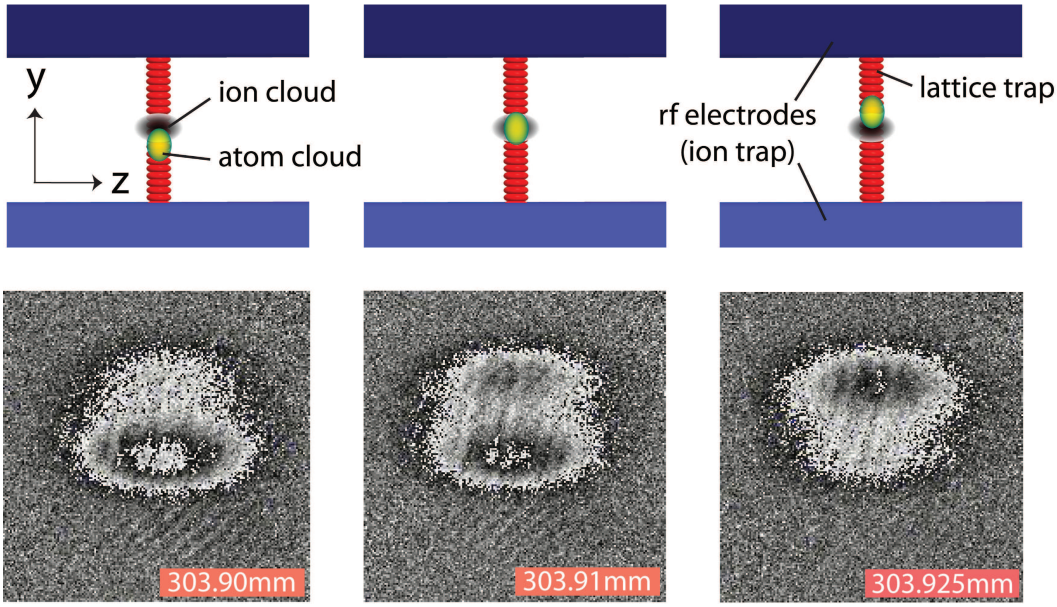

Figure 5.7: Absorption images of the atom cloud after it is transported into or close to the center of the ion trap. The Paul trap is loaded with hundreds of $\mathrm{Rb}^+$ ions, which are responsible for the localized loss of atoms around the trap center. Outside of the trap center the atom loss is very small, since the strong lattice confinement along the direction of transport (y-axis) keeps the atoms away from the ions. The transport distance is varied between 303.90 mm to 303.925 mm. The pictures are taken after the atoms are held at the final position for a duration of 1 s and after a time-of-flight of 12 ms.

is located we observe a substantial loss of atoms, as shown in Fig. 5.7. (For a detailed discussion on the mechanism of the atom loss, I would like to refer to the chapter 6.) The strong confinement in the 1-d optical lattice prevents atoms, which are located outside the central region, from colliding with the ions. Thus, only a minor atom loss is observed in this outside section. We adjust the transport distance $D$ such that the maximal atom loss appears right in the center of the atom cloud (see Fig. 5.7).

By analyzing the total number of lost atoms, we can also optimize the overlap between atoms and ions along the two horizontal directions within the x-z plane. The atom loss is larger when the ions are placed at a position of higher atom density. Once the final position of the lattice transport is roughly overlapped, the atoms are loaded from the lattice into the crossed dipole trap.

### Preparation of the lattice beams

The light for the lattice beams is derived from a fiber-amplified solid state laser (Mephisto from the company Innolight). Due to its very narrow spectral linewidth (1 kHz) the laser is well suited for the generation of an optical lattice. Both beams are sent through acousto-optical modulators (AOMs) in order to be able to control their frequency as well as their intensity. At the beginning of the transport both AOMs are driven with a radiofrequency of 80 MHz. For the transport scheme to work, it is essential that both radiofrequencies are kept phase locked to each other throughout the entire transport sequence. Therefore the rf signals are generated using direct digital synthesizers (AD9854), which can be locked to the same external reference oscillator. In order to make the standing wave pattern move with a velocity $v = \Delta\nu\,\lambda/2$, we detune the frequency of the upper lattice beam by $\Delta\nu$ (Fig. 5.6). The AOM frequencies and thus also the values for the detuning $\Delta\nu(t)$ are updated with a rate of 24 kHz. Modifying the AOM frequency changes the diffraction angle and the beam path. To preserve the alignment of the lattice throughout the transport it is thus necessary to couple the upper lattice beam through an optical fiber before sending it to the experiment. The fiber coupling limits the power of the upper lattice beam to about 500 mW. The lattice beams enter and exit the vacuum system through AR-coated viewports, which are welded to the chamber at an angle of about 4° with respect to the (vertical) propagation axis. Thereby we ensure that the reflections at the viewports do not modify or even destroy the standing wave pattern. Unwanted back-reflections from other optical elements along the beam path (such as lenses, beamcubes, etc.) are filtered by placing 40 dB optical isolators right before the viewports.

At this point I would like to mention that we have spent quite some time on experimentally figuring out the proper waist for the two lattice beams. On the one hand, if the waist becomes too large, the central intensity of the beam will be very small. On the other hand if the waist gets too small, the divergence of the beam will be very large and thus a transport over a macroscopic distance will be impossible. For this reason we have performed the optical transport of our atoms for various values of the waist. The position and the value of the waist are measured by redirecting the beams before they enter the vacuum apparatus. For the best value of the waist, the laser power required for the transport to work is minimized. This procedure can be very time-consuming, since the lattice has to be completely realigned once the waist of the beams is changed.

### 5.2.3 Crossed dipole trap

#### The dipole trap

After transport the atoms are loaded into a crossed optical dipole trap, formed by the lower lattice beam and an additional dipole trap beam. This additional dipole beam is derived from the same laser as the lattice beams and propagates horizontally and at an angle of 45° with respect to the ion trap axis (Fig. 5.8). It has a waist of 50 µm and a corresponding Rayleigh range of 7 mm. One more AOM is used to control the power of the dipole beam and to shift its frequency such that an interference with the lattice beams is avoided.

Altogether the loading of the dipole trap takes 3 s. In a first step the power of the lower lattice beam is increased from 1.7 W (lattice setting) to about 3.5 W (dipole trap setting) within 1 s. After 0.5 s the power of the dipole beam is ramped up to about 1 W within 1 s and finally the power of the upper lattice beam is lowered to zero again within 1 s. The depth of the resulting dipole trap potential is on the order of a 2µK. We are able to load about 50% of the atoms from the optical lattice into the crossed dipole trap.

#### Evaporative cooling

We start the final evaporation stage with up to $2\times10^6$ atoms. By exponentially decreasing the power of the dipole beam and thus the depth of the dipole trap within a time span of 4 s, we perform evaporative cooling until quantum degeneracy is reached. We typically end up with pure BECs of up to $1\times10^5$ atoms. Optionally we stop the evaporation right before the onset of Bose-Einstein condensation ($T \approx 100\,\mathrm{nK}$), in case we want to work with an ultracold thermal atom cloud. The final trap frequencies are found to be $(\omega_{x'}, \omega_y, \omega_{z'}) = (8\,\mathrm{Hz},\ 60\,\mathrm{Hz},\ 60\,\mathrm{Hz})$.

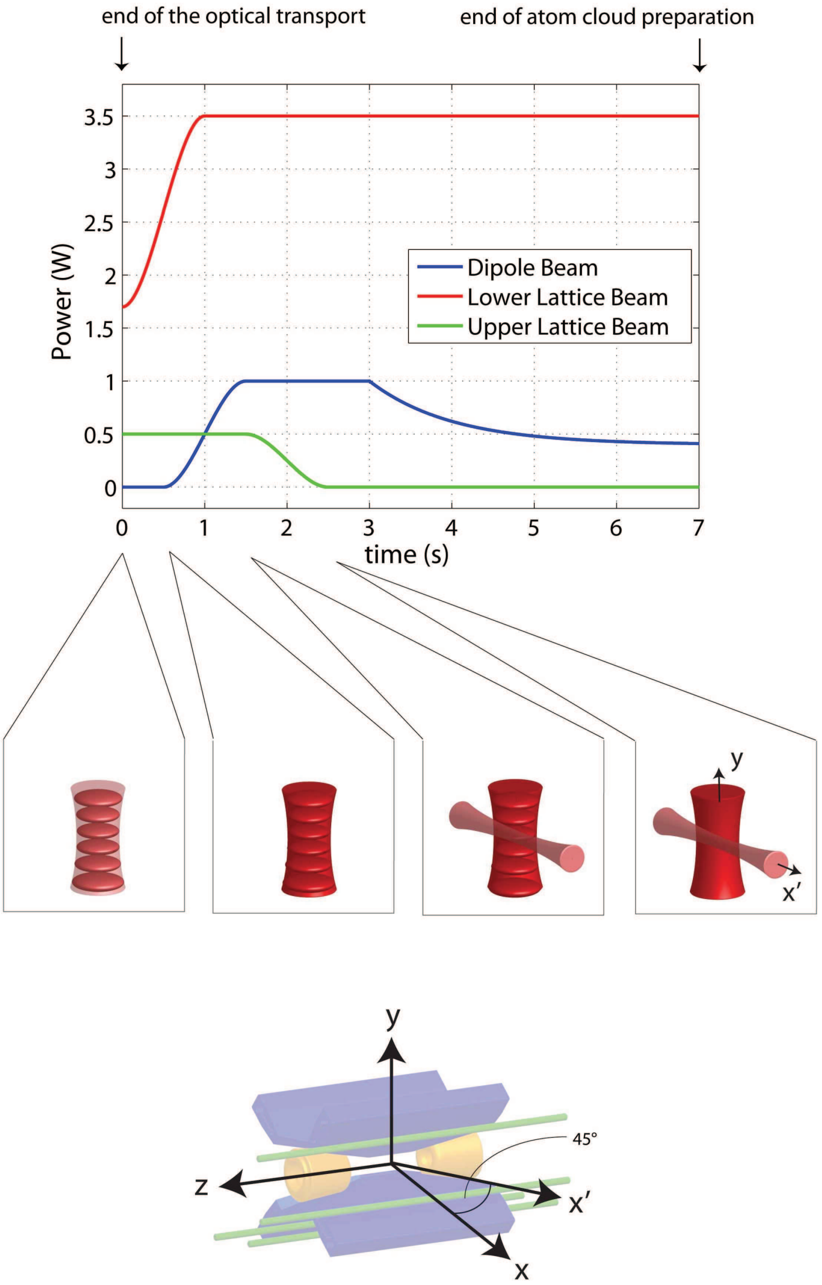

Figure 5.8: Laser powers of the trapping beams during loading of the dipole trap and during final evaporative cooling of the atoms. The crossed dipole trap is formed by the lower lattice beam and the dipole beam. The latter one propagates horizontally at an angle of 45° with respect to the x- and the z-axis, respectively. For evaporative cooling of the atomic sample, the power of the dipole beam is ramped down exponentially.

# Chapter 6

# Collisions of cold ions with ultracold neutral atoms

In the previous chapters I have explained the theoretical groundwork as well as our experimental approach for studying collisions of a cold trapped ion with ultracold neutral atoms. Now, I will present the first experimental data that we have obtained with our novel hybrid apparatus.

These first results include the observation of elastic atom-ion collisions on our setup, which we detect via the loss of atoms in the presence of the ion. By measuring the lifetime of the atom cloud and making a simple model of the atom-ion collision we find rough values for the corresponding collision rate and the collision cross section as well as for the typical collision energy ($\sim$ ion energy). This simple model is sufficient to explain our first results presented here and published in [18]. However, a more sophisticated model has to be used to describe the newest measurements made with our apparatus. For more details on the recent developments I need to refer to the final chapter 7.

Besides elastic collisions we have also observed charge transfer collisions in our experiment, which can be detected via a loss of the $Ba^+$ fluorescence. The corresponding collision rate (or cross section, respectively) is estimated by comparing the number of charge transfer collisions to the amount of elastic collisions. Also, we have already investigated one possible application of our setup in more detail. By varying the relative position between atoms and ion, we have demonstrated that a single ion can be used to probe the density profile of an ultracold atom cloud.

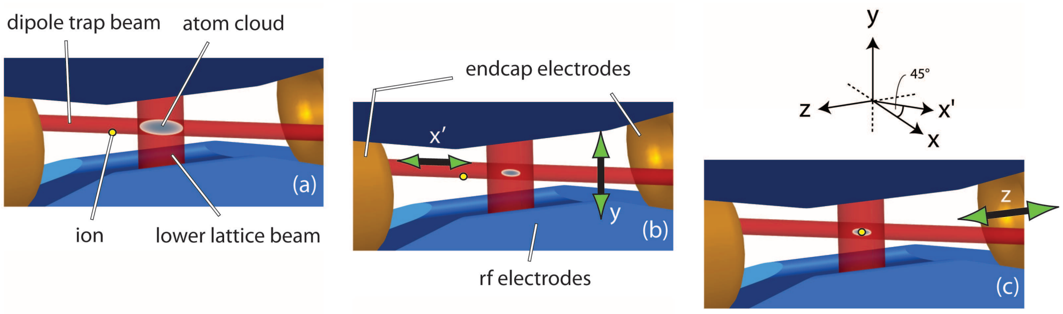

Figure 6.1: Overlapping the position of the ultracold atoms with the position of the trapped ion. (a) and (b) The ion is located on the $z$-axis at a distance of about 300 µm away from the atom cloud. (b) The atoms are cooled evaporatively to or close to BEC. The relative overlap within the $x'$-$y$ plane is achieved by properly adjusting the AOM frequencies. (c) By changing one of the endcap voltages, the ion is shifted along the Paul-trap axis ($z$-axis) into the center of the atom cloud.

### Overlap between the ion and the atoms

Prior to the investigation of the atom-ion collision dynamics we have to bring the ion and the atom cloud together. For this purpose we follow the procedure illustrated in Fig. 6.1. First, the atoms are loaded into the crossed dipole trap and are further cooled to either a temperature of $T_{\text{atoms}} \approx 250\,\text{nK}$ or to BEC (see section 5.2.3). At this stage the center of the atom cloud is located about 300 µm away from the ion. Then the cooling lasers for the ion are switched off in order to ensure that the ion relaxes into its electronic ground state $|F = 1/2,\ m_F = \pm 1/2\rangle$ and to avoid changes in the atom-ion collision dynamics due to the cooling radiation. Subsequently the ion is moved within 2 ms along the Paul trap axis ($z$-axis) into the atom cloud by changing one of the endcap voltages. To ensure that the atom and the ion position coincide for all three directions in space, it is essential to have full control over the relative position between the atoms and the ion. As mentioned above, along the z-axis we can move the ion by changing the settings of the endcap voltages. To adjust the relative atom-ion position along the other two directions (x’ and y), the position of the dipole trap is changed by sending the lower lattice beam and the dipole trap beam through AOMs. For this purpose, we use AOMs with a center frequency of 80 MHz and a corresponding Bragg angle of about 10 mrad. Since the bandwidth of such an AOM is typically 10%, the diffraction angle can be varied by about 1 mrad. For distances between the AOMs and the science chamber on the order of 1 m, this results in a shift of the atom trap position by up to 1 mm. Our method to find the proper AOM

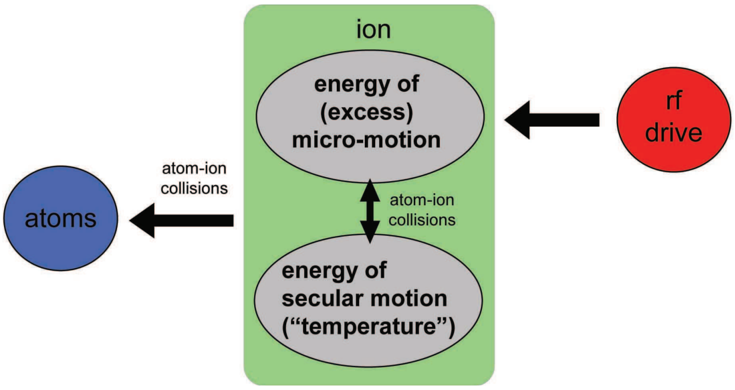
ion
energy of (excess) micro-motion
rf drive
atom-ion collisions
atoms
atom-ion collisions
energy of secular motion ("temperature")

Figure 6.2: The rf drive is constantly pumping energy into the system. In an atom-ion collision this energy can then be transferred from the ion's excess micromotion to the ion's secular motion as well as to the motion of the atom. The amount of transferred energy is usually enough for the atom to leave the dipole trap.

frequencies and endcap voltages for which the overlap between ion and atoms is maximized, is based on the detection of the atom-ion collisions. Therefore we will first discuss the atom-ion collision dynamics in detail and then present more technical details about the optimization of the overlap (see section 6.1.4).

## 6.1 Elastic collisions between a cold ion and ultracold neutral atoms

Elastic collisions are the dominant physical process in our hybrid atom-ion setup. Estimates for its rate can be found by measuring the losses of atoms from their trap. Before the interaction with the ion, the temperature of the atom cloud is $T_{\text{atoms}} \approx 80\,\text{nK}$, which is about a factor of 10 smaller than the depth of the dipole trap $U_{\text{dip}} \approx k_{\text{B}} \times 1\,\mu\text{K}$, as expected for plain evaporative cooling. For this setting of the dipole trap depth no heating of the atomic sample is allowed. Rather, increasing the kinetic energy of one of the atoms, leads to an atom being lost from the trap. Since $T_{\text{atoms}} \ll T_{\text{ion}}$, the atom's kinetic energy is increased after the collision for the vast majority of atom-ion collisions (see chapter 2).

It is important to understand that the dynamics of the atom-ion collisions in our setup is crucially influenced by the rf Paul trap. If the ion was trapped in a static trap, it would be sympathetically cooled to atomic temperatures and the atom loss would stop after a few collisions. In our system, however, we find a continuous decline of the number of trapped Rb atoms as a function of the interaction time (Fig. 6.3). It is the driven micromotion [39] of the rf trap, which is responsible for this continuing loss. In an atom-ion collision, energy can be redistributed among all motional degrees of freedom, enabling also the flux of excess micromotion energy $E_{\mathrm{kin}}^{\mathrm{excess\ micro}}$ to secular motion $E_{\mathrm{kin}}^{\mathrm{secular}}$ (see Fig. 6.2). After each collision, micromotion is quickly restored by the driving rf field. An equilibrium between the energy that is inserted by the driving field and the energy taken away by the lost atoms is reached within a few collisions. Therefore the minimal temperature of a sympathetically-cooled ion stored in a rf trap is determined by the amount of micromotion of the ion [10,58,59]. Since $E_{\mathrm{kin}}^{\mathrm{excess\ micro}}$ can be varied by applying dc electric fields along the radial direction, the kinetic energy of the ion is tunable.

Fig. 6.3 shows the elastic collision measurements with either (a) a thermal cloud of atoms (temperature $T_{\mathrm{Rb\ atoms}} = 80\,\mathrm{nK}$, which is just above $T_c$) or (b) a BEC. Here I want to point out, that the atom losses in our experiment are predominantly determined by atom-ion collisions. For comparison, the lifetime of the atom sample without an ion being present exceeds 15 s. In the following I will analyze the atom loss measurement in detail and show how we can derive order-of-magnitude estimates for the collision cross section and for the ion temperature from our data.

### 6.1.1 Elastic collision cross section - simple model

The position of the ion is fixed up to a length scale that is much smaller than the extension of the atom cloud. The ion is pinned down because it is laser-cooled prior to the collision experiment and because of the high trap frequencies with which it is confined in the Paul trap. Due to this localization of the ion and since atom-ion collisions can only take place in the vicinity of the ion, the atoms are removed locally from the trap. As a consequence, one expects the atomic density distribution to be modified due to the collisions with the ion.

At first, we will discuss a simple model where we neglect this modification of the density distribution. We assume that merely the total atom number $N$ changes with time, according to

$$\dot{N} = -n\sigma_{\mathrm{loss}}v_{\mathrm{rel}} \approx -n\sigma_{\mathrm{elastic}}v_{\mathrm{I}} \tag{6.1}$$

where $n$ the peak density of the atom cloud, when we assume that the ion

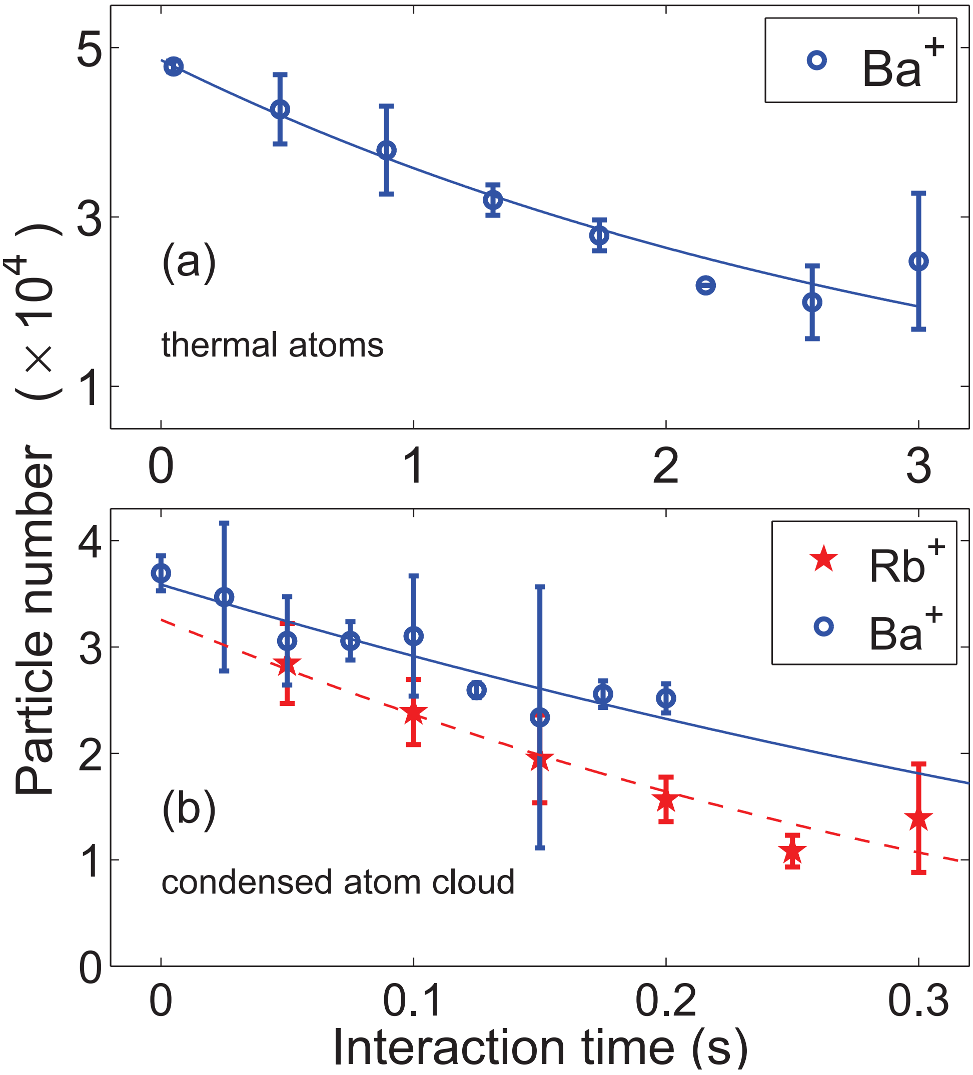

Figure 6.3: Number of remaining Rb atoms as a function of time as a sample of Rb atoms interacts with an ion. For some interaction times the number of datapoints is unfortunately rather small, which results in large errorbars. **(a)** A single $\mathrm{Ba}^+$ ion is immersed into the center of a thermal Rb cloud. The line is an exponential decay fit. **(b)** A single ion ($\mathrm{Ba}^+$ or $\mathrm{Rb}^+$) is immersed in a Rb Bose-Einstein condensate. The lines are fits based on our simple model described in the text.

is placed into the center of the atom cloud. Since for our experimental parameters basically every atom-ion collision leads to an atom being lost from the trap (see discussion at the beginning of the section), the atom loss cross section $\sigma_{\text{loss}}$ is approximately equal to the elastic atom-ion scattering cross section $\sigma_{\text{elastic}}$. Moreover, the atomic velocity is much smaller than the ion velocity $v_{\text{I}}$, so that the relative velocity between atoms and ion is $v_{\text{rel}} \approx v_{\text{I}}$.

For a thermal atom cloud the peak density reads [60]

$$n = N \left( \frac{\bar{\omega}_{\text{atoms}}\, m_{\text{Rb}}\, l_{\text{dB}}}{h} \right)^3 \tag{6.2}$$

with the mean trap frequency for the atoms $\bar{\omega}_{\text{atoms}} = (\omega^{(\text{x})}_{\text{atoms}} \omega^{(\text{y})}_{\text{atoms}} \omega^{(\text{z})}_{\text{atoms}})^{1/3} = 2\pi \times 29\,\text{Hz}$ and the thermal de-Broglie length $l_{\text{dB}} = h/\sqrt{2\pi m_{\text{Rb}} k_{\text{B}} T_{\text{atoms}}}$. By plugging the expression (6.2) into (6.1), we find the solution

$$N(t) = N_0 e^{-\Gamma t}. \tag{6.3}$$

From the fit to the data (Fig. 6.3a) we get $N_0 = 4.8 \times 10^4$ and $\Gamma = 0.30\,\text{s}^{-1}$. With the time constant $\Gamma$ we calculate the elastic collision rate coefficient

$$R_{\text{elastic}} = \Gamma \left( \frac{h}{\bar{\omega}_{\text{atoms}} m_{\text{Rb}} l_{\text{dB}}} \right)^3 = \sigma_{\text{elastic}} v_{\text{I}} \tag{6.4}$$

to be $R = 1.6 \times 10^{-14}\,\text{m}^3\text{s}^{-1}$. Using $v_{\text{I}} = \sqrt{2E/\mu}$ and $\sigma_{\text{elastic}}(E) = \pi \left( \frac{\mu C_4^2}{\hbar^2} \right)^{1/3} \left( 1 + \frac{\pi^2}{16} \right) E^{-1/3}$ [3] we can then estimate the collision energy $E \approx 7\,\text{mK}$ and the elastic scattering cross section $\sigma_{\text{elastic}} \approx 1 \times 10^{-14}\,\text{m}^2$.

One drawback of this analysis is the strong dependence of the collision energy $E \propto \Gamma^6$ on the measurable time constant $\Gamma$, which leads to a large uncertainty for $E$ and for $\sigma_{\text{elastic}}$ of almost one order of magnitude. Another issue of our simple model is obviously the assumption that the density distribution is not modified in the presence of an ion. As we will see in the following, this supposition is not valid, in particular not for high atomic densities (which we find for example for non thermal states). Therefore our model has to be improved such that it allows for a local depletion of the atomic density distribution at the position of the ion.

### 6.1.2 Elastic collision cross section - "sphere of depletion" model

One simple way of taking into account the local depletion of atoms is to introduce a so-called "sphere of depletion" (Fig. 6.4). The size of the sphere is determined by the mean position spread of the ion when it is trapped in a harmonic trap with a mean trap frequency of $\bar{\omega}_\mathrm{I}$. According to the ion's mass $m_\mathrm{I}$ and energy $E_\mathrm{I} = m_\mathrm{I} v_\mathrm{I}^2/2$ this mean position spread is given by

$$R_0 = \sqrt{E_\mathrm{I}/m_\mathrm{I}\bar{\omega}_\mathrm{I}^2}. \tag{6.5}$$

Inside this sphere with radius $R_0$ we assume a homogeneous density $\tilde{n}$ (Fig. 6.4). Right outside the sphere, the density is given by equation (6.2). Similar as in the simple model described before, we write for the atom loss

$$\dot{N} \approx -\tilde{n}\sigma_\mathrm{elastic} v_\mathrm{I}. \tag{6.6}$$

In contrast to equation (6.1), the atom density at the position of the ion is now given by $\tilde{n}$. Here, all three quantities $\sigma_\mathrm{elastic}$, $v_\mathrm{I}$ and $\tilde{n}$ are unknown. However, based on our measurements and additional constraints of our model we can still find estimates for them.

The net flux of atoms into the "sphere of depletion" can be written as

$$\dot{N} = -\pi R_0^2 (n - \tilde{n}) v_\mathrm{thermal} \tag{6.7}$$

where $\pi R_0^2$ is the cross section of the sphere and $v_\mathrm{thermal} = \sqrt{k_B T_\mathrm{atoms}/8\pi m_\mathrm{Rb}} \approx 4.4\,\mathrm{mm/s}$ the thermal velocity of the atoms. By equating (6.7) to (6.6) we find

$$\frac{\tilde{n}}{n} = \frac{\pi R_0^2 v_\mathrm{therm}}{\pi R_0^2 v_\mathrm{therm} + \sigma_\mathrm{elastic} v_\mathrm{I}}, \tag{6.8}$$

From this equation we recognize that $\tilde{n} \propto n \propto N$ for all times, so that the atom number again follows an exponential decay with a lifetime of $1/\Gamma$, as in our simple model described above.

At $t = 0$ (beginning of the interaction) $\dot{N} = N_0\Gamma = 1.5 \times 10^4\,\mathrm{s}^{-1}$ (as can also be read off from Fig. 6.3a) and $n = 9 \times 10^{11}\,\mathrm{m}^{-3}$. By plugging these values into equation (6.7) and additionally setting $\tilde{n} = 0$ we get a lower bound for the ion energy $E_\mathrm{I} \gtrsim k_B \times 17\,\mathrm{mK}$. On the other hand we are able to estimate an upper limit of the ion energy from our micromotion compensation procedure. For this measurement with the thermal atom sample we are able to reduce the DC electric

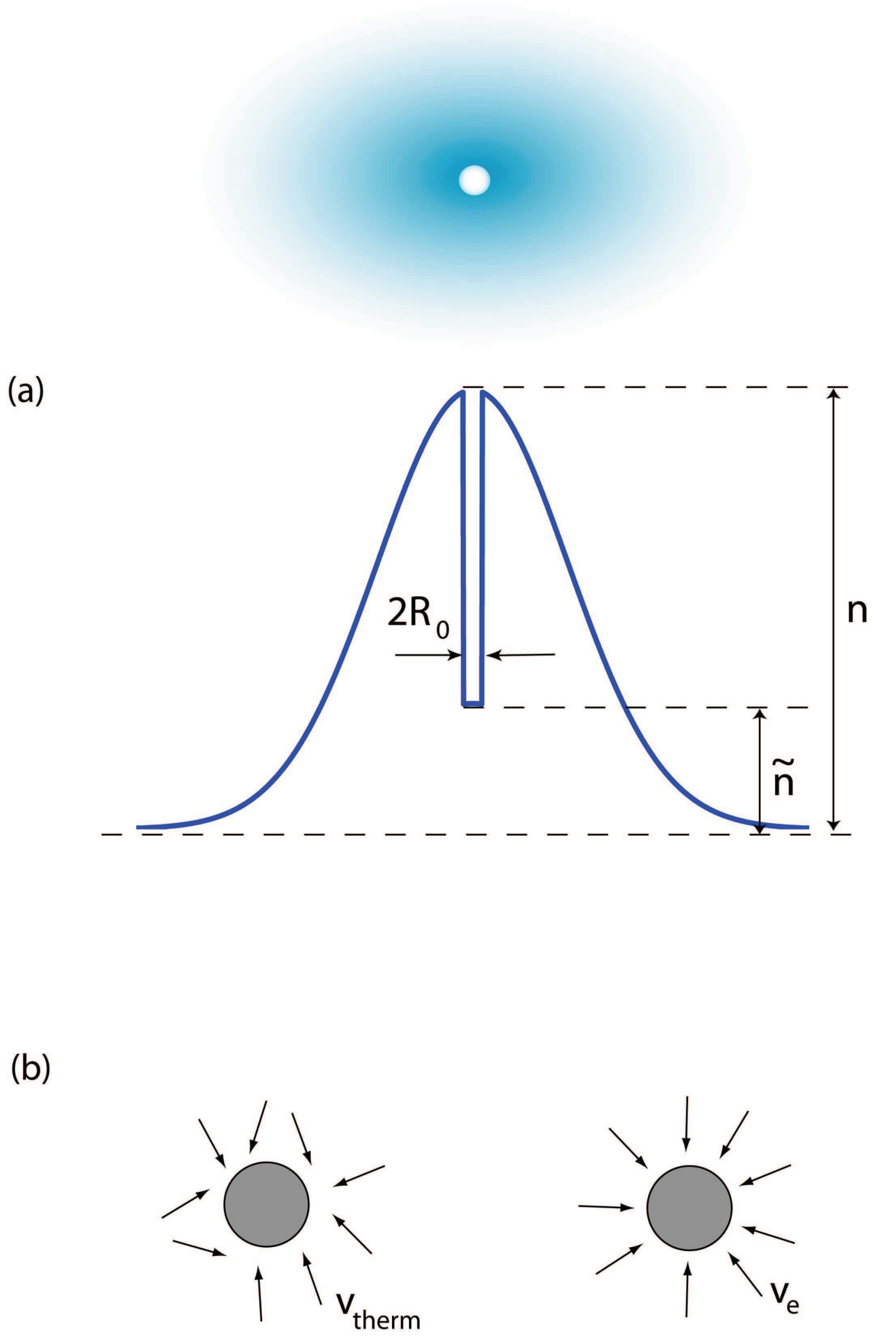

Figure 6.4: **(a)** Illustration of our "sphere of depletion model": The peak density of the atom cloud without an ion being present is $n$. When a single ion is placed into the center of the atom cloud the atomic density distribution is locally depleted. We model this depletion with a sphere of homogeneous density $\tilde{n}$ and radius $R_0$. **(b)** The velocity of the atoms which enter the sphere of depletion has no preferred direction in the thermal case (*left*) and points along the radial direction in the case of a BEC (*right*). This difference has to be taken into account, when one calculates the flux of atoms into the sphere of depletion (equations (6.7) and (6.14)).

field at the position of the ion to below 4 V/m, which gives us $E_{\mathrm{I}} \lesssim k_B{\times}40\,\mathrm{mK}$ using equations (4.31). By taking the midpoint between the two bounds we estimate the ion energy to be about $E_{\mathrm{I}} \approx k_B{\times}30\,\mathrm{mK}$ and thus the collision energy to be $E = E_{\mathrm{I}}\mu/m_I \approx 12\,\mathrm{mK}$. Plugging this energy into (6.5) above we get $R_0 \approx 1.45\,\mu\mathrm{m}$. Using (6.7) and (6.8), we can determine the density $\tilde{n} \approx 0.45\,n$ and the elastic scattering cross section $\sigma_{\mathrm{elastic}} \approx 1.9 \times 10^{-14}\,\mathrm{m}^2$. For comparison, the semiclassical expression yields $\sigma_{\mathrm{elastic}} \approx 9 \times 10^{-15}\,\mathrm{m}^2$ for a collision energy of $E \approx 12\,\mathrm{mK}$.

### Measurement with a BEC (Fig. 6.3b)

A slightly different analysis has to be done for the measurement with the BEC shown in Fig. 6.3b. Again, collisions of the atoms with the trapped ion will lead to a sphere of depletion within the condensate. However, the flux of atoms into the sphere is now driven by mean field pressure rather than thermal motion. Therefore, to find an expression for this flux, analogous to equation (6.7), we study the time evolution of the condensate wave function $\psi(r,t)$ according to the time-dependent Gross-Pitaevskii equation [60]

$$i\hbar\dot{\psi}(r,t) = \left[-\frac{\hbar^2}{2m}\left(\frac{\partial^2}{\partial r^2} + \frac{2}{r}\frac{\partial}{\partial r}\right) + \frac{1}{2}m\bar{\omega}_{\mathrm{atoms}}^2 r^2 + \frac{4\pi\hbar^2 a_s}{m}|\psi|^2 - iV_{\mathrm{loss}}(r)\right]\psi(r,t). \tag{6.9}$$

Here the third term is the well-known mean field interaction, with $a_s$ being the s-wave scattering length between two particles of the condensate (for Rb $a_s = 5.61\,\mathrm{nm}$) and $|\psi|^2$ being the atomic density. Thus, the total number of particles can be calculated with

$$N(t) = \int_0^\infty 4\pi r^2 |\psi(r,t)|^2 dr. \tag{6.10}$$

In our model the particle number is not a conserved quantity, since we have introduced a imaginary potential term $iV_{\mathrm{loss}}(r)$. This term takes into account the losses of atoms due to collisions with the ion. As in the thermal case, we assume that the ion is well localized within a region of radius $R_0$ (see figure 6.4). Therefore we can model our losses with a potential of the form

$$V_{\mathrm{loss}}(r) = C_{\mathrm{loss}}\Theta(R_0 - r) \tag{6.11}$$

where $\Theta(R_0 - r)$ is the Heaviside step function. We then solve the Gross-

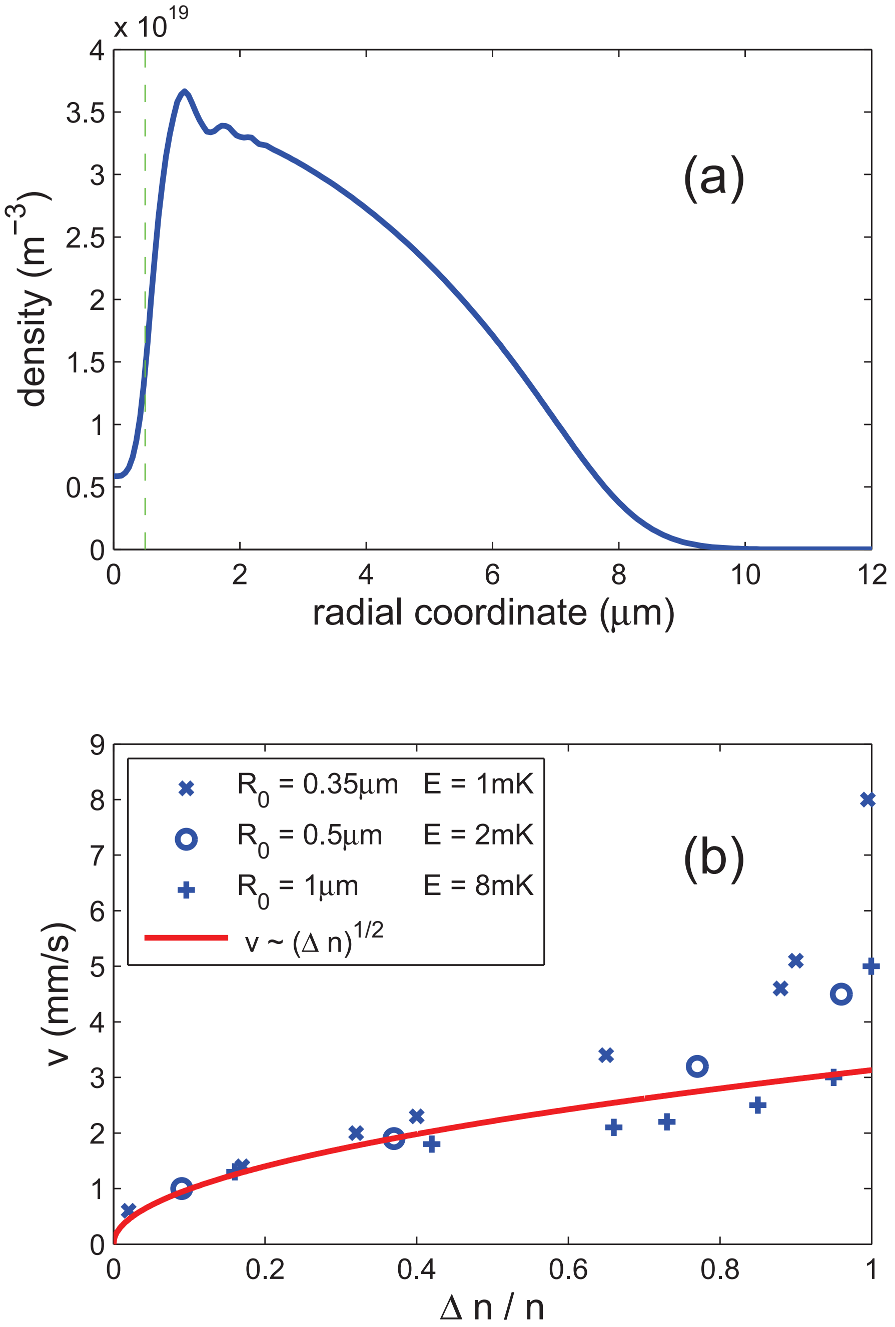

Figure 6.5: **(a)** The numerically derived density distribution $|\psi(r,t)|^2$ for a fixed interaction time $t = 0.1\,\mathrm{s}$. The green dashed line indicates that here we have chosen a typical radius of $R_0 = 0.5\,\mu\mathrm{m}$. **(b)** The velocity with which the atoms enter the sphere of depletion. The datapoints (blue) are calculated numerically by using equation (6.12) and are compared to the analytic expression (6.13) (red line).

Pitaevskii equation (6.9) for different amplitudes of the loss term $C_{\text{loss}}$ and various $R_0$. After a certain interaction time $t$ the atomic density distribution $|\psi(r,t)|^2$ has a shape as given in Fig. 6.5a. In the center at $r = 0$ the density drops to $\tilde{n}$. For $r > R_0$ the density distribution hardly deviates from its original shape at $t = 0$. By studying the dynamics we find that after an interaction time corresponding to an atom loss of typically 5%, $\tilde{n}$ and thus the depletion $\Delta n = n - \tilde{n}$ reach a steady state value. With the wavefunction $\psi$, the maximum velocity with which the atoms enter the sphere of depletion can then be calculated

$$v_e = \frac{\hbar}{m} \max\left(\frac{\partial}{\partial r}\arg(\psi)\right). \tag{6.12}$$

In Fig. 6.5b we have plotted $v_e$ as a function of the depletion $\Delta n = n - \tilde{n}$ and for three different values of $R_0$. The depletion $\Delta n$ is varied by changing $C_{\text{loss}}$. When a condensate atom moves into the sphere of depletion, its mean-field energy is decreased by $4\pi\hbar^2 a_s \Delta n/m$. Assuming that this amount of energy is transferred into kinetic energy of the atom $mv_c^2/2$, we would expect the atoms to have a velocity of $v_c = \hbar\sqrt{8\pi n a_s}/m$. By comparing the result of our simulation $v_e$ with $v_c$, we find for $\Delta n/n \lesssim 0.9$ that

$$v_e = 2v_c = \frac{\hbar}{m_{\text{Rb}}}\sqrt{32\pi a_s(n - \tilde{n})}. \tag{6.13}$$

For $\Delta n/n \to 1$ the deviation of $v_e$ from this analytic expression (6.13) becomes large and starts to depend on the size of the sphere of depletion $R_0$ (see Fig. 6.5b). With our simulation we have also verified that the net flux of atoms into the sphere of depletion and can be written as

$$\dot{N} = -4\pi R_0^2 \tilde{n} v_e. \tag{6.14}$$

Here it is important to note that the atom flux cross section is not given by $\pi R_0^2$, as in the thermal case, but by the surface of the sphere $4\pi R_0^2$. The reason for this difference between the two cross sections can be understood by the fact that $v_e$ points along the radial direction, in contrast to $v_{\text{therm}}$, which has an arbitrary direction (Fig. 6.4b).

We have checked that our model is self-consistent. For this purpose we compared the value for the particle loss derived from the analytic expression (6.14) with the numerical value directly obtained from the simulation (equation (6.10)). As expected, we find the two numbers to be the same, regardless of $R_0$ and $C_{\text{loss}}$. Now, that we have proven the validity of the analytic expressions for $v_e$ and $\dot{N}$, we can use them to determine the ion energy and the atom-ion scattering cross section. We start by calculating the peak density of the condensate [60]

$$n = \frac{1}{8\pi}\left(\frac{15 m_{\mathrm{Rb}}^3 \bar{\omega}_{\mathrm{atoms}}^3 N}{\hbar a^{3/2}}\right)^{2/5}. \tag{6.15}$$

For this measurement the mean trap frequency of the atom trap was $\bar{\omega}_{\mathrm{atoms}} = 2\pi \times 31\,\mathrm{Hz}$, leading to a density of $n = 3.8 \times 10^{13}\,\mathrm{cm}^{-3}$. Similar to the thermal case, we then equate (6.14) to (6.6) and get for the depletion

$$n - \tilde{n} = \left(\frac{\sigma_{\mathrm{elastic}} v_I m_{\mathrm{Rb}}}{4\pi R_0^2 \hbar \sqrt{32\pi a}}\right)^2. \tag{6.16}$$

Plugging this expression back into (6.6) we get a differential equation for the atom number of the form

$$\dot{N}(t) = A \cdot N(t)^{2/5} + B. \tag{6.17}$$

The (numerical) solution to this equation is fitted to our data (Fig. 6.3b). For $t = 0$ we find the atom loss rate to be $\dot{N} = 8 \times 10^4\,\mathrm{s}^{-1}$. By equating this value together to the net flux (6.14), we find the lower bound on the ion energy for the BEC measurement to be $E_{\mathrm{I}} \gtrsim k_B \times 1\,\mathrm{mK}$. On the other hand, the upper bound on $E_{\mathrm{I}}$ is again set by how well we can compensate excess micromotion. Since a comparatively large effort was made to compensate micromotion for the experiments with the BEC, we believe that the residual dc electrical fields here are smaller than $2\,\mathrm{V/m}$, corresponding to $E_{\mathrm{I}} \lesssim k_B \times 10\,\mathrm{mK}$. These bounds suggest an ion energy of $E_{\mathrm{I}} \approx 5\,\mathrm{mK}$ and thus a collision energy of $E \approx 2\,\mathrm{mK}$. This implies $R_0 \approx 0.8\,\mu\mathrm{m}$, a density of $\tilde{n} \approx 0.1\,n$ and a cross section of $\sigma_{\mathrm{elastic}} \approx 3.1 \times 10^{-14}\,\mathrm{m}^2$.

In the measurements discussed so far, single $\mathrm{Ba}^+$ ions have been used. However, we have also performed the atom loss experiment with a single $\mathrm{Rb}^+$ ion. For the typical collision energies in our experiment, the inner structure of the atom and the ion, respectively, is not relevant. Nevertheless, a slight difference in the collision rate coefficient $R_{\mathrm{elastic}} = \sigma_{\mathrm{elastic}} v_{\mathrm{I}}$ is expected between $^{138}\mathrm{Ba}^+$ and $^{87}\mathrm{Rb}^+$, since both $\sigma_{\mathrm{elastic}} \propto \mu^{1/3}$ and $v_{\mathrm{I}} \propto \mu^{-1/2}$ depend on the mass of the ion. By assuming the same collision energy $E$ we can use these scalings and find that the collision rate (and thus the inverse lifetime) should only be about 3% larger in the case of a $^{87}\mathrm{Rb}^+$ ion, as compared with the $^{138}\mathrm{Ba}^+$ ion. Unfortunately we were not able to resolve this small difference between $^{87}\mathrm{Rb}^+$ and $^{138}\mathrm{Ba}^+$, due to the large experimental uncertainties in our lifetime measurements on the order

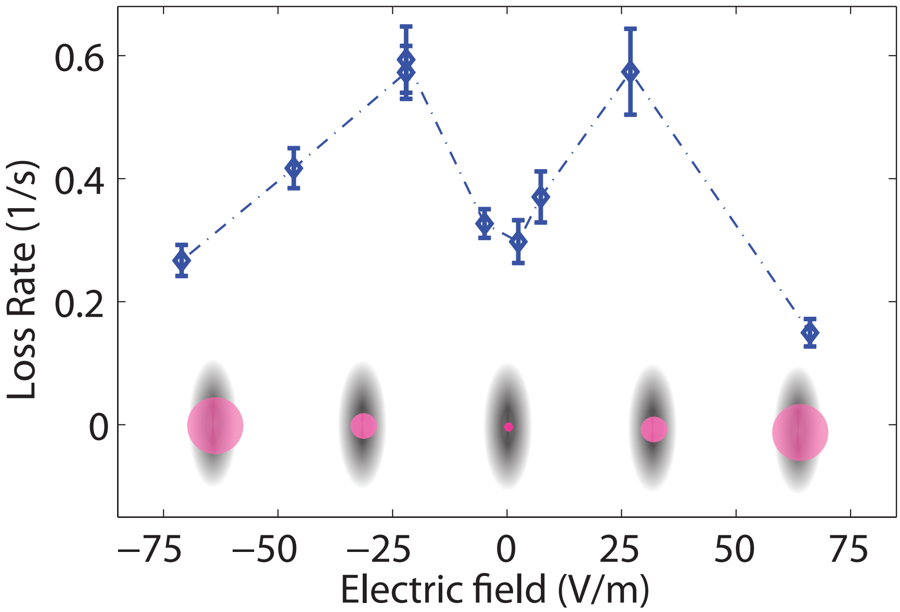

Figure 6.6: Loss rate of a thermal atom cloud when a static electric field is applied. In the presence of a field, the energy of the $Ba^+$ ion and thus the amplitude of its secular motion are increased. As a result the sphere of depletion becomes larger, leading to an enhanced atom loss rate. For fields $|\mathcal{E}_{dc}| > 30\,V/m$, the amplitude of the secular motion is so large, that the ion spends a significant amount of time in a region of lower atom density. Therefore the loss rate decreases at high fields.

of 25% (Fig. 6.3b).

Again, I want to point out that the discussion presented here (i.e. the "sphere of depletion" model) can only be used to get rough estimates for the physical quantities. One issue of our simplified model is clearly the fact that we assume a spherical range of depletion, even though our ion trap is highly anisotropic. Moreover, the depletion will neither be uniform nor will it have a sharp spatial cut-off. For these reasons a more sophisticated description of the atom losses is required, in order to be able to derive more precise values for the ion energy (collision energy) from our measurements.

### 6.1.3 Energy dependence of the collision rate

For the measurements discussed so far, the dc electric field at the position of the ion and thus the ion's excess micromotion was minimized. In the following we intentionally increase the dc electric field $\mathbf{E}_{dc}$ and thus the collision energy $E$. In this case we expect the atom loss rate to rise for two reasons. First, the elastic

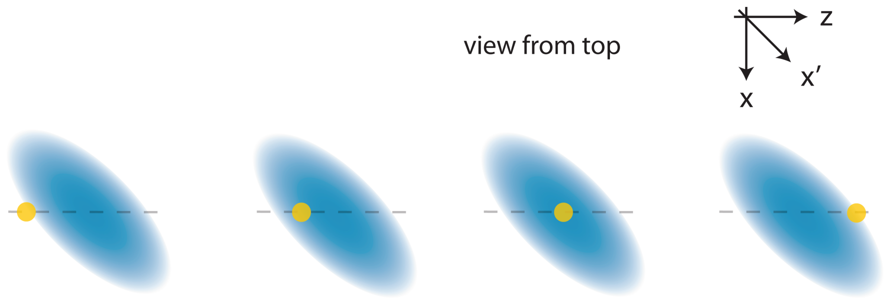

Figure 6.7: An ion as a local density probe: We vary the $z$-position of the ion (orange). At each position we measure the atom loss on a freshly prepared atom cloud (blue).

atom-ion scattering rate rises as $R_{\mathrm{elastic}} = \sigma_{\mathrm{elastic}} v_{\mathrm{I}} \propto E^{1/6} \propto |\mathbf{E}_{\mathrm{dc}}|^{1/3}$, and second, as the sphere of depletion increases, the density inside the sphere $\tilde{n}$ becomes larger (see equation (6.8)). The corresponding measurement is shown in Fig. 6.6. We find an increase of the loss rate up to an electric field of $|\mathbf{E}_{\mathrm{dc}}| \approx 30\,\mathrm{V/m}$, where the amplitude of the ion's secular motion is $R_0 \approx 20\,\mu\mathrm{m}$. This value is comparable to the size of the atom cloud, which has an extension of about 15 µm along the radial and 80 µm along the axial direction. The model of a well-localized ion and a sphere of depletion is clearly no longer valid in this regime. We explain the decrease of the atom loss rate for even higher fields by the fact that the ion spends a significant amount of time in regions of lower atom density.

### 6.1.4 A single ion as a local density probe

To optimize the spatial overlap between the ion and the atoms along all three directions in space, we measure the atom loss as a function of the endcap voltage and the two AOM frequencies. As an example I would like to present a measurement, where we have varied the endcap voltage and thus the $z$-position of a single $\mathrm{Rb}^+$ ion (see Fig. 6.7). At each position the atom loss is measured on a freshly prepared atom cloud for a given interaction time $t_{\mathrm{int}}$. The measurement is performed with a thermal cloud, a semi-condensed cloud and with an almost pure BEC (Fig. 6.8). As expected, the atom loss is always maximal when the ion is placed right into the center of the atom cloud.

We can theoretically reproduce the data shown in Fig. 6.8 with our model, which demonstrates our quantitative understanding of the dynamics. We start again with the general expression for the total atom loss

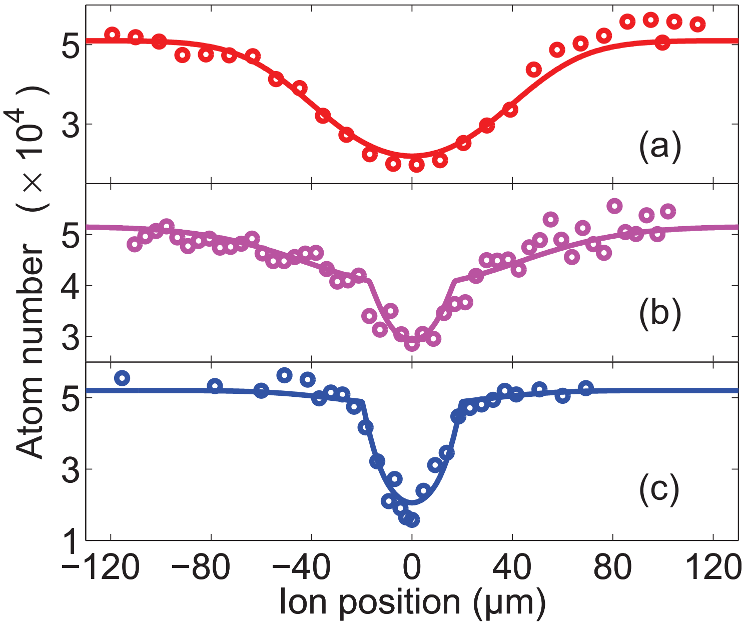

Figure 6.8: Number of Rb atoms remaining in the trap depending on the position of the $\mathrm{Rb}^+$ ion relative to the center of the atom cloud. The measurement is performed with (a) a thermal cloud, (b) a partially condensed cloud and (c) an almost pure Bose-Einstein condensate. The interaction time was (a) 1.5 s, (b) 1 s and (c) 0.5 s. The solid lines are fits, where the ion energy $E_I$ and the atom temperature $T_{\mathrm{Rb}}$ are used as free fit parameters. $E_I$ is kept fixed for all three cases and is found to be 14 mK. The atom temperature on the other hand is varied and turns out to be (a) 50 nK, (b) 35 nK and (c) 25 nK.

$$\dot{N} = -\tilde{n}\sigma_{\text{elastic}}v_{\text{I}}. \tag{6.18}$$

However, the density is now given by

$$\tilde{n} = \tilde{n}_{\text{th}} + \tilde{n}_{\text{c}} \tag{6.19}$$

where

$$\tilde{n}_{\text{th}}(z) = N_{\text{th}}\left(\frac{m_{\text{Rb}}\bar{\omega}_{\text{atoms}}}{l_{\text{dB}}}\right)^3 \exp\left(-\frac{m_{\text{Rb}}\omega_{\text{atoms}}^{(\text{z})\,2}}{2k_{\text{B}}T_{\text{atoms}}}z^2\right)\frac{\pi R_0^2 v_{\text{therm}}}{\pi R_0^2 v_{\text{therm}} + \sigma_{\text{elastic}}v_{\text{I}}} \tag{6.20}$$

is the density of the thermal part of the cloud and

$$\tilde{n}_{\text{c}}(z) = \frac{1}{8\pi}\left(\frac{15m_{\text{Rb}}^3\bar{\omega}_{\text{atoms}}^3}{\hbar a^{3/2}}\right)^{2/5} N_{\text{c}}^{2/5} - \frac{m_{\text{Rb}}^2\omega_{\text{atoms}}^{(\text{z})\,2}}{8\pi\hbar^2 a}z^2 - \left(\frac{\sigma_{\text{elastic}}v_{\text{I}}m_{\text{Rb}}}{4\pi R_0^2\hbar\sqrt{32\pi a}}\right)^2 \tag{6.21}$$

the density of the condensed part. The last factor in equation (6.20) and the last term in equation (6.21) are required to take into account the depletion effect. Moreover we have made use of the well-known density profile for a thermal atom cloud (Gaussian) as well as for a Bose-Einstein condensate (parabolic) confined in a harmonic trap. For the number of thermal atoms $N_{\text{th}}$ and the number of condensed atoms $N_{\text{c}}$ we can write [60]

$$\begin{aligned} N &= N_{\text{th}} + N_{\text{c}} && (6.22)\\ \frac{N_{\text{th}}}{N} &= \left(\frac{T_{\text{atoms}}}{T_{\text{c}}}\right)^3 && (6.23)\\ \frac{N_{\text{c}}}{N} &= 1 - \left(\frac{T_{\text{atoms}}}{T_{\text{c}}}\right)^3. && (6.24) \end{aligned}$$

For a harmonic trap the BEC transition temperature is given by $k_{\text{B}}T_{\text{c}} = \hbar\bar{\omega}_{\text{atoms}}\zeta(3)^{-1/3}$, where $\zeta(3) = 1.202$. Using the expressions (6.20)-(6.24) and setting $\sigma_{\text{elastic}} = 3\times10^{-14}\,\text{m}^2$ (as suggested by the results of the previous section), we numerically solve the differential equation (6.18). We assume that the temperature of the atomic sample $T_{\text{atoms}}$ is constant, due to the very shallow optical trap. $T_{\text{atoms}}$ is used as a free fit parameter in our model together with the ion energy $E_{\text{I}}$, which we keep fixed for all three measurements. The results of our numerical calculations are also depicted in Fig. 6.8. The values for $T_{\mathrm{Rb}}$ obtained from the fit (a) 50 nK, (b) 35 nK and (c) 25 nK are in nice agreement with the temperatures determined separately in time-of-flight measurements. Moreover the fit suggests $E_{\mathrm{I}} \approx k_B \times 14\,\mathrm{mK}$, which is in the same range as the temperatures found in the lifetime experiments.

With this measurement we have shown, that a single ion can be used to locally probe the atomic density distribution. In contrast to the absorption imaging, which integrates over the line of sight, a full 3-dimensional scan of the atom density can be performed with our ion probe. Moreover our new technique features a high spatial resolution on the µm scale.

## 6.2 Inelastic processes

In addition to the elastic processes discussed so far, we have also investigated inelastic atom-ion collisions. Studying inelastic processes is more involved, since the Ba$^+$ ion is either lost from the trap or exchanged by another ion. In both cases, one has to repeatedly load the Paul trap with a new, fresh Ba$^+$ ion, which takes a valuable amount of time on the order of minutes. For this reason the amount of data, that we have obtained so far on inelastic collisions, is limited. Fortunately, all inelastic processes are highly suppressed with respect to the elastic collisions, so that it was possible in the first place to study the elastic processes and the atom-ion collision dynamics in general.

We start the discussion with the most dominant inelastic channel, which turns out to be the charge transfer process

$$\mathrm{Rb} + \mathrm{Ba}^+ \rightarrow \begin{cases} \mathrm{Rb}^+ + \mathrm{Ba} & \text{(non-radiative)} \\ \mathrm{Rb}^+ + \mathrm{Ba} + \nu & \text{(radiative)} \end{cases} \tag{6.25}$$

as expected. The energy released in this reaction is either carried away by a photon (radiative charge transfer) or transferred into kinetic energy of the collision partners. The fact that the charge exchange is exothermic can be read off from the potential curves shown in Fig. 6.9. We start our experiment with a Ba$^+$ ion and neutral Rb atoms, which follow one of the first two excited state potentials (dotted lines in Fig. 6.9), when they come close to each other. Whether they enter the singlet or the triplet channel, respectively, depends on the relative orientation of the electron spin of the Ba$^+$ ion and the Rb atom. Anyway, in both cases

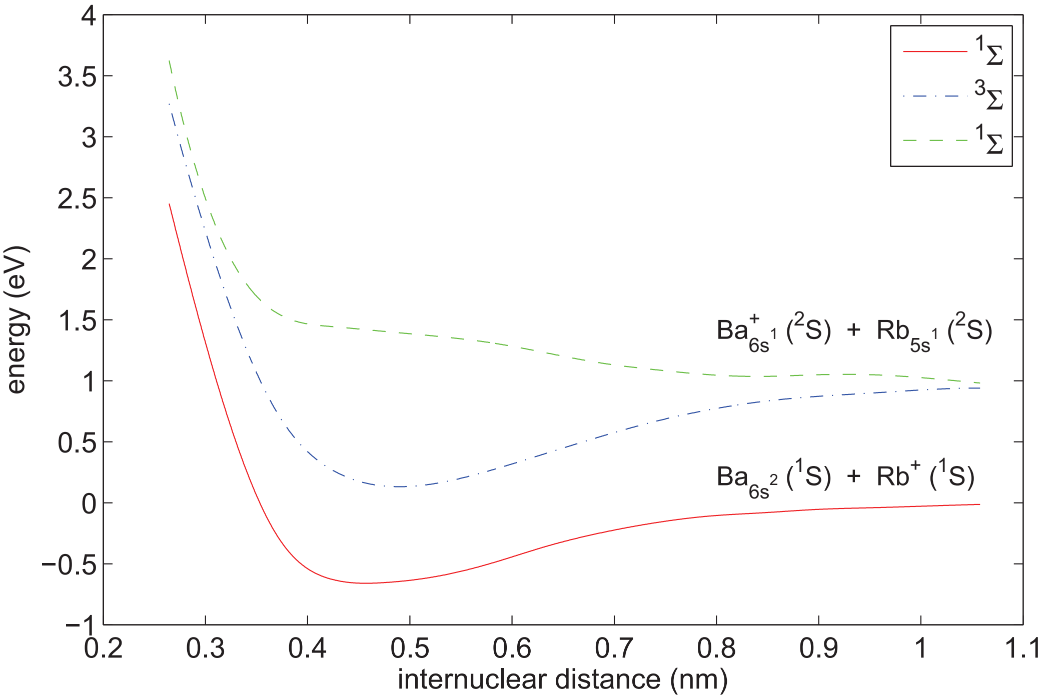

Figure 6.9: The 3 lowest lying potential curves for ($^{138}$Ba - $^{87}$Rb)$^+$: The asymptotic limit (internuclear distance R$\rightarrow \infty$) of the dotted lines corresponds to Ba$^+$ and Rb in their respective groundstates, which are the atomic states with which we start our experiments. Since the ground state potential of our (Ba-Rb)$^+$ system (solid line) asymptotically leads to Rb$^+$ and Ba, the electron is expected to jump from Rb to Ba$^+$. The energy released in such a process is about 1 eV, as can be read off from the asymptotical difference between solid and the dotted potential curves. The data is taken from [61].

the transition into the molecular ground state potential has a small but finite probability. Such a transition corresponds to a charge transfer process, since the molecular ground state potential of the (Ba-Rb)$^+$ system asymptotically (i.e. for a large internuclear distance) leads to neutral Ba and Rb$^+$. More details on the charge transfer collisions (detection, rate, cross section) are given below.

The second type of inelastic collision which are expected to take place in our system are molecule formation processes, such as e.g.

$$\mathrm{Rb} + \mathrm{Ba}^+ \rightarrow \mathrm{RbBa}^+ + \gamma \tag{6.26}$$

$$\mathrm{Rb} + \mathrm{Rb} + \mathrm{Ba}^+ \rightarrow \begin{cases} \mathrm{Rb} + \mathrm{RbBa}^+ \\ \mathrm{Ba} + \mathrm{Rb}_2^+ \end{cases} \tag{6.27}$$

and

$$\mathrm{Rb} + \mathrm{Rb} + \mathrm{Rb}^+ \rightarrow \mathrm{Rb} + \mathrm{Rb}_2^+, \tag{6.28}$$

respectively. These processes are particularly interesting, since they can be used to trap cold molecular ions on a single particle level. In order to be able to observe the 3-body process in our experiment, it will be essential to maximize the atomic density, since the three-body collision rate depends quadratically on the density.

### 6.2.1 Observation of charge transfer reactions

For the detection of the charge transfer process we load two $^{138}\mathrm{Ba}^+$ ions into the ion trap. Typically after a time corresponding to $10^4$-$10^5$ elastic atom-ion collisions, the fluorescence of one of the $\mathrm{Ba}^+$ ions is lost (Fig. 6.10). Since the position of the remaining bright $\mathrm{Ba}^+$ ion does not change, we infer that the other $\mathrm{Ba}^+$ ion has been replaced by an unknown dark ion formed in a reaction. We identify the dark ion by measuring the radial eigenfrequencies of the two-ion crystal. For this purpose we modulate the amplitude of the rf voltage. When the modulation frequency is close to the eigenfrequencies, the motion of the ions is resonantly excited and a drop of the $\mathrm{Ba}^+$ fluorescence signal is observed. This procedure has also been used for the determination of the trap frequencies (of a single ion), as described in chapter 4. In the same chapter I have also derived expressions for the theoretically expected eigenfrequencies of the (hetero-nuclear) two-ion crystal (equations (4.14), (4.15), (4.25) and (4.26)). Using these equations and taking the measured trap frequencies of a single $^{138}\mathrm{Ba}^+$ ion, it is possible to calculate the expected eigenfrequencies of all relevant two-ion systems (table 6.1). In the experiment we observe the radial resonance frequencies to be about 219(1) kHz and 346(1) kHz. By comparison with the table 6.1, we find these values to be in nice agreement with the ones expected for a two-ion crystal consisting of $^{138}\mathrm{Ba}^+$ and a $^{87}\mathrm{Rb}^+$. Therefore we can conclude that the dark ion formed in the reaction has to be $\mathrm{Rb}^+$ and that the dominant inelastic process in our system is indeed the charge transfer process.

As mentioned above, for our experimental settings the charge transfer collision rate is a factor of $10^4$-$10^5$ smaller than the elastic collision rate. This strong suppression of the charge exchange is very important, since it is a necessary prerequisite for all elastic collision experiments. The cross section for charge

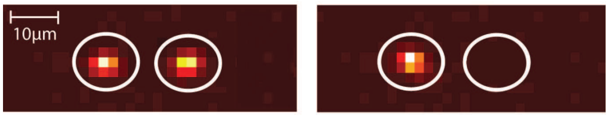

Figure 6.10: *Left*: Fluorescence image of two $\mathrm{Ba}^+$ ions. *Right*: Fluorescence of one $^{138}\mathrm{Ba}^+$ next to an unknown dark ion. We infer the existence of the dark ion from the position of the $\mathrm{Ba}^+$.

exchange can therefore be estimated with

$$\sigma_{\text{ch.ex.}} \approx \frac{\sigma_{\text{elastic}}}{10^4 ... \, 10^5} \approx 10^{-19} ... \, 10^{-18}\,\mathrm{m}^2. \tag{6.29}$$

This value is comparable to the charge transfer cross section for $\mathrm{Rb} + \mathrm{Yb}^+ \rightarrow \mathrm{Rb}^+ + \mathrm{Yb}$ determined by the group of Michael Köhl in Cambridge [9]. For a collision energy on the order of $E \approx 10\,\mathrm{mK}$, the corresponding charge transfer rate is

$$R_{\text{ch.ex.}} = \sigma_{\text{ch.ex.}} \sqrt{\frac{2E}{\mu}} = 10^{-13} ... \, 10^{-12}\,\mathrm{cm}^3\mathrm{s}^{-1}. \tag{6.30}$$

This charge transfer rate is roughly a factor $10^3$ smaller than the one observed in the group of Vladan Vuletic for the energetically resonant case of $^{\alpha}\mathrm{Yb}$ - $^{\beta}\mathrm{Yb}^+$ [7].

From the potential curves (Fig. 6.9) we can read off that the energy released in the charge transfer reaction (6.25) is about $\Delta E_{\text{rel}} \approx 1\,\mathrm{eV}$. This energy can either be transferred into kinetic energy of the collision partners or carried away by a photon. In both cases the $\mathrm{Rb}^+$ ion will stay in the trap, since our Paul trap is very deep with a depth of about 5 eV (see Fig. 4.7). Switching to a lower trap depth of below $m_{\mathrm{Rb}}/(m_{\mathrm{Rb}} + m_{\mathrm{Ba}})\Delta E_{\text{rel}} \approx 0.6\,\mathrm{eV}$ would enable us to discriminate between the radiative charge transfer and non-radiative charge transfer. The theoretical prediction tells us that the process predominately takes place under an emission of a photon [28].

Table 6.1: Trap frequencies and the eigenfrequencies of a two-ion crystal given in kHz.

| | $\omega_{\text{axial}}$ | $\omega_{\text{radial}}$ | $\Omega_+^{\text{axial}}$ | $\Omega_-^{\text{axial}}$ | $\Omega_+^{\text{radial}}$ | $\Omega_-^{\text{radial}}$ |
|---|---|---|---|---|---|---|
| single $^{138}$Ba$^+$ | 40.5 | 220.5 | | | | |
| single $^{87}$Rb$^+$ | 51 | 348 | | | | |
| two $^{138}$Ba$^+$ | | | 70 | 40.5 | 220 | 215.5 |
| $^{138}$Ba$^+$ and $^{87}$Rb$^+$ | | | 81 | 44.5 | 346 | 219 |
| $^{138}$Ba$^+$ and $^{87}$Rb$_2^+$ | | | 66.5 | 38 | 218.5 | 171.5 |
| $^{138}$Ba$^+$ and ($^{87}$Rb$^{138}$Ba)$^+$ | | | 64 | 35 | 218.5 | 132 |

# Chapter 7

# Conclusion and Outlook

In this thesis I have presented an experimental setup, with which collisions between a single trapped $Ba^+$ or $Rb^+$ ion and a cloud of ultracold neutral Rb atoms can be studied. For this purpose we have combined a Bose-Einstein condensation (BEC) apparatus with a linear radiofrequency (rf) Paul trap used for trapping the ions. The ultracold atoms are generated in a Quadrupole-Ioffe-configuration (QUIC) trap and transported over 30 cm into the center of the ion trap. Due to this large distance, mutual disturbance between the rf Paul trap and the production of the ultracold atom cloud is avoided. For the transport we employ a moving 1d optical lattice transport. After the atoms have arrived in the Paul trap, they are loaded into a crossed optical dipole trap and precisely overlapped with the position of the ion.

With our setup both elastic and inelastic collisions between the atoms and the ion can be detected. The cross section for elastic scattering is found to be on the order of $10^{-14}\,\mathrm{m}^2$. This value is more than a factor of $10^4$ larger than the cross section for inelastic scattering. In our system we have identified the dominant inelastic collision channel to be the charge transfer $\mathrm{Rb} + \mathrm{Ba}^+ \rightarrow \mathrm{Rb}^+ + \mathrm{Ba}$. With the help of the elastic collision measurements we were able to investigate the dynamics of the atom-ion scattering. In our case, where we trap the ions using radiofrequency fields, the collision energy is fully determined by the excess micromotion of the ion. We have managed to minimize the collision energy to values on the order of $k_\mathrm{B}\times 10\,\mathrm{mK}$ by properly compensating the electric stray fields at the position of the ion.

After the first experiments discussed in this thesis, a large effort has been made to further improve the compensation of the DC electric stray fields. Thereby, it was possible to further reduce the radial and in particular the axial excess micromotion notably, so that experiments in the sub-mK regime are now possible. In this low energy regime the sympathetic cooling of the ions towards the ground state of the secular potential should be possible. Since the number of partial waves contributing to the scattering gets small for energies below the mK range, quantum mechanical effects should become observable. For example, we should be able to detect magnetic Feshbach resonances in this ultracold regime [19, 29]. These scattering resonances could be used to tune the interaction between the atoms and the ion via an external magnetic field. In addition, they should allow for a controlled formation of an ultracold $(\mathrm{BaRb})^+$ molecular ion, which is an important goal in molecular physics [15, 16]. Alternatively, such ultracold $(\mathrm{BaRb})^+$ ions could also efficiently be produced via photo-association [62].

Besides molecular physics, also polaron-type effects can be studied with our atom-ion system [20–23]. In this context, the ion ($\mathrm{Ba}^+$ or $\mathrm{Rb}^+$) is treated as an impurity in the sea of ultracold atoms. The ionic impurity is expected to lead to a modification of the atomic density distribution [20, 63]. A related mechanism is the formation of mesoscopic molecular ions [5]. For this purpose ionic impurities need to be put into a BEC. A large number of atoms can then be captured into loosely bound states via "super-elastic scattering". In this type of collisions a BEC atom is captured by the ion and the kinetic energy is released via the emission of a phonon, i.e. it is shared among the remaining atoms and the freshly formed mesoscopic ion.

Our setup also allows to study the charge mobility in an ultracold atom cloud [4]. In particular with our homo-nuclear configuration (Rb-$\mathrm{Rb}^+$), we could search for the predicted transition between the high temperature regime, where the charges are transported by the ions themselves, and the low temperature regime, where the electrons hop from the neighboring atom to the positive ion (hopping conductivity). In the long term it might be interesting to implement an optical lattice potential for the neutral atoms. Thereby controlled collisions between a single atom and a single ion could be studied [64].

Since the ion energy was successfully reduced to the sub-mK range, the experimental realization of many of the proposals given above, is now within reach. For experiments that require ion energies below what can be reached in rf Paul traps, the ion could be loaded into an optical dipole trap. However, the trapping of ions using laser fields is not yet fully developed. First experiments in this direction have been performed recently [65, 66].

# Chapter 8

# Danksagung

Ich möchte mich bei allen Personen bedanken, die mir geholfen haben diese Dissertation anzufertigen. Allen voran gilt da natürlich der Dank Johannes Hecker Denschlag, der mir den Aufbau dieses Projekt anvertraut hat. Als Betreuer meiner Diplomarbeit und jetzt als Doktorvater hat er meine wissenschaftliche Entwicklung maßgeblich geprägt. Ihm möchte ich vor allem für sein Interesse an meinen Arbeiten und für die zugehörigen Ratschläge danken.

Des weiteren gilt ein großer Dank Arne Härter, meinem langjährigen Forschungsbruder am BaRbiE Projekt, mit dem ich den Großteil meiner Messungen durchgeführt habe. Nur durch seinen unermüdlichen Einsatz (möglich gemacht durch den roten Bullen), seine Hilfe und sein Können war es möglich, noch vor dem Umzug des Experiments von Innsbruck nach Ulm, erste Forschungsergebnisse am BaRbi Experiment einzufahren und in der Folge diese Dissertation anzufertigen. Ein großes Dankeschön gilt natürlich auch Albert Frisch und Sascha Hoinka, die vor allem mit ihren besonderen technischen Fähigkeiten maßgeblich zum Erfolg dieses Exeriments beigetragen haben.

Rudi Grimm will ich dafür danken, dass wir Teil seiner herausragenden Forschungsgruppe sein durften und speziell auch dafür, dass er uns in der schwierigen Zeit vor dem Ulmzug sehr entgegengekommen ist, was das Nutzen seiner Räumlichkeiten beziehungsweise der Infrastrukur allgemein betrifft.

Bedanken will ich mich bei allen Mitstreitern der Arbeitsgruppen von Johannes Hecker Denschlag, Rudi Grimm und Rainer Blatt für ihre physikalische beziehungsweise mentale Unterstützung. Ganz besonders will ich mich auch bei den Leuten aus der Mechanikwerkstätte und dem Sekretariat bedanken, ohne die der Aufbau des Projekts in dieser Form nicht möglich gewesen wäre.

Auch will ich all meinen Freunden und Kollegen danken, die mich während meiner Zeit als Doktorand unterstützt haben, allen voran meiner Freundin Petra. Bei ihr konnte ich die notwendige Kraft tanken, um die langen Labortage und -nächte (insbesondere die vor dem Ulmzug) durchzustehen. Zuletzt will ich meiner Mutter danken, die mir diese Ausbildung ermöglicht und mich jederzeit voll unterstützt hat.

# Chapter 9

# Erklärung

Hiermit erkläre ich, dass ich die vorliegende Arbeit selbständig verfasst, keine anderen Quellen und Hilfsmittel als die angegebenen benutzt und die Stellen der Arbeit, die anderen Werken dem Wortlaut oder dem Sinn nach entnommen sind, in jedem Fall unter Angabe der Quelle als Entlehnung kenntlich gemacht habe. Das Gleiche gilt für beigegebenen Zeichnungen und Darstellungen.

Ulm, am

---

Stefan Schmid

# Bibliography

[1] D. Leibfried, R. Blatt, C. Monroe, and D. J. Wineland, "Quantum dynamics of single trapped ions," *Rev. Mod. Phys.*, vol. 75, p. 281, 2003.

[2] "Nature insight on ultracold matter," *Nature*, vol. 416, pp. 205–246, 2002.

[3] R. Côté and A. Dalgarno, "Ultracold atom-ion collisions," *Phys. Rev. A*, vol. 62, p. 012709, 2000.

[4] R. Côté, "From classical mobility to hopping conductivity: Charge hopping in an ultracold gas," *Phys. Rev. Lett.*, vol. 85, p. 5316, 2000.

[5] R. Côté, V. Kharchenko, and M. D. Lukin, "Mesoscopic molecular ions in Bose-Einstein condensates," *Phys. Rev. Lett.*, vol. 89, p. 093001, 2002.

[6] M. Cetina, A. Grier, J. Campbell, I. Chuang, and V. Vuletić, "Bright source of cold ions for surface-electrode traps," *Phys. Rev. A*, vol. 76, p. 041401, 2007.

[7] A. T. Grier, M. Cetina, F. Oručević, and V. Vuletić, "Observation of cold collisions between trapped ions and trapped atoms," *Phys. Rev. Lett.*, vol. 102, p. 223201, 2009.

[8] C. Zipkes, S. Palzer, C. Sias, and M. Köhl, "A trapped single ion inside a Bose-Einstein condensate," *Nature*, vol. 464, p. 388, 2010.

[9] C. Zipkes, S. Palzer, L. Ratschbacher, C. Sias, and M. Köhl, "Cold heteronucler atom-ion collisions," *Phys. Rev. Lett.*, vol. 105, p. 12559, 2010.

[10] C. Zipkes, L. Ratschbacher, C. Sias, and M. Köhl, "Kinetics of a single trapped ion in an ultracold buffer gas," *New. J. Phys.*, vol. 13, p. 053020, 2011.

[11] M. Hawley and M. A. Smith *J. Chem. Phys.*, vol. 95, p. 8662, 1991.

[12] D. Gerlich, E. Herbst, and E. Roue *Planetary and Space Science*, vol. 50, p. 1275, 2002.

[13] D. Gerlich *Phys. Chem. Chem. Phys.*, vol. 7, p. 1583, 2005.

[14] S. Willitsch, M. T. Bell, A. D. Gingell, S. R. Procter, and T. P. Softley, "Cold reactive collisions between laser-cooled ions and velocity-selected neutral molecules," *Phys. Rev. Lett.*, vol. 100, p. 043203, 2008.

[15] P. F. Staanum, K. Hojbjerre, P. Skyt, A. Hansen, and M. Drewsen, "Rotational laser cooling of vibrationally and translationally cold molecular ions," *Nat. Phys.*, vol. 6, p. 271, 2010.

[16] T. Schneider, B. Roth, H. Duncker, I. Ernsting, and S. Schiller, "All-optical preparation of molecular ions in the rovibrational ground state," *Nat. Phys.*, vol. 6, p. 275, 2010.

[17] S. Schmid, A. Härter, A. Frisch, S. Hoinka, and J. H. Denschlag, "An apparatus for immersing cold trapped ions into a quantum degenerate gas of neutral atoms," *to be published*.

[18] S. Schmid, A. Härter, and J. H. Denschlag, "Dynamics of a cold trapped ion in a Bose-Einstein condensate," *Phys. Rev. Lett.*, vol. 105, p. 133202, 2010.

[19] Z. Idziaszek, T. Calarco, P. S. Julienne, and A. Simoni, "Quantum theory of ultracold atom-ion collisions," *Phys. Rev. A*, vol. 79, p. 010702, 2009.

[20] P. Massignan, C. J. Pethik, and H. Smith, "Static properties of positive ions in atomic Bose-Einstein condensates," *Phys. Rev. A*, vol. 71, p. 023606, 2005.

[21] R. M. Kalas and D. Blume, "Interaction-induced localization of an impurity in a trapped Bose-Einstein condensate," *Phys. Rev. A*, vol. 73, p. 043608, 2006.

[22] F. M. Cuccietti and E. Timmermans, "Strong-coupling polarons in dilute gas Bose-Einstein condensates," *Phys. Rev. Lett.*, vol. 96, p. 210401, 2006.

[23] G. E. Astrakharchik and L. P. Pitaevskii, "Motion of a heavy impurity through a Bose-Einstein condensate," *Phys. Rev. A*, vol. 70, p. 013608, 2004.

[24] R. Teachout and R. Pack, "Table of experimental and calculated static dipole polarizabilities for the electronic ground states of the neutral elements (in atomic units)," *Atomic Data*, vol. 3, p. 195, 1972.

[25] C. Chin, R. Grimm, P. S. Julienne, and E. Tiesinger, "Feshbach resonances in ultracold gases," *Phys. Mod. Phys.*, vol. 82, p. 1225, 2010.

[26] P. Langevin, "Une formule fondamentale de théorie cinétique," 1905.

[27] C. Cohen-Tannoudji, B. Diu, and F. Laloë, *Quantum mechanics - Vol. 2.* 1999.

[28] O. P. Makarov, R. Côté, and W. W. Smith, "Radiative charge-transfer lifetime of the excited state of $(\mathrm{NaCa})^+$," *Phys. Rev. A*, vol. 67, p. 042705, 2003.

[29] Z. Idziaszek, *private communication.*

[30] C. Zipkes, L. R. S. Palzer, C. Sias, and M. Köhl, "Hybrid quantum systems of atoms and ions," *J. Phys.: Conf. Ser.*, vol. 264, p. 012019, 2011.

[31] D. Naik and C. Raman, "Optically plugged quadrupole trap for Bose-Einstein condensates," *Phys. Rev. A*, vol. 71, p. 033617, 2005.

[32] D. Steck, "Rb d-line data," 2002.

[33] D. J. McCarron, S. A. King, and S. L. Cornish, "Modulation transfer spectroscopy in atomic rubidium," *Meas. Sci. Technol.*, vol. 19, p. 105601, 2008.

[34] G. C. Bjorklund, M. D. Levenson, W. Lenth, and C. Ortiz, "Frequency modulation (fm) spectroscopy," *Meas. Sci. Technol.*, vol. 32, pp. 145–152, 1983.

[35] Webpage of Florian Schreck, *http://iqoqi006.uibk.ac.at/users/c704250/.*

[36] D. J. Wineland, C. Monroe, W. M. Itano, B. E. K. D. Leibfried, and D. M. Meekhof, "Experimental Issues in Coherent Quantum-State Manipulation of Trapped Atomic Ions," *J. R. Nat. Inst. St. Techn.*, vol. 103, p. 259, 1998.

[37] P. K. Gosh, *Ion traps.* Clarendon Press, 1995.

[38] M. Drewsen and A. Brøner., "Harmonic linear Paul trap: Stability diagram and effective potentials," *Phys. Rev. A*, vol. 62, p. 045401, 2000.

[39] D. J. Berkeland, J. D. Miller, J. C. Bergquist, W. M. Itano, and D. J. Wineland, “Minimization of ion micromotion in a Paul trap,” *J. Appl. Phys.*, vol. 83, p. 10, 1998.

[40] L. D. Landau and E. M. Lifshitz, *Mechanics.* New York: Pergamon.

[41] D. Rotter, *Quantum feedback and quantum correlation measurements with a single Barium ion.* PhD thesis, Universität Innsbruck, 2008.

[42] T. W. Hänsch and A. L. Schawlow, “Cooling of gases by laser radiation,” *Opt. Comm.*, vol. 13, p. 68, 1975.

[43] T. Fließbach, *Mechanik.* Springer.

[44] G. Morigi and H. Walther, “Two-species Coulomb chains for quantum information,” *Eur. Phys. J. D*, vol. 13, pp. 261–269, 2000.

[45] M. Theis, *Optical Feshbach Resonances in a Bose-Einstein Condensate.* PhD thesis, Universität Innsbruck, 2005.

[46] E. L. Raab, M. Prentiss, A. Cable, and S. Chu, “Trapping of neutral sodium atoms with radiation pressure,” *Phys. Rev. Lett.*, vol. 59, pp. 2631–2634, 1987.

[47] W. D. Philips, “Laser cooling and trapping of neutral atoms,” *Rev. Mod. Phys.*, vol. 70, p. 721, 1998.

[48] H. J. Metcalf and P. van der Straten, *Laser cooling and trapping.* New York, Berlin, Heidelberg: Springer-Verlag, 1999.

[49] M. Greiner, I. Bloch, T. W. Hänsch, and T. Esslinger, “Magnetic transport of trapped cold atoms over a large distance,” *Phys. Rev. A*, vol. 63, p. 031401, 2001.

[50] R. Grimm, M. Weidemller, and Y. Ovchinnikov, “Optical dipole traps for neutral atoms,” *Adv. At. Mol. Opt. Phys.*, vol. 42, p. 95, 2000.

[51] T. L. Gustavson, A. P. Chikkatur, A. E. Leanhardt, A. Gorlitz, S. Gupta, D. E. Pritchard, and W. Ketterle, “Transport of Bose-Einstein condensates with optical tweezers,” *Phys. Rev. Lett.*, vol. 88, p. 020401, 2001.

[52] S. Kuhr, W. Alt, D. Schrader, M. Müller, V. Gomer, and D. Meschede, “Deterministic delivery of a single atom,” *Science*, vol. 293, p. 278, 2001.

[53] S. Schmid, G. Thalhammer, K. Winkler, F. Lang, and J. H. Denschlag, "Long distance transport of ultracold atoms using a 1d optical lattice," *New. J. Phys.*, vol. 8, p. 159, 2006.

[54] S. Schmid, "Long distance optical transport of ultracold atoms using a 1d optical lattice," Master's thesis, Universität Innsbruck, 2006.

[55] J. H. Denschlag, J. E. Simsarian, H. Häffner, C. McKenzie, A. Browaeys, D. Cho, K. Helmerson, S. L. Rolston, and W. D. Phillips, "A Bose-Einstein condensate in an optical lattice," *J. Phys. B*, vol. 35, pp. 3095–3110, 2002.

[56] G. Thalhammer, *Ultrakalte gepaarte Atome in kohrenten Lichtfeldern.* PhD thesis, Universität Innsbruck, 2007.

[57] D. Hucul, M. Yeo, S. Olmschenk, C. Monroe, W. Hensinger, and J. Rabchuk, "On the transport of atomic ions in linear and multidimensional ion trap arrays," *arxiv:quant-ph*, p. 0702175v3, 2008.

[58] F. G. Major and H. G. Dehmelt, "Exchange-collision technique for the rf spectroscopy of stored ions," *Phys. Rev.*, vol. 170, p. 91, 1968.

[59] R. DeVoe, "Power-law distributions for a trapped ion interacting with a classical buffer gas," *Phys. Rev. Lett.*, vol. 102, p. 063001, 2009.

[60] C. Pethik and H. Smith, *Bose-Einstein condensation in dilute gases.* Cambridge Univeristy Press, 2001.

[61] S. Knecht, H. J. Jensen, and T. Fleig, "Large-scale parallel configuration interaction. i. nonrelativistic and scalar-relativistic general active space implementation with application to (rbba)$^+$," *J. Chem. Phys.*, vol. 128, p. 014108, 2008.

[62] A. Rakshit and B. Deb, "Formation of cold molecular ions by radiative processes in cold ion-atom collisions," *Phys. Rev. A*, vol. 83, p. 022703, 2011.

[63] J. Goold, H. Doerk, Z. Idziaszek, T. Calarco, and T. Busch, "Ion-induced density bubble in a strongly correlated one-dimensional gas," *Phys. Rev. A*, vol. 81, p. 041601, 2010.

[64] Z. Idziaszek, T. Calarco, and P. Zoller, "Controlled collisions of a single atom and an ion guided by movable trapping potentials," *Phys. Rev. A*, vol. 76, p. 033409, 2007.

[65] C. Schneider, M. Enderlein, T. Huber, and T. Schätz

[66] C. Cormick, T. Schätz, and G. Morigi, “Trapping ions with lasers,” *New. J. Phys.*, vol. 13, p. 043019, 2011.